A Monolithic Finite Element Approach for Interface Capturing in Multiphase Flow Problems

---

Dissertation

zur Erlangung des akademischen Grades eines

Doktors der Naturwissenschaften

(Dr. rer. nat.)

Der Fakultät für Mathematik der

Technischen Universität Dortmund

vorgelegt von

Muhammad Aaqib Afaq

im April 2026

Dissertation

A Monolithic Finite Element Approach for Interface Capturing in Multiphase Flow Problems

Fakultät für Mathematik
Technische Universität Dortmund

Mitglieder der Prüfungskommission:

Erstgutachter:	Prof. Dr. Stefan Turek
Zweitgutachter:	Privatdozent Dr. Andriy Sokolov

Tag der mündlichen Prüfung: 16.07.2026

Abstract

Multiphase flows are fundamental to diverse industrial applications, from inkjet technology and droplet formation to bubble dynamics in chemical reactors. Despite their prevalence, the numerical simulation of interfacial dynamics remains a significant challenge due to the stiff non-linearities introduced by surface tension and the geometric complexities of moving boundaries. Traditional numerical frameworks often struggle with restrictive capillary time step constraints, the need for frequent interface reinitialization, and the inaccuracies associated with explicit curvature estimation.

This thesis presents a robust, monolithic finite element solver designed for the simultaneous calculation of velocity, pressure, and interface position in incompressible multiphase flows. Building upon curvature free level set and indicator-based material function formulations, the proposed method eliminates the need for explicit calculation of interface normals and curvature. This approach bypasses the traditional capillary time step restriction and removes the necessity for separate redistancing or reinitialization procedures, which are integrated directly into the non-linear formulation.

The governing equations are discretized using the high-order stable FEM pair $Q_2P_1^{disc}$ for velocity and pressure, while a Q_2 approximation is employed for the interface scalar fields. The resulting non-linear system is resolved using a discrete Newton solver with a divided difference evaluation of the Jacobian matrices. To handle the resulting saddle-point problems, a suitable linear solver is implemented within the FeatFlow software framework.

The accuracy, stability, and mass conservation properties of the solver are rigorously validated against established test cases and benchmark, including the static bubble, the oscillating bubble, and the rising bubble cases. The results demonstrate that the monolithic coupling provides an efficient and robust framework capable of handling high surface tension coefficients without compromising interface integrity, offering a significant ad-

vancement over decoupled or explicit interfacial solvers.

Keywords: Multiphase flows, Interfacial flows, Level set method, Material cut-off function, Redistancing, Reinitialization, Finite element method, Newton method.

Dedication

To my
grandparents (late), parents,
wife, siblings,
and lovely son

Acknowledgements

First and foremost, I would like to express my deepest gratitude to my supervisor, Prof. Dr. Stefan Turek, for providing me the opportunity to conduct research within his prestigious group. His invaluable expertise and insightful feedback challenged me to sharpen my scientific thinking and elevated my work to a higher standard. I am profoundly grateful for his guidance, confidence, and constant optimism throughout these years. His scientific vision has been indispensable to this thesis and will remain a source of inspiration for my future career. Furthermore, I am deeply impressed by his ability to manage the Faculty of Mathematics as Dean while maintaining a leading research group; his leadership, both in science and administration, is truly exemplary. On a personal note, I must also acknowledge him as my toughest opponent on the table tennis table.

I am sincerely thankful to PD Dr. Andriy Sokolov for our many fruitful discussions regarding the mathematical foundations of my research. I am also honored and grateful that he accepted the role of second reviewer for this thesis.

Special thanks go to Dr. Abderrahim Ouazzi for his guidance and the helpful technical discussions that significantly deepened my understanding of the research topic. I am also indebted to Dr. Hogenrich Damanik for providing his version of the FeatFlow software and for his assistance in navigating the codebase.

I would like to thank my office mates, Dr. Omid Ahmadi, Dr. Babak Hosseini, and Alexander Westermann, for fostering such a supportive and friendly working environment. My gratitude also extends to my colleagues Dr. Liudmila Rivkind and Dr. Hennes Hajduk, as well as the entire LSIII staff and secretaries, for their wonderful collaboration over the years. Furthermore, I appreciate the invaluable reviews and suggestions provided by Dr. Christoph Lohmann, Michael Fast, Dr. Mirco Arndt, Dr. Hogenrich Damanik, and Dr. Arooj Fatima for bringing the thesis in this final stage.

I am extremely grateful to my wife, Dr. Arooj Fatima, for her immense love, patience,

and support. As a fellow researcher at LSIII, our long discussions on our respective fields have significantly broadened my scientific vision. This endeavor would not have been possible without her constant encouragement through the challenges of these past years.

Finally, I wish to thank my parents, Afaq and Rehana, and my siblings for their prayers, love, and moral support. This journey would be incomplete without mentioning my son, Shayaan Aaqib Afaq. He has been a profound blessing in my life; as a child, he taught me-not through words, but through his own perseverance-to "try and try again" until succeeding.

Lastly, I gratefully acknowledge the financial support provided by the Erasmus Mundus INTACT project, the Faculty of Mathematics at TU Dortmund University, and the SimulAC project (No. 01IF23298N), funded by the Federal Ministry for Economic Affairs and Climate Action. I also acknowledge the technical support provided by the LiDO3 team at ITMC, TU Dortmund University.

Muhammad Aaqib Afaq

Nomenclature

Symbol	Description
Domains and Variables	
Ω	Fluid domain
ρ	Fluid density
$\mathbf{u}$	Velocity vector field
μ	Dynamic viscosity
$\mathbf{D}(\mathbf{u})$	Deformation tensor: $\frac{1}{2}(\nabla\mathbf{u}+\nabla\mathbf{u}^{\mathrm{T}})$
p	Pressure field
$\mathbf{f}$	External forces
t	Time
Γ	Interface
κ	Curvature
σ	Surface tension coefficient
$\mathbf{n}$	Unit normal vector
δ_Γ	Dirac delta function concentrated on the interface
ϵ	Interface thickness parameter
Π	Polynomial function
$\mathrm{dist}_\Gamma(\mathbf{x})$	Signed distance function to the interface
$\phi(\mathbf{x},t)$	Level set function
$\psi(\mathbf{x},t)$	Material cut-off function
exp	Exponential function
$H(\psi)$	Hessian operator
P_s	Projection matrix onto the tangent plane: $I-\mathbf{n}\otimes\mathbf{n}$
I	Identity matrix
∇_s	Tangential gradient operator

Symbol	Description
$\boldsymbol{\tau}_s$	Cauchy stress tensor
$\boldsymbol{\tau}_m$	Stress-modified tensor
τ	Fictitious reinitialization time
γ	Reinitialization rate
$\mathbf{v}$	Velocity test function
q	Pressure test function
Re	Reynolds number
Eo	Eötvös number
g	Gravitational acceleration
$\mathcal{U}_b$	Bubble rise velocity
X_c	Bubble center of mass
ϕ	Bubble circularity
Δt_h^{cap}	Capillary time step
γ_1	Compression parameter
γ_2	Diffusion parameter
Function Spaces and Discretization	
$C^0(\Omega)$	Space of continuous functions
$L^2(\Omega)$	Space of square-integrable functions
$L_0^2(\Omega)$	Space of L^2 functions with zero mean value
$\boldsymbol{H}^1(\Omega)$	Sobolev space of functions with square-integrable first derivatives
$\boldsymbol{H}_0^1(\Omega)$	Vector-valued Sobolev space with zero trace on the boundary
$[\boldsymbol{H}_0^1(\Omega)]^d$	Vector-valued Sobolev space with dimension d
$\mathbb{R}$	Set of real numbers
$\mathbb{V}$	Continuous velocity space
$\mathbb{V}'$	Dual space of $\mathbb{V}$
$\mathbb{M}$	Continuous material cut-off function space
$\mathbb{M}'$	Dual space of $\mathbb{M}$
$\mathbb{Q}$	Continuous pressure space
$\mathbb{Q}'$	Dual space of $\mathbb{Q}$
$(\cdot,\cdot)$	L^2 inner product
$\langle\cdot,\cdot\rangle$	Duality pairing
$\mathcal{T}_h$	Finite element mesh / triangulation
h	Element size
$\mathbb{V}^h$	Discrete velocity finite element space
$\mathbb{Q}^h$	Discrete pressure finite element space

Symbol	Description
$\mathbb{M}^h$	Discrete material cut-off finite element space
$\mathbf{u}_h, \mathbf{v}_h$	Discrete trial and test velocity functions
p_h, q_h	Discrete trial and test pressure functions
ψ_h, ξ_h	Discrete trial and test material cut-off functions
v_i, χ_i	Finite element basis functions
Error Analysis and Norms	
$\|e\|_0$	L^2-norm of the error
$\|e\|_1$	H^1-norm of the error
$\|e\|_\infty$	L^∞-norm (maximum) of the error
EOC	Estimated Order of Convergence
$\|\cdot\|_0$	L^2-norm
$\|\cdot\|_{1,h}$	Mesh-dependent H^1 norm

Contents

1

Introduction

1.1 Introduction, Background and Motivation

Fluid motion plays a fundamental role in our daily lives, manifesting in various essential processes such as blood circulation through our veins, the inhalation and exhalation of air in the respiratory system, and the consumption of liquids like water. Beyond everyday occurrences, fluid dynamics is integral to a broad spectrum of scientific challenges and real-world applications. For instance, in aerodynamics, it influences the design of aircraft, automobiles, and wind turbines. In the chemical industry, it governs multiphase flows in transport processes, gas-liquid reactors, and boiling phenomena. Similarly, in the biomedical field, it is crucial for simulating cardiovascular hemodynamics.

Most of these aforementioned phenomenons may involve two or more immiscible fluids. The immiscibility property prevents these fluids from mixing, maintaining distinct phases separated by interfaces. Such systems fall under the category of multiphase fluids.

Multiphase flows are of significant interest across various industrial and engineering applications due to their complex dynamics and critical role in system performance. For instance, in naval engineering, boat design must account for wave interactions and their impact on stability and propulsion. In printing technology, inkjet printers rely on precise control of droplet formation to ensure high quality printing. Similarly, in thermal and chemical process industries, heat exchangers and chemical reactors often involve bubble dynamics, which influence heat and mass transfer efficiency.

The simplest form of multiphase flow is two-phase flow [1], where two distinct fluid

phases coexist while being separated by an interface. At this interface, surface tension forces play a crucial role in governing fluid behavior. When the interacting fluids have different densities and viscosities, a discontinuous pressure jump occurs across the interface due to the imbalance in normal stresses. Furthermore, as flow evolves, the interface itself can undergo movement or deformation, leading to complex interfacial dynamics that must be accurately modeled and analyzed.

The behavior of fluid flow can be analyzed using two primary approaches. The first approach involves experimental techniques, which are often considered ideal as they provide direct physical measurements of the phenomena under investigation. However, experimental studies come with several limitations, including high costs, time-consuming procedures, and potential safety hazards, particularly when dealing with hazardous or reactive chemical fluids.

An alternative and widely adopted approach is the development of mathematical models to describe these fluid dynamics phenomena. Which serves as an effective substitute for experimental studies by overcoming many of their limitations. However, the governing equations in these models are often highly complex, making analytical solutions either extremely difficult or, in some cases, impossible to obtain. To address this challenge, numerical methods are employed as a practical means of approximating solutions to these complex systems of equations. Numerical simulations have become an essential tool in modern fluid dynamics research, enabling accurate and efficient analysis of multiphase flows and other intricate fluid behaviors.

In the context of multiphase flow problems, interface modeling can be broadly classified into two main approaches: interface tracking and interface capturing [2].

Interface tracking methods explicitly define the interface, often using techniques such as fitted-mesh approaches. Examples of this category include the immersed boundary method [3, 4] and the front tracking method [5, 6]. A key advantage of interface tracking is its ability to ensure mass conservation with high accuracy. However, a major drawback is the necessity for remeshing at every time step to accurately follow the evolving interface, which significantly increases computational complexity.

In contrast, interface capturing methods represent the interface implicitly, typically by defining it using a level set function or a color function with a constant value. These methods are particularly advantageous from a computational and implementation perspective, as they employ fixed grids, eliminating the need for remeshing. However, additional procedures such as reinitialization or redistancing might be required to maintain mass conservation accurately. Most widely used Eulerian interface capturing methods (Fig. 1.1) are listed below:

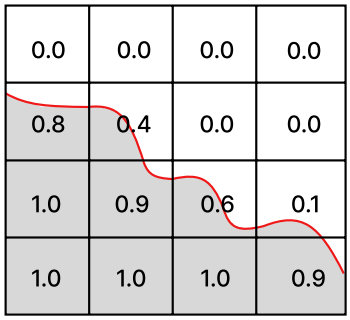

(a) Volume of fluid

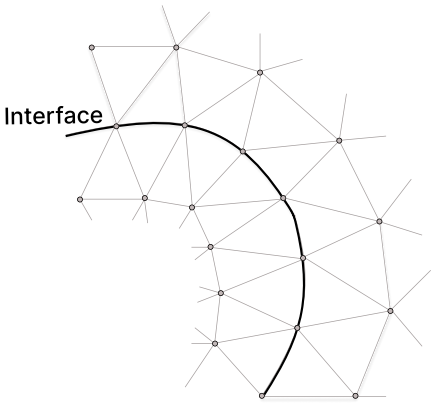

(b) Augmented Lagrangian Eulerian

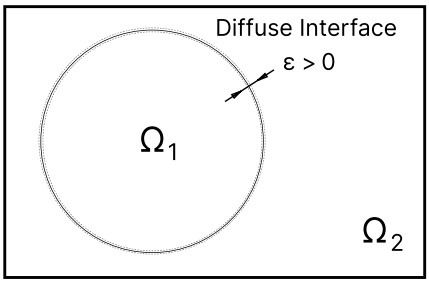

(c) Phase field

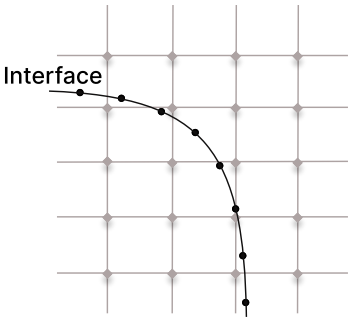

(d) Immersed Boundary

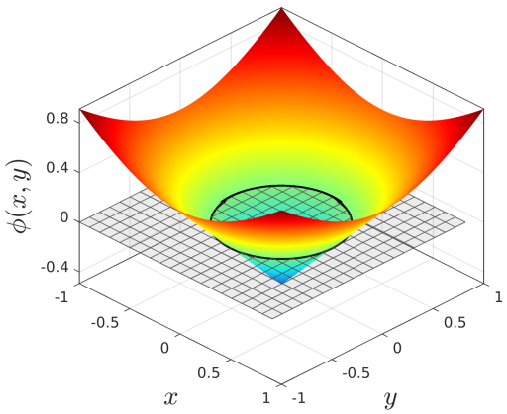

(e) Level set

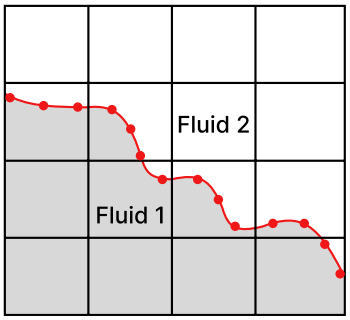

(f) Front tracking

Figure 1.1: Interface capturing and tracking methods.

- Volume of fluid (VOF) method [7, 8, 9] tracks the fraction of fluid in each computational cell.
- Phase field method [10, 11, 12, 13] introduces an order parameter to distinguish different phases and incorporates interfacial physics.
- Level set method [14, 15, 16, 17, 18] represents the interface as a zero level set of a signed distance function.

Each of these methods has its own advantages and limitations, making the choice of approach highly dependent on the specific requirements of a given multiphase flow problem.

1.2 Contribution of the Thesis

The contributions of this thesis is to address the key challenges of solving the incompressible multiphase flow problems numerically using the classical methods (e.g. continuum surface force (CSF)) and to overcome its limitations by adapting the alternative approach (continuum surface stress (CSS)) with its extended version that circumvents the need of redistancing and curvature calculation issues.

First, a numerical solver is developed to efficiently solve the governing system of equations using a monolithic (fully coupled) approach. This formulation ensures a more stable and accurate solution compared to traditional segregated methods, particularly in the presence of complex interfacial dynamics. Leveraging the CSS approach [19], a novel stress tensor formulation is introduced, wherein the surface force term is expressed as the divergence of the stress tensor [20]. This formulation offers several significant advantages, unlike the CSF approach [21], which requires explicit computations of curvature, normal vectors, and delta functions to approximate surface tension forces, the CSS-based formulation naturally incorporates these effects, eliminating the need for such calculations.

Furthermore, in the proposed fully implicit method (2.6.3), the explicit redistancing procedure is entirely removed by integrating the non-linear term directly into the formulation [22]. This modification enhances numerical stability and efficiency, making the approach particularly well-suited for simulations involving strong interfacial deformations. Additionally, this method serves as a promising candidate for alleviating the capillary time step restriction, a well-known constraint in the numerical treatment of interfacial flow problems dominated by surface tension effects. By mitigating this limitation, the proposed approach enables more efficient and robust simulations of multiphase flows over extended time scales.

1.3 Organization

The structure of this dissertation, in addition to the present introductory chapter, is arranged as follows:

Chapter 2 is devoted to the mathematical formulation and numerical treatment of interfacial force modeling within the level set framework. Particular emphasis is placed on the incorporation of surface tension forces into the governing equations of incompressible multiphase flow. In this context, a formal connection between the continuum surface force (CSF) and the continuum surface stress (CSS) formulations is established. The computational implications of this approach, especially in terms of accuracy and numerical stability are discussed in detail.

Chapter 3 addresses the selection and analysis of finite element spaces suitable for a stable discretization of the Stokes system. This includes a thorough discussion of the finite element approximation of the Stokes equations and the inherent challenges associated with their discretization. Particular attention is paid to difficulties arising from the saddle-point structure of the Stokes problem and the requirement for finite element pairs that satisfy the inf-sup (Ladyzhenskaya-Babuška-Brezzi) condition for velocity-pressure coupling.

Chapter 4 presents the numerical strategies employed for solving the curvature free material cut-off function formulation. The justification behind their selection, as well as their integration into the computational framework, is discussed. This chapter further introduces both non-linear and linear solvers used in the present work. The performance and robustness of the monolithic Navier-Stokes solver are validated through the classical "flow around a cylinder" benchmark problem.

Chapter 5 contains a detailed study of representative test cases, including static and oscillating bubble configurations. These numerical experiments are designed to assess the solvability and stability of the proposed methodology. To achieve reliable spatial resolution, higher-order finite element approximations are employed. The influence of surface tension effects, the choice of temporal discretization scheme, and the limitations imposed by the capillary time step restriction are also addressed.

Chapter 6 is dedicated to the numerical investigation of the well-established rising bubble benchmark (test case 1 and 2), as it constitute a stringent validation procedure for multiphase flow solvers due to the presence of pronounced interfacial deformations and possible topological changes. By tackling these challenges, the benchmarks provide a rigorous evaluation of the accuracy and robustness of the proposed method. All simulations are carried out within the in-house CFD software framework FeatFlow, which has been

developed in C programming environment.

Chapter 7 introduces a distancing-free variant of the proposed formulation, wherein the fluid interface is represented through a color (indicator) function, denoted by $\psi_I(\mathbf{x},t)$. The advection of this function is designed to be strictly mass conservative, thereby eliminating the need for any redistancing procedure. The effectiveness of this strategy within the curvature free material cut-off framework is tested by revisiting the rising bubble benchmark (test case 1 and 2).

Chapter 8 concludes the dissertation by summarizing the main contributions and outlining perspectives for future research. A comprehensive list of references is provided at the end.

1.4 Already Published Contributions

- [23] M. A. Afaq, S. Turek, A. Ouazzi, and A. Fatima. Monolithic Newton-multigrid solver for multiphase flow problems with surface tension. In Book of Extended Abstracts of the 6th ECCOMAS Young Investigators Conference 7th-9th July 2021, Valencia, Spain, pages 190-199, Valencia, Spain, 2021. Editorial Universitat Polit‘ecnica de Valencia.

- [24] A. Fatima, S. Turek, A. Ouazzi, and M. A. Afaq. An adaptive discrete Newton method for regularization-free bingham model. In Book of Extended Abstracts of the 6th ECCOMAS Young Investigators Conference 7th-9th July 2021, Valencia, Spain, pages 180-189, Valencia, Spain, 2021. Editorial Universitat Polit‘ecnica de Valencia.

- [25] M. A. Afaq, A. Fatima, S. Turek, and A. Ouazzi. Robust Monolithic Multigrid FEM Solver for Three Field Formulation of Incompressible Flow Problems, Ergebnisberichte des Instituts für Angewandte Mathematik Nummer 659, Fakultät für Mathematik, TU Dortmund, 659, 2023.

2

Mathematical Modelling

As outlined in Chapter 1, interface capturing strategies constitute a computationally efficient framework for simulating multiphase flows. These approaches avoid explicit interface reconstruction and instead embed the interface implicitly within the computational domain. Among the various techniques available, the level set method [14, 15, 16, 17, 18] has emerged as one of the most prominent techniques. The popularity of this method arises from its mathematical elegance and inherent ability to represent complex interface dynamics, such as topological changes due to droplet coalescence or breakup.

The first part of this chapter is devoted to the mathematical formulation and numerical treatment of interfacial forces in the context of the level set framework. A central aspect is the incorporation of surface tension forces into the governing equations of incompressible multiphase flows. The flow dynamics are described by the classical incompressible Navier-Stokes equations, along with the force terms as follows

$$\begin{cases} \rho\left(\dfrac{\partial \mathbf{u}}{\partial t} + \mathbf{u}\cdot\nabla\mathbf{u}\right) - \nabla\cdot 2\mu\mathbf{D}(\mathbf{u}) + \nabla p = \mathbf{f} \quad \text{in } \Omega, \\ \nabla\cdot\mathbf{u} = 0 \quad \text{in } \Omega, \end{cases} \tag{2.0.1}$$

where ρ denotes the fluid density, $\mathbf{u}$ represents the velocity field, μ is the dynamic viscosity, and $\mathbf{D}(\mathbf{u}) = \frac{1}{2}(\nabla\mathbf{u} + \nabla\mathbf{u}^{\mathrm{T}})$ is the deformation tensor. The variable p corresponds to the pressure field, while $\mathbf{f}$ accounts for external forces, including surface tension effects.

For Eulerian interface capturing methods, where the interface does not coincide with the underlying grid, a standard and widely implemented approach for introducing surface

tension is the CSF model [21]. In this formulation, the sharp fluid-fluid interface is replaced by a thin transition layer across which the surface tension force is smoothly distributed. This diffuse representation ensures compatibility with the discretized governing equations and mitigates numerical instabilities associated with sharp discontinuities. A detailed overview of the theoretical foundations and computational consequences of this method can be found in [21].

The second part of this chapter establishes the formal connection between the CSF approach [21] and the alternative CSS formulation [19]. Whereas CSF introduces interfacial effects in the form of localized body forces, the CSS methodology reformulates the surface tension contribution as the divergence of a stress tensor. This stress-based representation offers several notable advantages such as, it eliminates the explicit evaluation of interface curvature, provides improved numerical stability, and facilitates a more consistent treatment of interfacial stresses. For a summary of these aspects, including comparative insights into both methods, the reader is referred to [20].

2.1 Continuum Surface Force (CSF)

The continuum surface force (CSF), first proposed by Brackbill et al. [21], provides a framework for modeling surface tension in multiphase flows by representing it as a smoothly distributed volumetric force rather than enforcing it strictly at the sharp interface. This conceptual shift obviates the need for explicit interface reconstruction, significantly simplifying the numerical implementation of surface tension effects within an Eulerian formulation.

In the CSF approach, the surface tension force $\mathbf{f}$ is formulated using a Dirac delta function to localize its influence near the interface Γ as

$$\mathbf{f} = \kappa\sigma\mathbf{n}\delta_\Gamma, \tag{2.1.1}$$

where κ is the curvature of the interface, σ denotes the surface tension coefficient, $\mathbf{n}$ is a unit normal vector to the interface, and δ_Γ is the Dirac delta function, ensuring that the force is concentrated in the vicinity of Γ. This force term is incorporated as a source term in the momentum equation of the incompressible Navier-Stokes system (2.0.1), enabling surface tension to be treated naturally within a fixed Eulerian grid.

A key assumption underlying the CSF formulation is that the surface tension acts continuously across a thin transition layer, rather than being imposed strictly at a discrete

interface. To achieve this, the Dirac delta function is regularized over a finite thickness ϵ, providing a smooth distribution of the force across the interface

$$\delta_\Gamma^\epsilon(\mathbf{x}) = \begin{cases} \frac{1}{\epsilon}\Pi\Big(\frac{\text{dist}_\Gamma(\mathbf{x})}{\epsilon}\Big) & \text{if} \quad \text{dist}_\Gamma(\mathbf{x}) \leq \epsilon, \\ 0 & \text{if} \quad \text{dist}_\Gamma(\mathbf{x}) > \epsilon, \end{cases} \tag{2.1.2}$$

where ϵ is the regularization parameter, defining the effective thickness of the interface, $\text{dist}_\Gamma(\mathbf{x})$ is the signed distance function to the interface [26, 27], and Π is a smooth polynomial function [28], typically chosen as

$$\Pi(z) = \Big(\frac{35}{32}\Big)(1 - 3z^2 + 3z^4 - z^6), \tag{2.1.3}$$

which ensures a smooth and compact support for the regularized force.

By incorporating the CSF force term, the incompressible Navier-Stokes equations for multiphase flows can be expressed as

$$\begin{cases} \rho\Big(\frac{\partial \mathbf{u}}{\partial t} + \mathbf{u}\cdot\nabla\mathbf{u}\Big) - \nabla\cdot 2\mu\mathbf{D}(\mathbf{u}) + \nabla p = \kappa\sigma\mathbf{n}\delta_\Gamma & \text{in } \Omega, \\ \nabla\cdot\mathbf{u} = 0 & \text{in } \Omega. \end{cases} \tag{2.1.4}$$

Here, the fluid properties, namely density ρ and dynamic viscosity μ, are allowed to vary spatially across different phases, reflecting the heterogeneous nature of the multiphase system. This formulation provides a robust and numerically convenient method for capturing the effects of surface tension without explicitly tracking the interface, while maintaining the consistency and stability of the underlying flow solver.

2.1.1 Level Set Method

The level set method, originally formulated by Osher and Sethian in 1988 [14], represents a sophisticated mathematical framework for tracking the evolving interfaces in multiphase flow problems. This method employs an implicit representation of the interface by embedding it within a higher-dimensional, continuously differentiable function, defined over the entire computational domain Ω. The temporal evolution of this function is governed by the level set transport equation

$$\frac{\partial}{\partial t}\phi(\mathbf{x},t) + \mathbf{u}\cdot\nabla\phi(\mathbf{x},t) = 0 \quad \text{in } \Omega, \tag{2.1.5}$$

where $\phi(\mathbf{x},t)$ is the level set function and $\mathbf{u}$ represents the velocity field. In the case of a two-phase flow involving immiscible fluids, the level set function naturally distinguishes between the two fluid phases through its sign, assigning positive values to one phase and negative values to the other. The interface Γ, which separates these two phases, is implicitly defined as the zero level set of the function, represented as

$$\Gamma = \{\mathbf{x} \in \Omega \mid \phi(\mathbf{x},t) = 0\}. \tag{2.1.6}$$

This implicit formulation offers a powerful and flexible approach for capturing complex topological changes, without requiring explicit reconstruction of the interface geometry. The general definition of the interface, as introduced in equation (2.1.6), is very flexible. However, in order to accurately capture the interface in numerical simulations, certain requirements must be satisfied [29]. Specifically, the level set function ϕ should at least be continuous, ensuring a well defined description of the interface. Furthermore, the evaluation of the interface normal vector is necessary in most applications, since it directly enters the computation of curvature and surface tension forces.

To simultaneously satisfy these requirements, a particularly convenient and widely adopted choice for the level set function is the signed distance function [26], presented in Fig. 2.1. This definition satisfies the property that the gradient of ϕ has unit magnitude almost everywhere in the computational domain i.e. $\|\nabla\phi\| = 1$, which greatly simplifies numerical differentiation and stabilizes the computation of geometric quantities associated with the interface. However, numerical discretization may cause deviations from this property over time, necessitating periodic reinitialization (redistancing) to restore the signed distance function structure.

Definition: Signed Distance Function

The signed distance function to Γ is the function $\phi : [0,T] \times \Omega \to \mathbb{R}$ defined by

$$\phi(\mathbf{x},t) = \begin{cases} \operatorname{dist}(\mathbf{x},\Gamma) & \text{for} \quad \mathbf{x} \in \Omega_1, \\ 0 & \text{for} \quad \mathbf{x} \in \Gamma, \\ -\operatorname{dist}(\mathbf{x},\Gamma) & \text{for} \quad \mathbf{x} \in \Omega_2, \end{cases} \tag{2.1.7}$$

where $\operatorname{dist}(\mathbf{x},\Gamma)$ represents the minimum Euclidean distance from a point $\mathbf{x}$ to the interface Γ. The interface normal vector $\mathbf{n}$ and the curvature κ are determined as follows

$$\mathbf{n} = \frac{\nabla\phi}{\|\nabla\phi\|}, \quad \kappa = -\nabla \cdot \mathbf{n}, \tag{2.1.8}$$

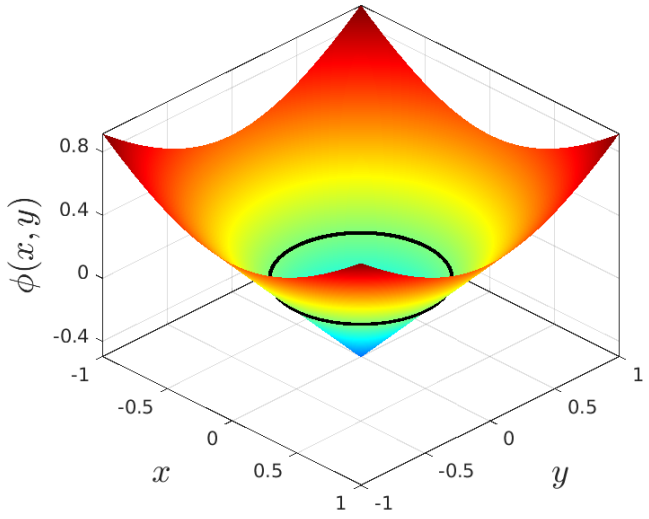

Figure 2.1: Signed distance function with zero level set contour.

where the unit normal vector $\mathbf{n}$ is computed as the gradient of the level set function normalized by its magnitude, provided that $\|\nabla\phi\| \neq 0$. The sign of the curvature κ dictates the directionality of the surface tension force, with $\mathbf{n}$ conventionally pointing into the region where $\phi > 0$ [30]. The complete system of governing equations incorporating the level set formulation is given as

$$\begin{cases} \rho(\phi)\left(\dfrac{\partial \mathbf{u}}{\partial t} + \mathbf{u}\cdot\nabla\mathbf{u}\right) - \nabla\cdot 2\mu(\phi)\mathbf{D}(\mathbf{u}) + \nabla p = \kappa\sigma\mathbf{n}\delta_\Gamma(\phi) & \text{in } \Omega, \\ \nabla\cdot\mathbf{u} = 0 & \text{in } \Omega, \\ \dfrac{\partial\phi}{\partial t} + \mathbf{u}\cdot\nabla\phi = 0 & \text{in } \Omega. \end{cases} \tag{2.1.9}$$

This three-field coupled system accounts the surface tension as a volumetric force term. The density $\rho(\phi)$ and dynamic viscosity $\mu(\phi)$ are phase-dependent functions, varying across the interface to reflect the distinct properties of the two fluid phases.

2.2 Towards the CSS Formulation

In the previously established formulation, the surface tension force is incorporated into the incompressible Navier-Stokes equations as a volumetric term. However, this approach still requires the explicit evaluation of interface curvature and normal vectors. The direct computation of these geometric quantities is often problematic: normals derived from discrete interface functions are prone to numerical oscillations, while curvature calculations

amplify discretization errors, leading to spurious currents and loss of accuracy near the interface, a detailed study on the curvature evaluation and its effects is given in [31]. To circumvent these problems, it is advantageous to express the surface tension force in the form of divergence of a stress tensor, as in the continuum surface stress (CSS) methodology. Transitioning from the traditional CSF approach to CSS involves redefining the interface-representing function as a material cut-off function rather than a level set function. This material cut-off function is defined as

$$\psi(\mathbf{x},t) = \begin{cases} +\frac{1}{2} & \text{if} \quad \phi(\mathbf{x},t) \geq 0, \\ -\frac{1}{2} & \text{if} \quad \phi(\mathbf{x},t) < 0, \end{cases} \tag{2.2.1}$$

where $\psi(\mathbf{x},t)$ serves as an indicator distinguishing the two fluid phases.

For numerical implementation, the material cut-off function ψ is typically regularized to ensure smoothness across the interface. A common choice is a sigmoid function [32]

$$\psi = \frac{-1}{1+\exp\left(\frac{\phi}{\epsilon}\right)} + 0.5. \tag{2.2.2}$$

where ϵ is a small positive parameter controlling the transition width, thereby providing a continuous and differentiable representation of the interface.

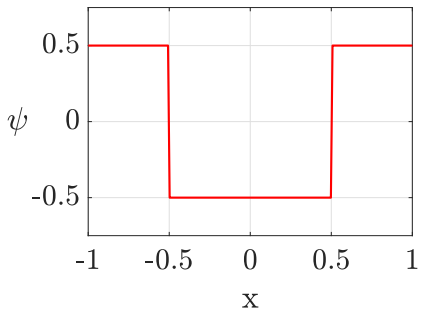

Figure 2.2: Sigmoid function

The rationale for not using the level set function lies in its gradient: The level set gradient behaves as a regular vector field and does not localize sharply at the interface. In contrast, the gradient of the indicator function is strictly supported at the interface and oriented correctly. This property enables a straightforward reformulation of the surface tension force [22] and is formally expressed as

$$\mathbf{n}\delta_\Gamma = \mathbf{n}\delta_{(\phi=0)} = \nabla\psi(\phi). \tag{2.2.3}$$

This property offers several computational advantages. It eliminates the need for explicit curvature reconstruction while allowing the straightforward construction of dyadic products such as $\nabla\psi \otimes \nabla\psi$, which inherently encode the interface geometry. Taking the divergence of this tensor naturally yields the correct surface stress distribution.

Consequently, the surface tension force can be represented as a domain-integrated volumetric force

$$\mathbf{f} = \sigma\kappa\nabla\psi. \tag{2.2.4}$$

The resulting governing system, incorporating this modified surface tension representation, is expressed as

$$\begin{cases} \rho(\psi)\left(\dfrac{\partial \mathbf{u}}{\partial t} + \mathbf{u}\cdot\nabla\mathbf{u}\right) - \nabla\cdot 2\mu(\psi)\mathbf{D}(\mathbf{u}) + \nabla p = \kappa\sigma\nabla\psi & \text{in } \Omega, \\ \nabla\cdot\mathbf{u} = 0 & \text{in } \Omega, \\ \dfrac{\partial\phi}{\partial t} + \mathbf{u}\cdot\nabla\phi = 0 & \text{in } \Omega, \\ \psi = \dfrac{-1}{1+\exp(\frac{\phi}{\epsilon})} + 0.5 \end{cases} \tag{2.2.5}$$

As it is already mentioned above, the numerical computation of interface normals and curvature constitutes a primary source of discretization errors, making it a computationally challenging task. CSS, introduced by Lafaurie et al. [19] and refined by other researchers, provides an alternative approach to overcome the reasons of inaccuracies and spurious oscillations. The reformulation of CSF force in terms of stress-tensor based formulation is given in the next section.

2.3 Continuum Surface Stress (CSS)

By taking the advantage of the properties of material cut-off function introduced in (2.2.1), the surface tension force is given as

$$\mathbf{f} = \sigma\kappa\nabla\psi. \tag{2.3.1}$$

Substituting the value of curvature κ in the above equation

$$\mathbf{f} = -\sigma\nabla\cdot\Big(\nabla\psi\frac{1}{\|\nabla\psi\|}\Big)\nabla\psi, \tag{2.3.2}$$

applying the divergence operator using product rule

$$\mathbf{f} = -\sigma\Big(\frac{\nabla\cdot\nabla\psi}{\|\nabla\psi\|}\Big)\nabla\psi - \sigma\Big(\nabla\Big(\frac{1}{\|\nabla\psi\|}\Big)\cdot\nabla\psi\Big)\nabla\psi. \tag{2.3.3}$$

Let $q := \|\nabla\psi\|$, and substitute in the second part of the above equation

$$\mathbf{f} = -\sigma\Big(\frac{\nabla\cdot\nabla\psi}{\|\nabla\psi\|}\Big)\nabla\psi - \sigma\Big(\nabla\Big(\frac{1}{q}\Big)\cdot\nabla\psi\Big)\nabla\psi. \tag{2.3.4}$$

Calculating

$$\nabla\Big(\frac{1}{q}\Big) = -\frac{1}{q^3}H(\psi)\nabla\psi, \tag{2.3.5}$$

where $H(\psi) = \partial_i\partial_k\psi$ is the Hessian operator, by substituting the values in equation (2.3.4) results

$$\mathbf{f} = -\sigma\Big(\frac{\nabla\cdot\nabla\psi}{\|\nabla\psi\|}\Big)\nabla\psi + \sigma\Big(\Big(\frac{1}{\|\nabla\psi\|^3}H(\psi)\nabla\psi\Big)\cdot\nabla\psi\Big)\nabla\psi. \tag{2.3.6}$$

By using the identity $\nabla\|\nabla\psi\| = \frac{H(\psi)\nabla\psi}{\|\nabla\psi\|}$, we obtain

$$\mathbf{f} = -\sigma\underbrace{\Big(\frac{\nabla\cdot\nabla\psi}{\|\nabla\psi\|}\Big)\nabla\psi}_{:=A} + \sigma\underbrace{\Big(\frac{\nabla\|\nabla\psi\|\cdot\nabla\psi}{\|\nabla\psi\|^2}\Big)\nabla\psi}_{:=B}. \tag{2.3.7}$$

Simplifying the term B, we get

$$\begin{aligned} B &= \nabla\psi\frac{\nabla\psi\cdot\nabla\|\nabla\psi\|}{\|\nabla\psi\|^2} \\ &= \frac{(\nabla\psi\otimes\nabla\psi)\nabla\|\nabla\psi\|}{\|\nabla\psi\|^2} \\ &= (\mathbf{n}\otimes\mathbf{n})\nabla\|\nabla\psi\|. \end{aligned} \tag{2.3.8}$$

This is the projection of $\nabla\|\nabla\psi\|$ onto the normal direction, therefore

$$(\mathbf{n}\otimes\mathbf{n})\nabla\|\nabla\psi\| - \nabla\|\nabla\psi\| = -\underbrace{(I-\mathbf{n}\otimes\mathbf{n})}_{P_s}\nabla\|\nabla\psi\|, \tag{2.3.9}$$

the matrix $P_s := I - \mathbf{n} \otimes \mathbf{n}$ is the projection, applying P_s to a gradient gives the tangential gradient ∇_s, and $\nabla_s \|\nabla\psi\| = 0$ [22]. Hence, the equation (2.3.9) reduces to

$$\frac{(\nabla\psi \otimes \nabla\psi)}{\|\nabla\psi\|^2} \nabla \|\nabla\psi\| - \nabla \|\nabla\psi\| = 0, \tag{2.3.10}$$

$$\frac{(\nabla\psi \otimes \nabla\psi)}{\|\nabla\psi\|^2} \nabla \|\nabla\psi\| = \nabla \|\nabla\psi\|. \tag{2.3.11}$$

By substituting the simplified expression of B into the second part of equation (2.3.7), we obtain

$$\mathbf{f} = -\sigma \Big\{ \underbrace{\Big(\frac{\nabla \cdot \nabla\psi}{\|\nabla\psi\|} \Big) \nabla\psi}_{A} - \nabla \|\nabla\psi\| \Big\}. \tag{2.3.12}$$

Moreover, for simplifying the term A, define $T := \nabla\psi \otimes \nabla\psi$. The component wise product for $(\nabla \cdot T)_i = \partial_j T_{ij}$, gives $(\nabla \cdot T)_i = \Big(H(\psi)\nabla\psi \Big)_i + (\nabla^2\psi)\partial_i\psi$, and in vector notation

$$\nabla \cdot (\nabla\psi \otimes \nabla\psi) = H(\psi)\nabla\psi + (\nabla^2\psi)\nabla\psi, \tag{2.3.13}$$

rearrange

$$\nabla \cdot (\nabla\psi \otimes \nabla\psi) - H(\psi)\nabla\psi = (\nabla^2\psi)\nabla\psi. \tag{2.3.14}$$

From the calculations of (2.3.5), $\nabla \|\nabla\psi\|^2 = 2H(\psi)\nabla\psi$, rearranging results $\frac{1}{2}\nabla \|\nabla\psi\|^2 = H(\psi)\nabla\psi$, and substituting in equation (2.3.14) results in

$$\nabla \cdot (\nabla\psi \otimes \nabla\psi) - \frac{1}{2}\nabla \|\nabla\psi\|^2 = (\nabla^2\psi)\nabla\psi. \tag{2.3.15}$$

The term A simplifies as

$$\frac{(\nabla^2\psi)\nabla\psi}{\|\nabla\psi\|} = \frac{\nabla \cdot \overbrace{(\nabla\psi \otimes \nabla\psi)}^{:=F}}{\|\nabla\psi\|} - \underbrace{\frac{\nabla \|\nabla\psi\|^2}{2\|\nabla\psi\|}}_{:=C}, \tag{2.3.16}$$

in terms of q, $C := \frac{1}{2}\frac{\nabla q^2}{q} = \frac{1}{2}\left(\frac{2q\nabla q}{q}\right) = \nabla q$. Furthermore, the expansion of first term F

$$\left(\frac{\nabla \cdot F}{q}\right) = \nabla \cdot \left(\frac{F}{q}\right) + \frac{(F)\nabla q}{q^2}, \tag{2.3.17}$$

by substituting back the simplified forms of C and F in equation (2.3.16), we obtain

$$\frac{(\nabla^2\psi)\nabla\psi}{\|\nabla\psi\|} = \nabla \cdot \left(\frac{\nabla\psi \otimes \nabla\psi}{\|\nabla\psi\|}\right) + \frac{(\nabla\psi \otimes \nabla\psi)\nabla\|\nabla\psi\|}{\|\nabla\psi\|^2} - \nabla\|\nabla\psi\|, \tag{2.3.18}$$

rearranging

$$\frac{(\nabla^2\psi)\nabla\psi}{\|\nabla\psi\|} = \nabla \cdot \left(\frac{\nabla\psi \otimes \nabla\psi}{\|\nabla\psi\|}\right) + \underbrace{\left(\frac{(\nabla\psi \otimes \nabla\psi)}{\|\nabla\psi\|^2} - I\right)\nabla\|\nabla\psi\|}_{=\nabla_s\|\nabla\psi\|=0}. \tag{2.3.19}$$

The final form of equation (2.3.7) can be expressed as

$$\mathbf{f} = -\sigma\left\{\nabla \cdot \left(\frac{\nabla\psi \otimes \nabla\psi}{\|\nabla\psi\|}\right) - \nabla\|\nabla\psi\|\right\}. \tag{2.3.20}$$

This expression represents the surface tension force in terms of the indicator function ψ, thereby eliminating the need for explicit curvature computation.

To further suppress spurious pressure oscillations that may arise near the fluid interface, a modified pressure field p_m, is introduced. This pressure adjustment compensates for the capillary pressure gradient by incorporating the term $\sigma\nabla\|\nabla\psi\|$ into the pressure balance [22], leading to

$$\nabla p_m = \nabla p - \nabla(\sigma\|\nabla\psi\|). \tag{2.3.21}$$

The first term of equation (2.3.7) is consequently treated as an additional contribution to the total stress tensor in the Navier-Stokes equations. Thus, the conventional Cauchy stress tensor τ_s, and its stress-modified counterpart τ_m are defined as

$$\tau_s = 2\mu(\psi)\mathbf{D}(\mathbf{u}), \qquad \tau_m = -\sigma\left(\frac{\nabla\psi \otimes \nabla\psi}{\|\nabla\psi\|}\right). \tag{2.3.22}$$

The resulting system of governing equations therefore takes the form

$$\begin{cases} \rho\Big(\dfrac{\partial \mathbf{u}}{\partial t} + \mathbf{u}\cdot\nabla\mathbf{u}\Big) - \nabla\cdot\Big(2\mu\mathbf{D}(\mathbf{u}) + \sigma\Big(\dfrac{\nabla\psi\otimes\nabla\psi}{\|\nabla\psi\|}\Big)\Big) + \nabla p = 0 & \text{in } \Omega, \\ \nabla\cdot\mathbf{u} = 0 & \text{in } \Omega, \\ \dfrac{\partial\phi}{\partial t} + \mathbf{u}\cdot\nabla\phi = 0 & \text{in } \Omega, \\ \psi = \dfrac{-1}{1+\exp\left(\frac{\phi}{\epsilon}\right)} + 0.5 \end{cases} \tag{2.3.23}$$

This CSS formulation incorporates the capillary effects directly into the total stress tensor, thereby eliminating the explicit dependence on curvature and normal vector evaluation. By redistributing the surface tension force smoothly across the interfacial region, the method enhances numerical robustness and mitigates parasitic currents while maintaining an accurate representation of interfacial dynamics.

Nevertheless, the approach still relies on the level set function to capture interface motion, which requires periodic reinitialization to preserve interface sharpness and volume conservation. To address this, refined level set strategies have been developed, most notably the modified level set method with implicit reinitialization within a two-step advection framework proposed in [32]. The subsequent section provides a detailed discussion of this methodology, including its theoretical formulation and computational implementation aspects.

2.4 Reinitialization

Olsson and Kreiss [32] conducted a series of numerical experiments employing total variation diminishing (TVD) schemes, where the finite element method was utilized for spatial discretization. Their investigation revealed that, even with the implementation of well-established limiter functions, the interface thickness and profile were not consistently maintained throughout the simulation. To mitigate this deficiency, they identified the necessity of incorporating an artificial compression mechanism [33]. In response, they introduced a corrective term known as the compression flux, expressed as $\phi(1-\phi)$.

Furthermore, their numerical findings underscored the dependency of the interface profile on the orientation of the interface normals, thereby necessitating the application of the compression flux exclusively in the direction normal to the interface. Consequently, the compression flux is formulated as $\phi(1-\phi)\mathbf{n}$, where the level set function ϕ is constrained within the range $0 < \phi < 1$. Additionally, to ensure proper redistribution of the interface, a

diffusion term of the form $\nabla\phi \cdot \mathbf{n}$ is introduced, acting solely in the compression direction. The combination of these two terms yields an intermediate reinitialization equation within the formulation proposed by Olsson and Kreiss [32] as follows

$$\frac{\partial \phi}{\partial \tau} + \nabla \cdot \Big(\phi(1-\phi)\mathbf{n}\Big) - \nabla \cdot \Big(\gamma(\nabla\phi \cdot \mathbf{n})\mathbf{n}\Big) = 0. \tag{2.4.1}$$

The level set methodology proposed in this framework operates through a sequential two-step procedure. In the initial step, the transport equation for the level set function (2.1.5) is solved to advect the interface. Subsequently, a separate reinitialization step (2.4.1) is executed in fictitious time τ to restore the signed distance property of the level set function.

A key advantage of this approach is its ability to achieve a well-balanced interplay between compression and diffusion effects, thereby eliminating the need for additional artificial diffusion to stabilize the transport equation of ϕ [32]. However, a notable limitation of this formulation is the dependency of numerical stability on the choice of $\Delta\tau$. Excessively large values of $\Delta\tau$ may induce instabilities or spurious oscillations at the interface, undermining the accuracy of the method.

To circumvent these limitations, it would be beneficial to integrate the reinitialization process directly within the transport equation, enabling real-time interface preservation while maintaining the signed distance function properties. An approach that achieves this objective is the strategy introduced by T. Coupez [34], which is briefly outlined in the following section.

2.5 T. Coupez Strategy

To achieve real-time reinitialization of the level set function while preserving its essential properties, T. Coupez [34] proposed the incorporation of the convective derivative term directly into the reinitialization equation. This approach ensures the conservation of the level set function's fundamental properties, specifically maintaining the signed distance function condition, expressed as $\|\nabla\phi\| = 1$ and $\mathbf{n} \cdot \nabla\phi = 1$. The reinitialization equation is formulated as follows

$$\begin{cases} \dfrac{d\phi}{d\tau} + \nabla \cdot [(\mathbf{n} \cdot \nabla\phi - 1)\mathbf{n}] = 0, \\ \qquad\qquad\qquad \phi(\tau = 0) = \phi(t). \end{cases} \tag{2.5.1}$$

To establish a connection between the real (physical) time and the fictitious reinitialization time τ, the chain rule is applied, yielding the following relationship

$$\frac{d\phi}{dt} = \frac{\partial \phi}{\partial \tau}\frac{\partial \tau}{\partial t}. \tag{2.5.2}$$

Expanding this equation in terms of advection, we obtain

$$\frac{\partial \phi}{\partial \tau}\frac{\partial \tau}{\partial t} = \frac{\partial \phi}{\partial t} + \mathbf{u}\cdot\nabla\phi, \tag{2.5.3}$$

where $\mathbf{u}$ represents the velocity field governing the transport of the level set function. Introducing a scaling parameter γ to regulate the fictitious time evolution, we redefine the equation as

$$\frac{\partial \phi}{\partial \tau}\gamma = \frac{\partial \phi}{\partial t} + \mathbf{u}\cdot\nabla\phi. \tag{2.5.4}$$

Rearranging for $\frac{\partial \phi}{\partial \tau}$, we obtain

$$\frac{\partial \phi}{\partial \tau} = \frac{1}{\gamma}\frac{\partial \phi}{\partial t} + \frac{1}{\gamma}\mathbf{u}\cdot\nabla\phi. \tag{2.5.5}$$

Substituting this expression into the reinitialization equation results in the following governing equation for real-time reinitialization

$$\begin{cases} \dfrac{1}{\gamma}\dfrac{\partial \phi}{\partial t} + \dfrac{1}{\gamma}\mathbf{u}\cdot\nabla\phi + \nabla\cdot[(\mathbf{n}\cdot\nabla\phi - 1)\mathbf{n}] = 0, \\ \phi(t=0) = \phi_0. \end{cases} \tag{2.5.6}$$

Multiplying both sides by γ leads to a more compact form

$$\begin{cases} \dfrac{\partial \phi}{\partial t} + \mathbf{u}\cdot\nabla\phi + \gamma\nabla\cdot[(\mathbf{n}\cdot\nabla\phi - 1)\mathbf{n}] = 0, \\ \phi(t=0) = \phi_0. \end{cases} \tag{2.5.7}$$

To derive the weak form of the equation, we multiply it by a test function Φ and integrate over the computational domain Ω

$$\int_\Omega \frac{\partial \phi}{\partial t}\Phi\, dx + \int_\Omega (\mathbf{u}\cdot\nabla\phi)\Phi\, dx + \int_\Omega \gamma\nabla\cdot[(\mathbf{n}\cdot\nabla\phi - 1)\mathbf{n}]\Phi\, dx = 0. \tag{2.5.8}$$

Applying integration by parts to the divergence term and assuming natural boundary conditions, we obtain

$$\int_\Omega \frac{\partial \phi}{\partial t}\Phi\, dx + \int_\Omega (\mathbf{u}\cdot\nabla\phi)\Phi\, dx + \int_\Omega \gamma(\mathbf{n}\cdot\nabla\phi)(\mathbf{n}\cdot\nabla\Phi)\, dx - \int_{\partial\Omega} \gamma(\mathbf{n}\cdot\nabla\Phi)\, dx = 0. \tag{2.5.9}$$

This formulation effectively integrates the reinitialization step within the level set transport equation, thereby preserving the signed distance function properties throughout the simulation while ensuring numerical stability.

2.6 Curvature Free Material Cut-off Formulation

To fully exploit the advantages of the CSS formulation and the inherent properties of the material cut-off function, the conventional level set transport equation is replaced by a new governing equation for the material cut-off variable ψ. The function ψ is bounded within the interval $-0.5 \leq \psi \leq 0.5$, which ensures a sharply defined yet smoothly varying interface representation between the two immiscible phases.

To implicitly incorporate the reinitialization process within the advection dynamics thereby avoiding separate reinitialization steps, a modified transport equation for ψ is formulated. Based on the definition of the material cut-off function in equation (2.2.1), a compression flux term analogous to that proposed by [32] is introduced as

$$\gamma_1(0.5+\psi)(0.5-\psi)\mathbf{n}, \tag{2.6.1}$$

which acts in the direction of the interface normal $\mathbf{n}$. This term effectively compresses the transition zone, maintaining a sharp interface profile during advection.

However, excessive compression may induce numerical instabilities and artificial oscillations. To counterbalance this effect, a stabilizing diffusion term is added, acting only in the normal direction [22]

$$\gamma_2(\nabla\psi\cdot\mathbf{n})\mathbf{n}. \tag{2.6.2}$$

The combination of these two opposing fluxes (with their corresponding magnitudes γ_1 and γ_2) ensures that the interface thickness remains consistent while preserving numerical stability and phase conservation.

Accordingly, the complete set of governing equations for the CSS framework, expressed in physical time, is written as

$$\begin{cases} \rho(\psi)\left(\dfrac{\partial \mathbf{u}}{\partial t}+\mathbf{u}\cdot\nabla\mathbf{u}\right)-\nabla\cdot\Big(\underbrace{\underbrace{2\mu(\psi)\mathbf{D}(\mathbf{u})}_{\tau_s}+\underbrace{\sigma\left(\dfrac{\nabla\psi\otimes\nabla\psi}{\|\nabla\psi\|}\right)}_{\tau_m}}_{\tau=\tau_s+\tau_m}\Big)+\nabla p=0 \quad \text{in } \Omega, \\ \nabla\cdot\mathbf{u}=0 \quad \text{in } \Omega, \\ \dfrac{\partial\psi}{\partial t}+\mathbf{u}\cdot\nabla\psi+\nabla\cdot\left(\gamma_1(0.5+\psi)(0.5-\psi)\dfrac{\nabla\psi}{\|\nabla\psi\|}\right)-\nabla\cdot\left(\gamma_2(\nabla\psi\cdot\dfrac{\nabla\psi}{\|\nabla\psi\|})\dfrac{\nabla\psi}{\|\nabla\psi\|}\right)=0 \quad \text{in } \Omega. \end{cases} \tag{2.6.3}$$

This coupled system comprising the momentum balance, incompressibility constraint, and the evolution equation for ψ is solved in a monolithic framework. The implicit integration of reinitialization within the advection term eliminates the need for an explicit reinitialization equation, reducing both numerical complexity and computational overhead.

The final equation in system (2.6.3) is specifically constructed to ensure mass conservation. In its continuous form, the integral quantity

$$\int_\Omega \psi\, dx, \tag{2.6.4}$$

remains invariant in time, implying that the total volume of each phase is preserved. The numerical conservation properties of ψ, along with their implementation and validation, are discussed in detail in Chapter 4.

From a methodological perspective, the CSF formulation, though widely adopted in CFD solvers employing level set or volume of fluid (VOF) methods, suffers from inaccuracies due to curvature computation errors, which often generate spurious currents at the interface. In contrast, the CSS formulation integrates surface tension effects directly into the stress tensor, providing a more physically consistent and numerically stable approach. This comes at the cost of increased computational effort and algorithmic complexity.

In high fidelity simulations, such as those involving microfluidic flows, droplet dynamics, and multiphase interfacial interactions, the CSS formulation is particularly advantageous. Its capability to preserve interface sharpness, maintain strict mass conservation, and suppress nonphysical pressure oscillations makes it the preferred choice for accurate and stable multiphase flow modeling. Consequently, the present work adopts the CSS framework to develop a robust and reliable numerical solver tailored for complex two-phase flow problems.

A comparative overview of the CSF and CSS methodologies, highlighting their respective advantages, limitations, and implementation considerations, is summarized in Table 2.1.

Table 2.1: Comparison between the CSF and CSS formulations for modeling surface tension effects in multiphase flows.

Aspect	CSF	CSS
Formulation Basis	Surface tension represented as a volumetric body force concentrated at the interface.	Surface tension expressed as the divergence of a capillary stress tensor, continuously distributed across the interface.
Interface Representation	Typically based on a level set or VOF function.	Employs a material cut-off function defining the interfacial zone.
Curvature and Normal Computation	Requires explicit evaluation of curvature and interface normals, which can introduce numerical errors.	Avoids direct curvature computation; interfacial effects captured through tensor divergence.
Numerical Stability	Susceptible to spurious currents near the interface due to curvature discretization.	Enhanced stability since capillary stresses are smoothly distributed within the stress tensor.
Mass Conservation	Dependent on interface capturing method (e.g. reinitialization for level set).	Inherently conservative when solved in the flux form [35] (e.g. Olsson-Kreiss formulation).
Implementation Complexity	Straightforward implementation; widely integrated into existing CFD solvers.	Requires more complex tensor operations and coupling with the transport of ψ.
Computational Cost	Lower, as curvature and normal computations are localized.	Higher, due to tensor divergence and gradient evaluations.

3

Finite Element Method for Stokes Equations

For the numerical solution of partial differential equations (PDEs), several methodologies are available for the spatial discretization, among which the most commonly employed are the finite difference method (FDM) [36, 37, 38], the finite volume method (FVM) [39, 40], and the finite element method (FEM) [41, 42]. While FDM and FVM have been traditionally used across various engineering applications, the FEM represents a more modern approach. Initially this method was developed within the context of structural and solid mechanics. However, in recent years, FEM has gained significant traction across a broad spectrum of scientific and engineering disciplines, including computational fluid dynamics, heat transfer, electromagnetics, and biomechanics.

The primary advantage of FEM lies in its exceptional flexibility in dealing with complex geometries, irregular domains, and intricate boundary conditions, which often pose significant challenges for other discretization methods. In addition, it enables robust and highly accurate solutions to boundary value problems by leveraging a weak formulation of the original PDEs [43].

The core principle of FEM involves reformulating the governing differential equations into a weak form. Which is accomplished by multiplying the original (strong form) equations by a set of test functions, integrating over the entire computational domain, and applying integration by parts where necessary, to reduce the order of derivatives. This transformation yields a system of equations that is more amenable to numerical approximation.

Therefore, instead of seeking an exact solution to the differential equations, FEM

constructs an approximate solution within a finite-dimensional subspace, defined by basis functions (often piecewise polynomials) over a discretized domain composed of finite elements. The accuracy of the approximated solution can be enhanced through mesh refinement (h-refinement), which involves decreasing the size of the elements, or by increasing the order of the polynomial interpolation functions (p-refinement). These refinement strategies make FEM a powerful and versatile tool for solving a wide range of engineering and physical problems. The detailed literature on FEM can be found in [44, 45, 46]. However, a brief overview of its working methodology is presented below

- Define the governing equations: Navier-Stokes etc.
- Weak formulation: Multiplying by test functions and integration by parts
- Discretize domain (mesh generation): Divide domain into elements, define nodes and connectivity
- Choose basis (shape/trial) functions: For velocity, pressure etc. usually chosen as polynomials
- Element-wise assembly: Loop over elements, use quadrature formula for integrals
- Impose boundary conditions: Dirichlet, Neumann etc.
- Solve global system: Direct or iterative solvers
- Post-processing: Visualize velocity, pressure etc.

3.1 Stokes Problem

The Stokes system of equations, as introduced in [47], is attributed to the Irish mathematician and physicist George Gabriel Stokes. This system represents a simplified form of the Navier-Stokes equations, obtained by neglecting the non-linear convective term. Such simplification is appropriate for modeling flows characterized by high viscosity or strong confinement. The governing equations of the Stokes system are given as

$$-\nabla^2 \mathbf{u} + \nabla p = \mathbf{f} \quad \text{in } \Omega, \tag{3.1.1a}$$

$$\nabla \cdot \mathbf{u} = 0 \quad \text{in } \Omega. \tag{3.1.1b}$$

Here, $\mathbf{u}$ denotes the velocity vector field, while p corresponds to the pressure scalar field. For simplicity, homogeneous Dirichlet boundary conditions $\mathbf{u} = 0$ on Γ are considered. Equation (3.1.1a) encapsulates the conservation of linear momentum and is commonly referred to as the momentum equation. In contrast, equation (3.1.1b) enforces mass conservation and represents the incompressibility condition.

The motivation for focusing on the finite element approximation of the Stokes equations stems from the particular difficulties associated with their discretization. These challenges are fundamentally tied to the structure of the Stokes problem itself and persist, when transitioning to the full Navier-Stokes formulation. Specifically, the absence of a pressure term in the continuity equation necessitates that the finite element spaces, selected for velocity and pressure fields, must be carefully constructed to ensure stability. Arbitrary combinations of discrete spaces typically lead to numerical instability unless they satisfy a specific compatibility criterion, commonly referred to as the inf-sup or Ladyzhenskaya-Babuška-Brezzi (LBB) condition [48].

This chapter aims to identify and analyze compatible finite element spaces suitable for stable discretization. The goal is to develop candidate numerical schemes applicable to the monolithic three-field multiphase flow formulation introduced in Chapter 4. As a foundational step, the next section will derive the weak formulation of the Stokes problem to facilitate the application of the finite element method.

3.2 Weak Formulation

To derive the weak formulation of the Stokes system (3.1.1), we proceed by multiplying the momentum equation (3.1.1a) with a suitable test function $\mathbf{v}$, and the incompressibility condition (3.1.1b) with a scalar test function q. Integrating both expressions over the spatial domain Ω, results as follows

$$\begin{aligned} \int_\Omega (-\nabla^2 \mathbf{u} + \nabla p) \cdot \mathbf{v}\, dx &= \int_\Omega \mathbf{f} \cdot \mathbf{v}\, dx, \\ \int_\Omega (\nabla \cdot \mathbf{u}) q\, dx &= 0, \end{aligned} \tag{3.2.1}$$

for all admissible test functions $\mathbf{v}$ and q defined over appropriate function spaces.

The fundamental motivation behind the variational formulation is to relax the continuity requirements on the weak solution ($\mathbf{u}$, p). This is achieved by integrating by parts and transferring derivatives to the test function ($\mathbf{v}$, q). The momentum equation in (3.2.1)

results as follows

$$\int_\Omega \nabla \mathbf{u} : \nabla \mathbf{v}\, dx - \int_\Omega \nabla \cdot (\nabla \mathbf{u} \cdot \mathbf{v})\, dx - \int_\Omega p \nabla \cdot \mathbf{v}\, dx + \int_\Omega \nabla \cdot (p\mathbf{v})\, dx = \int_\Omega \mathbf{f} \cdot \mathbf{v}\, dx, \quad (3.2.2)$$

where the notation $\nabla \mathbf{u} : \nabla \mathbf{v}$ denotes the component-wise inner product ($\nabla u_x \cdot \nabla v_x + \nabla u_y \cdot \nabla v_y$).

Applying the divergence theorem to the second and fourth terms of equation (3.2.2)

$$\int_\Omega \nabla \mathbf{u} : \nabla \mathbf{v}\, dx - \int_{\partial\Omega} (\mathbf{n} \cdot \nabla \mathbf{u}) \cdot \mathbf{v}\, ds - \int_\Omega p \nabla \cdot \mathbf{v}\, dx + \int_{\partial\Omega} p\mathbf{n} \cdot \mathbf{v}\, ds = \int_\Omega \mathbf{f} \cdot \mathbf{v}\, dx, \quad (3.2.3)$$

where $\mathbf{n}$ denotes the unit outward normal vector on the boundary $\partial\Omega$. Combining the boundary terms, the expression simplifies to

$$\int_\Omega \nabla \mathbf{u} : \nabla \mathbf{v}\, dx - \int_\Omega p \nabla \cdot \mathbf{v}\, dx - \int_{\partial\Omega} \left(\frac{\partial \mathbf{u}}{\partial \mathbf{n}} - p\mathbf{n} \right) \cdot \mathbf{v}\, ds = \int_\Omega \mathbf{f} \cdot \mathbf{v}\, dx, \quad (3.2.4)$$

where $\frac{\partial \mathbf{u}}{\partial \mathbf{n}}$ denotes the directional derivative of $\mathbf{u}$ in the normal direction.

For a well-posed weak formulation, it is standard to assume that the boundary integral term vanishes. This typically requires the test function $\mathbf{v}$ and the trial function $\mathbf{u}$ to vanish on the Dirichlet portion of the boundary, leading to the introduction of appropriate function spaces.

We begin by defining the Lebesgue and Sobolev spaces required for the velocity, pressure, and test functions. The square-integrable functions over Ω form the space $L^2(\Omega)$, which is defined as

$$L^2(\Omega) := \left\{ u : \Omega \to \mathbb{R} \;\middle|\; \int_\Omega |u(x)|^2 dx < \infty \right\}. \quad (3.2.5)$$

The Sobolev space of functions with square-integrable first derivatives is $\boldsymbol{H}^1(\Omega)$

$$\boldsymbol{H}^1(\Omega) := \left\{ \mathbf{u} \in L^2(\Omega) \;\middle|\; \frac{\partial \mathbf{u}}{\partial x_i} \in L^2(\Omega),\ i = 1, 2, \ldots, d \right\}. \quad (3.2.6)$$

The subspace of $\boldsymbol{H}^1(\Omega)$ with functions vanishing on the Dirichlet boundary $\partial\Omega_D$ is

$$\boldsymbol{H}_0^1(\Omega) := \left\{ \mathbf{v} \in \boldsymbol{H}^1(\Omega) \;\middle|\; \mathbf{v} = 0 \text{ on } \partial\Omega_D \right\}. \quad (3.2.7)$$

Since the pressure term appears without derivatives, it suffices for p and the scalar test function q to belong to $L^2(\Omega)$. Moreover, to ensure uniqueness of the pressure, we impose

a zero-mean condition, leading to the definition

$$L_0^2(\Omega) := \left\{ q \in L^2(\Omega) \;\middle|\; \int_\Omega q\,dx = 0 \right\}. \tag{3.2.8}$$

The variational formulation of the Stokes problem can now be stated as follows

Find $\mathbf{u} \in \boldsymbol{H}_0^1(\Omega)$ and $p \in L_0^2(\Omega)$ such that

$$\begin{aligned} \int_\Omega \nabla\mathbf{u} : \nabla\mathbf{v}\,dx - \int_\Omega p\nabla\cdot\mathbf{v}\,dx &= \int_\Omega \mathbf{f}\cdot\mathbf{v}\,dx \qquad \forall\, \mathbf{v} \in \boldsymbol{H}_0^1(\Omega), \\ \int_\Omega (\nabla\cdot\mathbf{u}) q\,dx &= 0 \qquad\qquad \forall\, q \in L_0^2(\Omega). \end{aligned} \tag{3.2.9}$$

Let the velocity and pressure spaces be defined as $\mathbb{V} := \boldsymbol{H}_0^1(\Omega) := \left(\boldsymbol{H}_0^1(\Omega)\right)^2$ and $\mathbb{Q} := L_0^2(\Omega)$, respectively. The corresponding dual spaces are denoted by $\mathbb{V}'$ and $\mathbb{Q}'$. The linear operators associated with the weak formulation of the Stokes system are introduced as follows.

The operator $\mathcal{L}_\mathbf{u} : \mathbb{V} \to \mathbb{V}'$ is defined via the duality pairing

$$\langle \mathcal{L}_\mathbf{u}\mathbf{u}, \mathbf{v}\rangle := \int_\Omega \nabla\mathbf{u} : \nabla\mathbf{v}\,dx \quad \forall\, \mathbf{u},\mathbf{v} \in \mathbb{V}. \tag{3.2.10}$$

To facilitate the extension within multiphase flow contexts (e.g., Navier-Stokes systems coupled with advection or phase-field equations), we introduce the notation

$$\mathcal{A}_\mathbf{u} := \mathcal{L}_\mathbf{u}, \tag{3.2.11}$$

allowing future augmentation of the momentum operator $\mathcal{A}_\mathbf{u}$ with additional physical contributions in later chapters.

The corresponding bilinear form $a_\mathbf{u} : \mathbb{V}\times\mathbb{V} \to \mathbb{R}$ is defined as

$$a_\mathbf{u}(\mathbf{u},\mathbf{v}) := \langle \mathcal{A}_\mathbf{u}\mathbf{u}, \mathbf{v}\rangle. \tag{3.2.12}$$

Here, $(\cdot,\cdot)$ denotes the inner product in $L^2(\Omega)^n$ $(n = 1,2)$, while $\langle\cdot,\cdot\rangle$ represents the duality pairing between $\mathbb{V}$ and $\mathbb{V}'$.

The divergence operator $\mathcal{B} : \mathbb{V} \to \mathbb{Q}'$ is defined through

$$\langle \mathcal{B}\mathbf{v}, q\rangle := -\int_\Omega (\nabla\cdot\mathbf{v})\, q\,dx \quad \forall\, \mathbf{v} \in \mathbb{V},\ q \in \mathbb{Q}, \tag{3.2.13}$$

and the corresponding bilinear form $b : \mathbb{V} \times \mathbb{Q} \to \mathbb{R}$ is given by

$$b(\mathbf{v}, q) := \langle \mathcal{B}\mathbf{v}, q \rangle . \tag{3.2.14}$$

The linear form $f : \mathbb{V} \to \mathbb{R}$ is defined as

$$f(\mathbf{v}) = \int_\Omega \mathbf{f} \cdot \mathbf{v}\, dx \quad \forall\, \mathbf{v} \in \mathbb{V}. \tag{3.2.15}$$

Thus, the weak formulation of the Stokes problem (3.1.1) reads

Find $(\mathbf{u}, p) \in \mathbb{V} \times \mathbb{Q}$ such that

$$\begin{cases} a(\mathbf{u}, \mathbf{v}) + b(\mathbf{v}, p) = f(\mathbf{v}) & \forall\, \mathbf{v} \in \mathbb{V}, \\ b(\mathbf{u}, q) = 0 & \forall\, q \in \mathbb{Q}. \end{cases} \tag{3.2.16}$$

The corresponding algebraic linear system takes the saddle-point form

$$\begin{bmatrix} \mathcal{A}_\mathbf{u} & \mathcal{B}^\mathrm{T} \\ \mathcal{B} & 0 \end{bmatrix} \begin{bmatrix} \mathbf{u} \\ p \end{bmatrix} = \begin{bmatrix} \mathrm{rhs}_\mathbf{u} \\ 0 \end{bmatrix}. \tag{3.2.17}$$

As discussed above, this chapter addresses the first major difficulty inherent to the incompressible Navier-Stokes equations: the coupling between velocity and pressure. A distinctive feature of this coupling is that the pressure does not appear explicitly in the continuity equation. This leads to a saddle-point problem [47, 48, 49, 50], and the algebraic system (3.2.17) exhibits the characteristic saddle-point structure.

According to the theory of mixed finite elements [49, 51, 52], the well-posedness of such problems is guaranteed by the Babuška-Brezzi theory, which is governed by the so-called inf-sup (or Ladyzhenskaya-Babuška-Brezzi, LBB) stability conditions.

The conditions required for the well-posedness of the continuous mixed formulation are

1. **Continuity of the bilinear form** $a(\cdot,\cdot)$

$$\exists\, M > 0 \quad \text{such that} \quad |a(\mathbf{u}, \mathbf{v})| \le M \|\mathbf{u}\|_\mathbb{V} \|\mathbf{v}\|_\mathbb{V} \quad \forall\, \mathbf{u}, \mathbf{v} \in \mathbb{V}.$$

2. **Coercivity on the kernel of** $b(\cdot,\cdot)$

$$\exists\, \alpha > 0 \quad \text{such that} \quad a(\mathbf{v}, \mathbf{v}) \ge \alpha \|\mathbf{v}\|_\mathbb{V}^2 \quad \forall\, \mathbf{v} \in \mathrm{Ker}\, b,$$

where the kernel is defined as

$$\text{Ker } b := \{\mathbf{v} \in \mathbb{V} \mid b(\mathbf{v}, q) = 0 \quad \forall\, q \in \mathbb{Q}\}.$$

3. **Inf-sup condition (LBB condition)**

$$\exists\, \beta > 0 \quad \text{such that} \quad \inf_{q \in \mathbb{Q}, q \neq 0} \sup_{\mathbf{v} \in \mathbb{V}, \mathbf{v} \neq 0} \frac{b(\mathbf{v}, q)}{\|\mathbf{v}\|_{\mathbb{V}} \, \|q\|_{\mathbb{Q}}} \geq \beta.$$

If all three conditions are satisfied, then the mixed problem of finding $(\mathbf{u}, p) \in \mathbb{V} \times \mathbb{Q}$ admits a unique solution that depends continuously on the given data (e.g. force term).

The next step is to formulate the discrete weak problem in order to approximate the solution using the finite element method (FEM).

3.3 Finite Element Approximation

To approximate the variational problem (3.2.16), we consider finite-dimensional subspaces $\mathbb{V}^h \subset \mathbb{V} := \left(\boldsymbol{H}_0^1(\Omega)\right)^d$, $d = 2$ and $\mathbb{Q}^h \subset \mathbb{Q} := L_0^2(\Omega)$, as introduced in the weak formulation section. Let the domain $\Omega \subset \mathbb{R}^d$ is partitioned by a grid $\mathcal{T}_h$ consisting of elements $K \in \mathcal{T}_h$, which are assumed to be quadrilaterals. For an element $K \in \mathcal{T}_h$, we denote by $\mathcal{E}(K)$ the set of all one-dimensional edges of K. Let $\mathcal{E}_i$ be the set of all interior element edges of the grid $\mathcal{T}_h$, such that $\mathcal{E}_i := \bigcup_{k \in \mathcal{T}_h} \{E \in \mathcal{E}(K) \mid E \cap \partial\Omega = \emptyset\}$.

The discrete formulation of the saddle-point problem (3.2.16) in the conforming subspaces $\mathbb{V}^h$ and $\mathbb{Q}^h$ is given by

Find $(\mathbf{u}_h, p_h) \in \mathbb{V}^h \times \mathbb{Q}^h$ such that

$$\begin{aligned} a(\mathbf{u}_h, \mathbf{v}_h) + b(\mathbf{v}_h, p_h) &= f(\mathbf{v}_h) \quad \forall\, \mathbf{v}_h \in \mathbb{V}^h, \\ b(\mathbf{u}_h, q_h) &= 0 \qquad \forall\, q_h \in \mathbb{Q}^h. \end{aligned} \tag{3.3.1}$$

To ensure well-posedness and convergence of the discrete problem, the pair $(\mathbb{V}^h, \mathbb{Q}^h)$ must satisfy the discrete Ladyzhenskaya-Babuška-Brezzi (LBB) condition

$$\inf_{q_h \in \mathbb{Q}^h q \neq 0} \sup_{\mathbf{v}_h \in \mathbb{V}^h \mathbf{v} \neq 0} \frac{b(\mathbf{v}_h, q_h)}{\|\mathbf{v}_h\|_{\mathbb{V}} \, \|q_h\|_{\mathbb{Q}}} \geq \beta_h > 0,$$

where β_h is a stability constant independent of the mesh size h. This condition is essential for guaranteeing stability of the numerical scheme; its failure can lead to spurious pressure

modes, even when the continuous problem is well-posed.

It is crucial to note that the satisfaction of the continuous inf-sup condition does not automatically imply that its discrete counterpart holds. Therefore, the choice of compatible finite element spaces is of paramount importance. Examples of stable pairs include the Q_2/P_1^{disc} [53, 54, 55, 56], Taylor-Hood [57, 58], and MINI [59] elements. Under the discrete LBB condition, the following a priori error estimate holds [49]

$$\|\mathbf{u}-\mathbf{u}_h\|_{\mathbb{V}}+\|p-p_h\|_{\mathbb{Q}} \leq C \inf_{\mathbf{v}\in\mathbb{V}^h, q\in\mathbb{Q}^h} \left(\|\mathbf{u}-\mathbf{v}\|_{\mathbb{V}}+\|p-q\|_{\mathbb{Q}}\right), \tag{3.3.2}$$

where $C>0$ is a constant independent of h.

The discrete functions $\mathbf{v}_h$ and q_h are piecewise polynomials, characterized by a finite number of degrees of freedom (DOF) determined through interpolation conditions. To preserve solvability of the discrete saddle-point system, the number of pressure DOF must not exceed that of the velocity field [60]

$$\dim \mathbb{Q}^h \leq \dim \mathbb{V}^h. \tag{3.3.3}$$

If this condition is violated, the system matrix is singular. At the same time, the pressure space must be sufficiently rich to ensure mass conservation through the discrete continuity equation.

The finite element spaces $\mathbb{V}^h$ and $\mathbb{Q}^h$ are typically spanned by locally supported basis functions, often referred to as shape functions. To compute the approximate solution of problem (3.3.1), we employ the following ansatz

$$\mathbf{u}_h = \sum_{i=1}^{NN_{\mathbf{u}}} \mathbf{u}_i v_i, \qquad p_h = \sum_{i=1}^{NN_p} p_i \chi_i, \tag{3.3.4}$$

where $\mathbf{u}_i$, p_i are the nodal values and v_i, χ_i are the basis functions for velocity and pressure. Moreover, $NN_{\mathbf{u}}$ and NN_p denote the degrees of freedom in the corresponding spaces. Using identical functions for trial and test spaces results in the standard Galerkin formulation, maintaining consistency with the weak form of the continuous problem. These basis functions (v_i, χ_i) are constructed from piecewise polynomials.

The Lagrange basis functions [61] satisfy the properties of the shape functions and are thus well-suited for conforming finite element discretizations of the Stokes problem, provided that the velocity and pressure spaces are appropriately paired. Their local support leads to sparse global matrices, which is advantageous for computational efficiency. In the following section, we construct basis functions based on piecewise polynomials for

various finite element types, including Q_1, Q_2, and P_1^{disc}.

3.4 Finite Element Choices

The widely adopted finite element pairs for incompressible flow problems are the Q_2/Q_1 element, commonly referred to as the Taylor-Hood element and the Q_2/P_1^{disc} element pair. The latter, although developed later, emerged from discussions during the Banff Conference on "Finite Elements in Flow Problems" in 1979 [53]. Both of these element combinations are stable in the sense that they satisfy the discrete inf-sup (LBB) condition as described in Section 3.3.

The Taylor-Hood element utilizes piecewise biquadratic polynomial approximations for the velocity field and bilinear approximations for the pressure field. In contrast, the Q_2/P_1^{disc} element pair employs a piecewise biquadratic approximation for velocity and a discontinuous piecewise linear approximation for pressure. Numerical investigations such as those presented in [62] indicate that the Q_2/P_1^{disc} element not only achieves higher accuracy but also exhibits superior convergence rates due to its higher-order structure.

The construction and properties of the elements Q_1, Q_2, and P_1^{disc} are examined in detail in the subsequent subsections. A general framework for constructing conforming finite element spaces can also be found in [63].

3.4.1 Bilinear Finite Element Q_1

In this subsection, we present the formulation of the bilinear Lagrange finite element, denoted by Q_1, on a quadrilateral element. The geometry of a typical Q_1 element is illustrated in Fig. 3.1, where the four degrees of freedom are located at four vertices of the quadrilateral.

To define the shape functions, we introduce a reference element $\Omega_{\text{ref}} = [-1,1]^2$, equipped with a local coordinate system (ξ,η) centered at the origin, as shown in Fig. 3.1 (right). This approach enables a unified formulation, avoiding the need to rederive shape functions for each element in the physical mesh, regardless of shape or size. The corresponding polynomial space associated with the Q_1 element consists of all bilinear polynomials, given by

$$\text{span}\{1,\xi,\eta,\xi\eta\}. \tag{3.4.1}$$

The shape functions on the reference element are constructed via the tensor product of one-dimensional linear Lagrange basis functions. These one-dimensional functions are

defined as [64]

$$\hat{\vartheta}_1(\xi) = \frac{1-\xi}{2}, \quad \hat{\vartheta}_2(\xi) = \frac{1+\xi}{2}, \quad -1 \leq \xi \leq 1. \tag{3.4.2}$$

The tensor product of these functions yields the bilinear Lagrange basis functions on Ω_{ref}

$$\begin{aligned} \hat{\chi}_1(\xi,\eta) &= \hat{\vartheta}_1(\xi)\hat{\vartheta}_1(\eta), \qquad \hat{\chi}_2(\xi,\eta) = \hat{\vartheta}_2(\xi)\hat{\vartheta}_1(\eta), \\ \hat{\chi}_3(\xi,\eta) &= \hat{\vartheta}_2(\xi)\hat{\vartheta}_2(\eta), \qquad \hat{\chi}_4(\xi,\eta) = \hat{\vartheta}_1(\xi)\hat{\vartheta}_2(\eta). \end{aligned} \tag{3.4.3}$$

Mapping shape functions from the reference element to a general quadrilateral in the physical domain is achieved via an isoparametric transformation. Specifically, the bilinear map $F_k : \Omega_{\text{ref}} \to \Omega_k$ transforms coordinates from the reference element to the physical element Ω_k as

$$\begin{bmatrix} x \\ y \end{bmatrix} = \mathcal{F}_k(\xi,\eta) = \sum_{i=1}^{4} \begin{bmatrix} x_i \\ y_i \end{bmatrix} \hat{\chi}_i(\xi,\eta), \tag{3.4.4}$$

where (x_i, y_i) are the coordinates of the i-th vertex of the physical quadrilateral element.

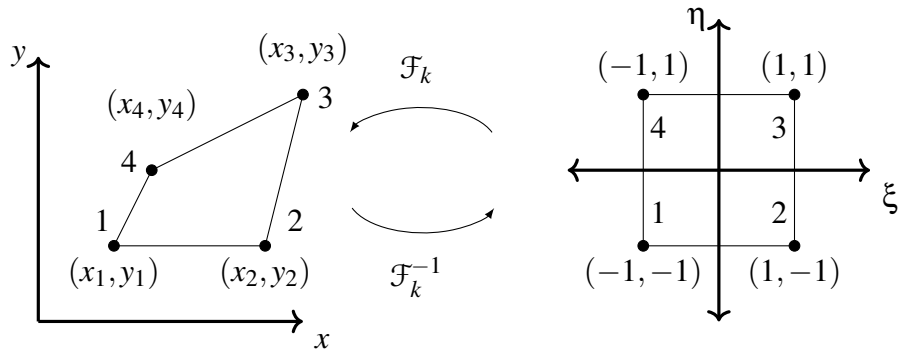

Figure 3.1: Mapping of a Q_1 quadrilateral between physical (left) and reference (right) element.

3.4.2 Biquadratic Finite Element Q_2

The Q_2 finite element, which employs biquadratic interpolation, possesses nine degrees of freedom. As depicted in Fig. 3.2, these are located at the four vertices, the midpoints of the four edges, and at the center of the quadrilateral element.

The corresponding polynomial space associated with the Q_2 element is given by

$$\text{span}\{1, \xi, \eta, \xi\eta, \xi^2, \eta^2\}, \tag{3.4.5}$$

where (ξ, η) denote the local coordinates defined on the reference element $\Omega_{\text{ref}} = [-1,1]^2$.

The shape functions for the Q_2 element are constructed via tensor products of one-dimensional quadratic Lagrange polynomials. These one-dimensional basis functions are defined as

$$\hat{\theta}_1(\xi) = \frac{1}{2}\xi(\xi-1), \quad \hat{\theta}_2(\xi) \quad = \frac{1}{2}\xi(\xi+1), \quad \hat{\theta}_3(\xi) = 1-\xi^2, \quad -1 \leq \xi \leq 1. \tag{3.4.6}$$

Using the tensor product of these basis functions, the biquadratic shape functions defined on the reference element are given by

$$\begin{aligned}
&\hat{\chi}_1(\xi,\eta) = \hat{\theta}_1(\xi)\hat{\theta}_1(\eta), \quad &&\hat{\chi}_2(\xi,\eta) = \hat{\theta}_2(\xi)\hat{\theta}_1(\eta), \quad &&\hat{\chi}_3(\xi,\eta) = \hat{\theta}_2(\xi)\hat{\theta}_2(\eta),\\
&\hat{\chi}_4(\xi,\eta) = \hat{\theta}_1(\xi)\hat{\theta}_2(\eta), \quad &&\hat{\chi}_5(\xi,\eta) = \hat{\theta}_3(\xi)\hat{\theta}_1(\eta), \quad &&\hat{\chi}_6(\xi,\eta) = \hat{\theta}_2(\xi)\hat{\theta}_3(\eta),\\
&\hat{\chi}_7(\xi,\eta) = \hat{\theta}_3(\xi)\hat{\theta}_2(\eta), \quad &&\hat{\chi}_8(\xi,\eta) = \hat{\theta}_1(\xi)\hat{\theta}_3(\eta), \quad &&\hat{\chi}_9(\xi,\eta) = \hat{\theta}_3(\xi)\hat{\theta}_3(\eta).
\end{aligned} \tag{3.4.7}$$

The transformation from the reference element to the corresponding physical element is realized via an isoparametric mapping. This mapping is defined using the biquadratic shape functions in equation (3.4.7), which are especially advantageous when approximating geometries with curved boundaries [41, 64], illustrated in Fig. 3.2.

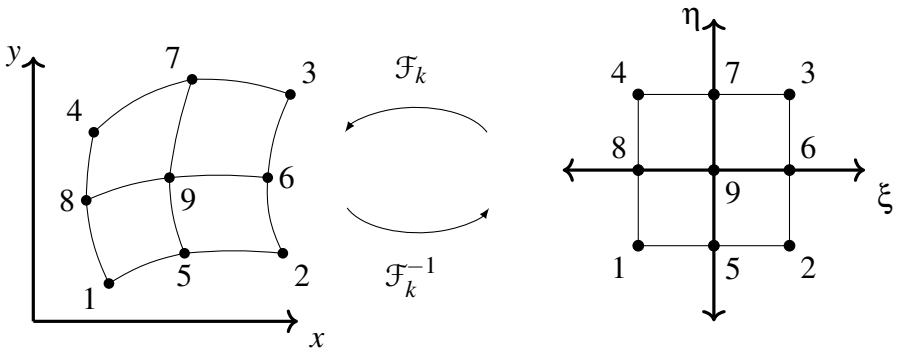

Figure 3.2: Biquadratic mapping between Q_2 physical (left) and reference (right) element.

3.4.3 Discontinuous Linear Element P_1^{disc}

The P_1^{disc} element is a discontinuous finite element that employs piecewise linear polynomials with three local degrees of freedom per element. The discontinuity across element interfaces is a defining characteristic of this element. The function space on a given physical element Ω_k can be described using two different approaches

- **Mapped Approach:** The shape functions are defined on the reference element and then mapped to the physical element via the inverse isoparametric transformation

$\mathcal{F}_k^{-1}$. The corresponding function space is given by

$$P_1^{\text{disc}}(\Omega_k) := \left\{ q \circ \mathcal{F}_k^{-1} \mid q \in \text{span}\{1, x, y\} \right\}. \tag{3.4.8}$$

- **Unmapped Approach:** The local coordinates are introduced directly on the physical element Ω_k, typically by connecting the midpoints of opposite edges. The basis functions are defined directly in physical coordinates

$$P_1^{\text{disc}}(\Omega_k) := \text{span}\{1, \xi, \eta\}. \tag{3.4.9}$$

In the mapped approach, the transformation can distort the approximation quality due to the lack of compatibility with the biquadratic mapping Q_2, which introduces non-linear effects. This mismatch leads to a degradation in the approximation order of the pressure field. Consequently, the unmapped approach is generally favored, as it preserves the second-order accuracy of the pressure approximation. Employing the conforming Q_2/P_1^{disc} finite element pair for the discretization of the Stokes equations ensures second-order accuracy in both velocity and pressure fields

$$\|\mathbf{u} - \mathbf{u}_h\|_0 = \mathcal{O}(h^3), \qquad \|p - p_h\|_0 = \mathcal{O}(h^2). \tag{3.4.10}$$

After selecting the Q_2/P_1^{disc} elements for the Stokes problem, the next steps of the FEM involve numerical integration of the discrete variational formulation using the Gauss-Legendre quadrature [65], which is well-suited for structured meshes and polynomial basis functions. The finite element matrices are then assembled, boundary conditions are imposed, and the resulting saddle-point system is solved using either direct or iterative solvers, as detailed in the next chapter.

The Q_2/P_1^{disc} finite element pair will also be employed in the monolithic three-field multiphase flow model that forms the core of the present research. Additional details on the finite element discretization of the material cut-off function (curvature free formulation) will be provided in the subsequent chapter.

4

Discretization and Numerical Solution of the Two-Phase Problem

As outlined in Chapter 1, numerical methods serve as essential tools for approximating the solutions of complex systems of equations, particularly in scenarios where analytical solutions are either exceedingly difficult or entirely unattainable. These computational techniques provide an alternative to experimental investigations, enabling the study of intricate physical phenomena through the simulation of corresponding mathematical models. The ability of numerical methods to deliver approximate yet accurate solutions makes them indispensable in the analysis of non-linear, time-dependent, and multi-scale problems commonly encountered in scientific and engineering disciplines.

The foundational framework for the numerical treatment of the current system of equations (2.6.3) has been established through the finite element discretization of the Stokes system, presented in the Chapter 3. Building on this foundation, the present chapter provides a comprehensive discussion of the numerical methods employed to solve the final formulation (2.6.3), including the justification for their selection and their integration into the overall computational framework.

Since the underlying formulation is time-dependent, the first step is the discretization of the temporal domain. Accordingly, the following section focuses on time discretization techniques.

4.1 Time Discretization

Time discretization plays a crucial role in obtaining accurate and stable numerical solutions of the unsteady Navier-Stokes equations. The choice of an appropriate time-stepping scheme directly influences the stability and accuracy of the computed solution. An unsuitable scheme may introduce significant numerical artifacts, such as spurious oscillations or non-physical mass loss in transport-dominated phenomena.

Time integration methods are generally categorized into explicit and implicit schemes. While explicit schemes are straightforward to implement, they are conditionally stable and subject to stringent time step restrictions governed by the Courant-Friedrichs-Lewy (CFL) condition [66]. This stability constraint significantly limits its efficiency for long time flow simulations.

To overcome these limitations, we employ implicit time integration methods, specifically the Backward Euler and Crank-Nicolson schemes [67]. These methods are unconditionally stable and thus allow larger time steps. The Backward Euler method is first-order accurate in time and exhibits strong A-stability, making it suitable for stiff problems. In contrast, the Crank-Nicolson method is second-order accurate and also A-stable, offering a good balance between accuracy and stability.

Therefore, we will discretize the system of equations (2.6.3) in time with a fully implicit time stepping scheme (Backward Euler/Crank-Nicolson). Let $\mathbf{u}^n$ be the velocity at a given time t^n, compute $\mathbf{u}^{n+1}$, p^{n+1}, and ψ^{n+1} at time t^{n+1} with time step $\Delta t = t^{n+1} - t^n$. The momentum equation is discretized as

$$\begin{aligned}\Big[\alpha\rho(\psi^{n+1})\mathbf{I} + \theta\Big(\rho(\psi^{n+1})\mathbf{u}^{n+1}\cdot\nabla - 2\mu(\psi^{n+1})\nabla\cdot\mathbf{D}\Big)\Big]\mathbf{u}^{n+1} + \theta\Big(\nabla\cdot\boldsymbol{\tau}_m(\psi^{n+1})\Big) + \nabla p^{n+1} = \\ \Big[\alpha\rho(\psi^{n})\mathbf{I} - (1-\theta)\Big(\rho(\psi^{n})\mathbf{u}^{n}\cdot\nabla - 2\mu(\psi^{n})\nabla\cdot\mathbf{D}\Big)\Big]\mathbf{u}^{n} - (1-\theta)\Big(\nabla\cdot\boldsymbol{\tau}_m(\psi^{n})\Big),\end{aligned} \tag{4.1.1a}$$

and the material cut-off function equation is discretized as

$$\begin{aligned}\Big[\alpha\mathbf{I} + \theta\mathbf{u}^{n+1}\cdot\nabla\Big]\psi^{n+1} - \theta\gamma_1\nabla\cdot\mathcal{F}(\psi^{n+1}) - \theta\gamma_2\nabla\cdot\mathcal{G}(\psi^{n+1}) = \\ \Big[\alpha\mathbf{I} - (1-\theta)\mathbf{u}^{n}\cdot\nabla\Big]\psi^{n} - (1-\theta)\gamma_1\nabla\cdot\mathcal{F}(\psi^{n}) - (1-\theta)\gamma_2\nabla\cdot\mathcal{G}(\psi^{n}),\end{aligned} \tag{4.1.1b}$$

where $\alpha = \frac{1}{\Delta t}$ denotes the inverse time step and θ is a switching parameter which is set to 1 for Backward Euler and $\frac{1}{2}$ for Crank-Nicolson. Moreover, the compression and the diffusion in normal direction for the material cut-off function are denoted by $\mathcal{F}(\psi)$ and

$\mathcal{G}(\psi)$, respectively.

$$\begin{aligned}\mathcal{F}(\psi) =& (0.5+\psi)(0.5-\psi)\frac{\nabla\psi}{\|\nabla\psi\|},\\ \mathcal{G}(\psi) =& -\left(\nabla\psi\cdot\frac{\nabla\psi}{\|\nabla\psi\|}\right)\frac{\nabla\psi}{\|\nabla\psi\|}.\end{aligned} \tag{4.1.2}$$

Following the time discretization of the system of equations (2.6.3), the next step involves spatial discretization, described in detail in the following section.

4.2 Space Discretization

The finite element approximation of the system is based on its weak formulation, which is derived as the initial step of the spatial discretization process.

4.2.1 Weak Formulation

For solving the system of equations (2.6.3) the variational formulations are prepared and spaces (the Lebesgue and the Sobolev) are defined. As the choice of finite element spaces for the velocity and pressure fields has already been discussed in Chapter 3, it remains to specify an appropriate function space for the material cut-off function ψ.

In equation (4.1.2), both $\mathcal{F}(\psi)$ and $\mathcal{G}(\psi)$ explicitly involve the gradient $\nabla\psi$, and include non-linear expressions with normalized gradients such as

$$\frac{\nabla\psi}{\|\nabla\psi\|}.$$

Such terms require that $\psi \in H^1(\Omega)$, since the weak gradient must exist almost everywhere and be square-integrable i.e.

$$\nabla\psi \in [L^2(\Omega)]^2.$$

Let $\mathbb{V}$, $\mathbb{Q}$, and $\mathbb{M}$ denote the spaces for the velocity, pressure, and material cut-off function, respectively, and $\mathbb{V}'$, $\mathbb{Q}'$, and $\mathbb{M}'$ be their corresponding dual spaces. Furthermore, we set $\mathbb{Y} := \mathbb{V}\times\mathbb{M}$ and $\mathbb{Y}' := \mathbb{V}'\times\mathbb{M}'$. The following linear forms (for the momentum equation) are introduced as $\mathcal{A}_{\mathbf{u}}$, $\mathcal{M}_{\mathbf{u}}$, $\mathcal{N}_{\mathbf{u}}$, and $\mathcal{L}_{\mathbf{u}}$ defined on $\mathbb{V}\longrightarrow\mathbb{V}'$

$$\begin{aligned}
\langle \mathcal{M}_{\mathbf{u}}\mathbf{u},\mathbf{v}\rangle &= \int_\Omega \rho(\psi)\mathbf{u}\mathbf{v}\,dx && \forall\,\mathbf{u},\mathbf{v}\in\mathbb{V},\\
\langle \mathcal{N}_{\mathbf{u}}\mathbf{u},\mathbf{v}\rangle &= \int_\Omega \rho(\psi)(\mathbf{u}\cdot\nabla\mathbf{u})\mathbf{v}\,dx && \forall\,\mathbf{u},\mathbf{v}\in\mathbb{V},\\
\langle \mathcal{L}_{\mathbf{u}}\mathbf{u},\mathbf{v}\rangle &= \int_\Omega 2\mu(\psi)\mathbf{D}(\mathbf{u}):\mathbf{D}(\mathbf{v})\,dx && \forall\,\mathbf{u},\mathbf{v}\in\mathbb{V},
\end{aligned} \tag{4.2.1}$$

and we set $\mathcal{A}_{\mathbf{u}}$ in the extended definition, initially defined in Chapter 3, equation (3.2.11).

$$\mathcal{A}_{\mathbf{u}} := \alpha\mathcal{M}_{\mathbf{u}} + \theta\mathcal{N}_{\mathbf{u}}(\mathbf{u}) + \theta\mathcal{L}_{\mathbf{u}}. \tag{4.2.2}$$

In the similar manner, the linear forms (for the material cut-off equation): $\mathcal{A}_\psi$, $\mathcal{M}_\psi$, $\mathcal{N}_\psi$, and $\mathcal{L}_\psi$, defined on $\mathbb{M}\longrightarrow\mathbb{M}'$ are as follows

$$\begin{aligned}
\langle \mathcal{M}_\psi\psi,\xi\rangle &= \int_\Omega \psi\xi\,dx && \forall\,\psi,\xi\in\mathbb{M},\\
\langle \mathcal{N}_\psi(\mathbf{u})\psi,\xi\rangle &= \int_\Omega \mathbf{u}\cdot\nabla\psi\xi\,dx && \forall\,\psi,\xi\in\mathbb{M},\\
\langle \mathcal{N}_\psi(\nabla\psi)\psi,\xi\rangle &= \int_\Omega \mathcal{F}(\psi)\nabla\xi\,dx && \forall\,\psi,\xi\in\mathbb{M},\\
\langle \mathcal{L}_\psi(\nabla\psi)\psi,\xi\rangle &= \int_\Omega \mathcal{G}(\psi)\nabla\xi\,dx && \forall\,\psi,\xi\in\mathbb{M},
\end{aligned} \tag{4.2.3}$$

the collective linear forms are

$$\begin{aligned}
\mathcal{A}_\psi &:= \alpha\mathcal{M}_\psi + \theta\gamma_1\mathcal{N}_\psi(\nabla\psi) + \theta\gamma_2\mathcal{L}_\psi(\nabla\psi),\\
\mathcal{C}_{\mathbf{u}}^{\mathrm{T}} &= \theta\mathcal{N}_\psi(\mathbf{u}).
\end{aligned} \tag{4.2.4}$$

Furthermore, the following linear forms: $\mathcal{B}$ and $\mathcal{C}$ defined on $\mathbb{V}\longrightarrow\mathbb{Q}'$ and $\mathbb{M}\longrightarrow\mathbb{V}'$ are as follows

$$\begin{aligned}
\langle \mathcal{B}\mathbf{u},q\rangle &= -\int_\Omega \nabla\cdot\mathbf{u}\,q\,dx && \forall\,\mathbf{u}\in\mathbb{V},q\in\mathbb{Q},\\
\langle \mathcal{C}\psi,\mathbf{v}\rangle &= \int_\Omega \tau_m(\psi):\nabla\mathbf{v}\,dx && \forall\,\psi\in\mathbb{M},\mathbf{v}\in\mathbb{V}.
\end{aligned} \tag{4.2.5}$$

In the next step, the bilinear forms $a(\cdot,\cdot)$ defined on $\mathbb{Y}\times\mathbb{Y}\longrightarrow\mathbb{R}$ and $b(\cdot,\cdot)$ defined on $\mathbb{Y}\times\mathbb{Q}\longrightarrow\mathbb{R}$ read
For $\mathcal{U}=(\mathbf{u},\psi)$ and $\mathcal{V}=(\mathbf{v},\xi)$

$$\begin{aligned}
a(\mathcal{U},\mathcal{V}) &= \langle \mathcal{A}_{\mathbf{u}}\mathbf{u},\mathbf{v}\rangle + \langle \mathcal{A}_\psi\psi,\xi\rangle + \langle \mathcal{C}\psi,\mathbf{v}\rangle,\\
b(\mathcal{U},q) &= b(\mathbf{u},q).
\end{aligned} \tag{4.2.6}$$

The compact weak formulation for the curvature free material cut-off function (2.6.3) reads

Find $(\mathcal{U}, p) \in \mathbb{Y} \times \mathbb{Q}$ such that:

$$\begin{cases} a(\mathcal{U}, \mathcal{V}) + b(\mathcal{V}, p) = 0 & \forall\, \mathcal{V} \in \mathbb{Y}, \\ b(\mathcal{U}, q) = 0 & \forall\, q \in \mathbb{Q}. \end{cases} \tag{4.2.7}$$

4.2.2 Conservation

The mass conservation of the function ψ is a crucial property. The preservation of the area enclosed by $\psi = 0$ can be demonstrated by analyzing a single iteration of the Crank-Nicolson or Backward Euler method for time discretization [68].

As aforementioned, the test function $\xi \in \boldsymbol{H}^1$ is a piecewise linear function analogous to ψ. Consequently, the gradient of the test function vanishes i.e. $\nabla\xi = 0$ (particularly holds for $\xi \equiv 1$).

$$\int_\Omega \frac{\partial \psi}{\partial t}\xi\, dx + \underbrace{\int_\Omega \nabla\xi \cdot (\mathbf{u}\psi)\, dx}_{0} + \underbrace{\int_\Omega \mathcal{F}(\psi)\nabla\xi\, dx}_{0} + \underbrace{\int_\Omega \mathcal{G}(\psi)\nabla\xi\, dx}_{0}. \tag{4.2.8}$$

The equation takes the following form

$$\int_\Omega \frac{\psi^{n+1} - \psi^n}{\Delta t} dx = 0, \tag{4.2.9}$$

simplifying

$$\int_\Omega \psi^{n+1} dx = \int_\Omega \psi^n dx. \tag{4.2.10}$$

Thus, mass is conserved exactly.

4.2.3 Finite Element Discretization

For the space discretization of the problem, the domain $\Omega \subset \mathbb{R}^d$ is partitioned by a grid $\mathcal{T}_h$ consisting of elements $K \in \mathcal{T}_h$, which are assumed to be quadrilaterals. For an element $K \in \mathcal{T}_h$, we denote by $\mathcal{E}(K)$ the set of all one-dimensional edges of K. Let $\mathcal{E}_i$ be the set of all interior element edges of the grid $\mathcal{T}_h$, such that $\mathcal{E}_i := \bigcup_{k\in\mathcal{T}_h}\{E \in \mathcal{E}(K) \mid E \cap \partial\Omega = \emptyset\}$.

For the approximation of the problems (4.2.7) with the finite element method, the approximation spaces are introduced as $\mathbb{V}^h$, $\mathbb{M}^h$, and $\mathbb{Q}^h$ and the product spaces are defined as

$\mathbb{Y}^h := \mathbb{V}^h \times \mathbb{M}^h$.

$$\begin{aligned} \mathbb{V}^h &= \left\{ \mathbf{v}_h \in \mathbb{V}, \mathbf{v}_{h|K} \in (Q_2(K))^2 \right\}, \\ \mathbb{M}^h &= \left\{ \xi_h \in \mathbb{M}, \xi_{h|K} \in Q_2(K) \right\}, \\ \mathbb{Q}^h &= \left\{ q_h \in \mathbb{Q}, q_{h|K} \in P_1^{\text{disc}}(K) \right\}. \end{aligned} \tag{4.2.11}$$

The velocity and pressure fields are discretized using the higher order stable Q_2/P_1^{disc} finite element pair [69]. The material cut-off function ψ involves gradient terms in its weak formulation, which necessitates its approximation in a conforming $\boldsymbol{H}^1(\Omega)$ space to ensure inter-element continuity. For this reason, discontinuous or purely L^2-based finite elements are unsuitable. Among the available C^0-continuous elements, the quadratic element Q_2 is selected in the present work, as shown in Fig. 4.1. Compared to the linear Q_1 element, Q_2 offers improved accuracy, which is particularly beneficial for resolving interface dynamics associated with multiphase flow problems [28]. The effectiveness of this choice is further supported by the numerical results presented in Chapter 5, specifically in Table 5.2, demonstrating the accuracy and stability. Hence, the problem (4.2.7) to the weak formulation, discretized in time and space reads

Find $(\mathcal{U}_h, p_h) \in \mathbb{Y}^h \times \mathbb{Q}^h$ such that

$$\begin{cases} a(\mathcal{U}_h, \mathcal{V}_h) + b(\mathcal{V}_h, p_h) = 0 & \forall\, \mathcal{V}_h \in \mathbb{Y}^h, \\ b(\mathcal{U}_h, q_h) = 0 & \forall\, q_h \in \mathbb{Q}^h. \end{cases} \tag{4.2.12}$$

As discussed in Chapter 3, the chosen finite element spaces $\mathbb{V}^h$ and $\mathbb{Q}^h$ satisfy the inf-sup stability condition [52], ensuring the well-posedness of the velocity-pressure pair. Regarding the third space $\mathbb{M}^h$, it is important to note that the associated variable ψ represents a material cut-off function, not a non-Newtonian stress tensor. Consequently, the second inf-sup condition, which is typically required in mixed formulations involving additional stress-like fields [25, 70], is not applicable in this context.

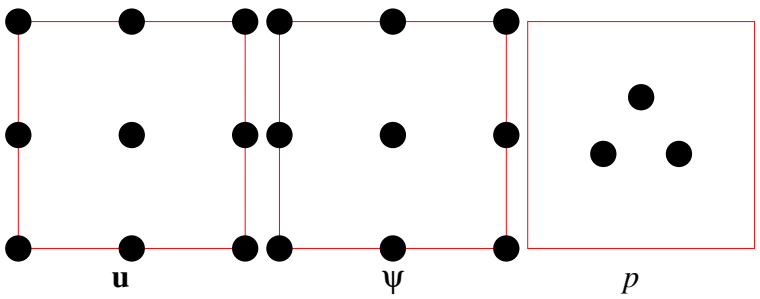

Figure 4.1: Higher order finite element Q_2, Q_2, and P_1^{disc} on quadrilaterals.

Thus, the corresponding final non-linear discrete curvature free material cut-off system

reads

$$\begin{bmatrix} \mathcal{A}_{\mathbf{u}} & \mathcal{C}_{\psi} & \mathcal{B}^{\mathrm{T}} \\ \mathcal{C}_{\mathbf{u}}^{\mathrm{T}} & \mathcal{A}_{\psi} & 0 \\ \mathcal{B} & 0 & 0 \end{bmatrix} \begin{bmatrix} \mathbf{u}^{n+1} \\ \psi^{n+1} \\ p^{n+1} \end{bmatrix} = \begin{bmatrix} rhs_{\mathbf{u}} \\ rhs_{\psi} \\ 0 \end{bmatrix}, \tag{4.2.13}$$

where

$$\begin{aligned} \mathcal{A}_{\mathbf{u}} &= \alpha\mathcal{M}_{\mathbf{u}} + \theta\mathcal{L}_{\mathbf{u}} + \theta\mathcal{N}_{\mathbf{u}}(\mathbf{u}), \\ \mathcal{A}_{\psi} &= \alpha\mathcal{M}_{\psi} + \theta\gamma_1\mathcal{N}_{\psi}(\nabla\psi) + \theta\gamma_2\mathcal{L}_{\psi}(\nabla\psi), \\ \mathcal{C}_{\mathbf{u}}^{T} &= \theta\mathcal{N}_{\psi}(\mathbf{u}), \end{aligned} \tag{4.2.14}$$

where $\mathcal{M}_{\mathbf{u}}$ and $\mathcal{M}_{\psi}$ are the mass matrix operators and $\mathcal{L}_{\mathbf{u}}$ is the discrete diffusion. The non-linear discrete normal diffusion for the material cut-off function is designed by $\mathcal{L}_{\psi}(\nabla\psi)$. Moreover, $\mathcal{N}_{\mathbf{u}}(\mathbf{u})$, $\mathcal{N}_{\psi}(\mathbf{u})$, and $\mathcal{N}_{\psi}$ are the discrete non-linear transport operators w.r.t. $\mathbf{u}$ and $\nabla\psi$. Furthermore, $\mathcal{B}$ is the vectorial discrete divergence operator. The operator $\mathcal{C}$ is the tensorial discrete divergence operator of multiphase tensor τ_m i.e. $\mathcal{C}\xi := \nabla \cdot \tau_m(\xi)$. The details about the matrix (4.2.13) blocks are given below.

Blocks Interpretation

- $\mathcal{A}_{\mathbf{u}}$: Momentum block depending on the material cut-off function ψ. It includes contributions from mass (inertia), convection, variable density, and viscosity. Non-linearity is due to convection as well as the dependency on $\rho(\psi)$ and $\mu(\psi)$.

- $\mathcal{C}_{\psi}$: Coupling of ψ into the momentum equation via variable properties (density, viscosity) and capillary stresses.

- $\mathcal{B}$, $\mathcal{B}^T$: Discrete divergence and gradient operators enforcing incompressibility ($\nabla \cdot \mathbf{u} = 0$). This forms the classic saddle-point structure of incompressible flows.

- $\mathcal{C}_{\mathbf{u}}^T$: Coupling of $\mathbf{u}$ into the material cut-off function equation. It represents advection of ψ by the velocity field.

- $\mathcal{A}_{\psi}$: Non-linear material cut-off function operator including time derivative, advection, and regularization terms. Strongly non-linear due to the sharpening terms.

A critical consideration in the discrete treatment of interfacial flow problems is the accurate evaluation of phase-dependent quantities (density, viscosity etc.), briefly discussed in the subsequent section.

4.3 Treatment of Material Properties Jump

Accurate evaluation of the discontinuous material properties such as pressure p, density ρ, viscosity μ, and the level set ϕ or material cut-off function ψ is a critical and delicate task in two-phase flow simulations. Several approaches [71, 72] exist to handle these discontinuities across the interface. A widely used method involves interface smearing via interpolation with a smoothed Heaviside function $\mathcal{H}_\psi$ [72], allowing continuous transitions between phases and reducing numerical artifacts. Polynomial orders within $\mathcal{H}_\psi$ can be chosen to control interpolation accuracy and convergence behavior.

An alternative is the patching method or area-weighted averaging, which computes material properties based on the geometric intersection of the interface with the mesh. In this approach, element Q_2 is first classified by evaluating ψ at its degrees of freedom (DOF).

- Elements fully within a phase $\psi < 0$ for Ω_1 or $\psi > 0$ for Ω_2, are assigned by the corresponding material property directly (e.g. ρ_1 or ρ_2)
- For cut elements, where $\psi = 0$ intersects the domain, the element is subdivided (e.g. into 8 sub-triangles) to resolve the local interface geometry (see Fig. 4.2). Local areas (triangles shaded with grey lines in Fig. 4.2) corresponding to each phase are then computed and properties (such as density) are averaged accordingly:

$$\rho_K = \frac{(area_1 \times \rho_1) + (area_2 \times \rho_2)}{\text{area of the element}} \tag{4.3.1}$$

This area-weighted interpolation captures sub-element phase fractions and is shown to offer improved accuracy over smearing methods, especially as mesh resolution increases [72].

4.4 Non-linear and Linear Solver

The system of equations (4.2.13) exhibits non-linearity primarily due to the convective terms present in the momentum equation. In addition, the compressive flux term contributes further to the non-linearity of the system because of its dependency on solution gradients. Addressing such non-linearities poses significant challenges for numerical solvers. Typically, iterative methods such as Newton's method or fixed-point iterations are employed to handle non-linear systems in fluid dynamics [73]. Among these, Newton's method is generally preferred due to its superior convergence properties, particularly its quadratic convergence near the solution under suitable conditions. Which is a strong

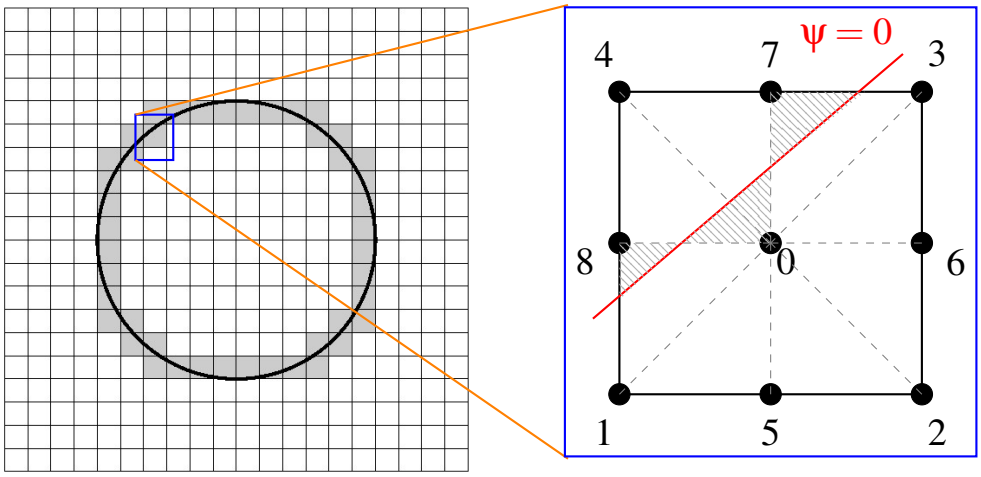

Figure 4.2: Distribution of the discontinuous material properties (viscosity and density) within a Q_2 finite element. Elements intersected by the interface are shaded in gray (shown on the left-side in the full view). Each such element is subdivided into triangles (in dotted lines shown on the right-side in the zoomed view).

advantage over the linear convergence of the fixed-point method.

4.4.1 Newton Method

This section details with the linearization strategy employed in the Newton method for solving non-linear systems. Let $\mathcal{R}(\mathcal{U}) \in C^1$ denote a continuously differentiable residual operator, where $\mathcal{U} = (\mathbf{u}, \psi, p)$ is the solution vector representing the velocity, material cut-off function, and pressure, respectively. Provided that the derivative $\mathcal{R}'(\mathcal{U})$ is non-singular, the classical Newton iteration scheme can be expressed as

$$\mathcal{U}^{l+1} = \mathcal{U}^l - \left[\mathcal{R}'(\mathcal{U}^l)\right]^{-1} \mathcal{R}(\mathcal{U}^l), \quad \forall\, l \geq 0, \tag{4.4.1}$$

which aims to compute a root of the non-linear equation by iteratively updating the solution vector. The update step involves solving a linearized system of the form

$$J(\mathcal{U}^l)\delta\mathcal{U}^l = \mathcal{R}(\mathcal{U}^l),$$

where $J(\mathcal{U}^l) = \frac{\partial \mathcal{R}(\mathcal{U}^l)}{\partial \mathcal{U}^l}$ is the Jacobian matrix and $\delta\mathcal{U}^l$ is the Newton correction term at iteration l.

The method requires a suitable initial guess $\mathcal{U}^0$ at the zeroth iteration. It is important to note that Newton's method exhibits quadratic convergence in the neighborhood of the

solution, provided that the Jacobian is well-conditioned and the initial guess is sufficiently close to the actual solution. In the context of the present work, Newton's method is applied to solve the unsteady, non-linear system of equations (4.2.13), following the procedural steps outlined in algorithm 4.1.

Algorithm 4.1 Newton method

- Provide the input parameters, e.g. tolerance, parameters of the non-linear solver, initial guess and the iteration number l
- Repeat until the tolerance is achieved
- Calculate the residual $\mathcal{R}(\mathcal{U}^l) = \mathbf{A}\,\mathcal{U}^l - \mathbf{b}$
- Build the Jacobian $J(\mathcal{U}^l) = \frac{\partial \mathcal{R}(\mathcal{U}^l)}{\partial \mathcal{U}^l}$
- Solve $J(\mathcal{U}^l)\,\delta\mathcal{U}^l = \mathcal{R}(\mathcal{U}^l)$
- Find the optimal value of the damping factor $\omega^l \in (-1, 0]$
- Approximate $\mathcal{U}^{l+1} = \mathcal{U}^l - \omega^l\,\delta\mathcal{U}^l$

For non-linear systems arising in multiphase flow problems, Newton's method is an effective iterative approach, but its numerical stability depends on several other critical factors (in addition to the initial guess). One such factor is the damping parameter ω, which is particularly important in the presence of non-smooth or stiff solution behavior. In this study, the damping factor is adaptively determined through a line search algorithm, a root-finding strategy designed to enhance convergence and stability [74, 75, 76]. For the current non-linear coupled system, each Newton step can be formally written as

$$\begin{bmatrix} \mathbf{u}^{l+1} \\ \psi^{l+1} \\ p^{l+1} \end{bmatrix} = \begin{bmatrix} \mathbf{u}^{l} \\ \psi^{l} \\ p^{l} \end{bmatrix} - \omega_l \begin{bmatrix} \frac{\partial \mathcal{R}_{\mathbf{u}}(\mathcal{U}^l)}{\partial \mathbf{u}} & \frac{\partial \mathcal{R}_{\mathbf{u}}(\mathcal{U}^l)}{\partial \psi} & \frac{\partial \mathcal{R}_{\mathbf{u}}(\mathcal{U}^l)}{\partial p} \\ \frac{\partial \mathcal{R}_{\psi}(\mathcal{U}^l)}{\partial \mathbf{u}} & \frac{\partial \mathcal{R}_{\psi}(\mathcal{U}^l)}{\partial \psi} & \frac{\partial \mathcal{R}_{\psi}(\mathcal{U}^l)}{\partial p} \\ \frac{\partial \mathcal{R}_{p}(\mathcal{U}^l)}{\partial \mathbf{u}} & \frac{\partial \mathcal{R}_{p}(\mathcal{U}^l)}{\partial \psi} & \frac{\partial \mathcal{R}_{p}(\mathcal{U}^l)}{\partial p} \end{bmatrix}^{-1} \begin{bmatrix} \mathcal{R}_{\mathbf{u}}(\mathcal{U}^l) \\ \mathcal{R}_{\psi}(\mathcal{U}^l) \\ \mathcal{R}_{p}(\mathcal{U}^l) \end{bmatrix}, \tag{4.4.2}$$

where the full Jacobian matrix $J(\mathcal{U})$, composed of the first derivatives of the residual functions $\mathcal{R}_{\mathbf{u}}$, $\mathcal{R}_{\psi}$ and $\mathcal{R}_p$ is required at each iteration to construct the linearized update system.

Depending on the problem structure, the Jacobian matrix may be obtained analytically or approximated using numerical techniques. A common and flexible approach is the finite difference (divided difference) approximation, which enables a black-box treatment of the

residual operator without requiring explicit derivation of derivatives [77, 78].
In the present work, we opt for the numerical approximation of the Jacobian. Specifically, the j^{th} column of the Jacobian at iteration n is estimated using a central difference scheme as follows

$$\left[\frac{\partial \mathcal{R}(\mathcal{U}^l)}{\partial \mathcal{U}^l}\right]_j \approx \frac{\mathcal{R}(\mathcal{U}^l + \chi\delta_j) - \mathcal{R}(\mathcal{U}^l - \chi\delta_j)}{2\chi}, \tag{4.4.3}$$

where δ_j is the unit basis vector in the j^{th} coordinate direction, and $\chi > 0$ is a perturbation parameter. The key advantage of this strategy is that it eliminates the need for analytical Jacobian expressions, which is especially beneficial for complex or highly non-linear systems. However, the accuracy and stability of this approximation are sensitive towards the choice of χ. Selecting an appropriate step size remains a subtle issue: χ may be chosen as a constant or adjusted adaptively based on residual behavior and sensitivity analysis [79, 80].

4.4.2 Linear System

After applying the Newton linearization to the non-linear system, the next critical step involves solving the resulting linear subproblem. This linear system, expressed as $J(\mathcal{U})\ \delta\mathcal{U} = \mathcal{R}(\mathcal{U})$, must be solved at each iteration, where $J(\mathcal{U})$ is the Jacobian matrix and $\mathcal{U} = \{\mathbf{u}, \psi, p\}$ represents the vector of unknowns. Solving this linear system often constitutes the most computationally intensive part of the algorithm.

Linear solvers are generally categorized into two main types: direct and iterative methods. The choice between these depends on the problem size, matrix structure, and available computational resources.

If sufficient memory is available, direct solvers are preferred due to their robustness and predictability. Methods such as Gaussian elimination and LU decomposition [81, 82] compute the solution in a finite number of steps. For sparse systems, the Unsymmetric MultiFrontal Method (UMFPACK) [83, 84] is widely used and offers an efficient implementation for solving large sparse linear systems. Given the matrix $J(\mathcal{U})$ and right-hand side $\mathcal{R}(\mathcal{U})$, these solvers yield the solution vector $\delta\mathcal{U}$ containing all unknown fields in a single computational step.

However, for very large systems, direct solvers can be infeasible due to high memory requirements and computational cost. In such cases, iterative solvers are a more suitable alternative e.g. BiCG, GMRES, Multigrid etc. The choice depends on a trade-off between memory capacity, problem size, matrix structure, numerical robustness, and time to solution.

Multigrid methods [85, 86, 87] offer an efficient solution strategy for large linear systems by combining smoothing, restriction, prolongation, and a direct coarse-grid solver (e.g. UMFPACK). This approach leverages a hierarchy of discretization levels, transferring residuals between grids via restriction (fine to coarse) and prolongation (coarse to fine), with Vanka-type smoothers [88, 89] applied pre- and post-transfer. The choice of cycle type (e.g. V, F, or W-cycle) determines how frequently coarse levels are visited. The coarsest level is solved directly and should remain sufficiently coarse to minimize memory usage.

4.5 Flow around a Cylinder

Prior to applying our monolithic three-field multiphase flow solver to interfacial flow problems, we validate the monolithic standard Navier-Stokes solver using the well-established "flow around a cylinder" benchmark [90]. With regard to the multiphase flow benchmarks and accompanying numerical studies, we have chosen to present them in detail in the following Chapter 5. This decision is motivated by the extensive set of results, validations, and test cases that warrant a dedicated and comprehensive discussion.

This two-dimensional DFG benchmark [90] analyses the attributes of the flow around an obstacle in a rectangular channel, where a cylinder of radius $r = 0.05$ is placed with the center at $(0.2, 0.2)$ in a rectangular channel of length 2.2, the upper and lower walls are 0.41 length apart. The geometrical configuration and coarse mesh are shown in Fig. 4.3 and 4.4. The fluid density ρ and kinematic viscosity η are set to 1 and 0.001, respectively.

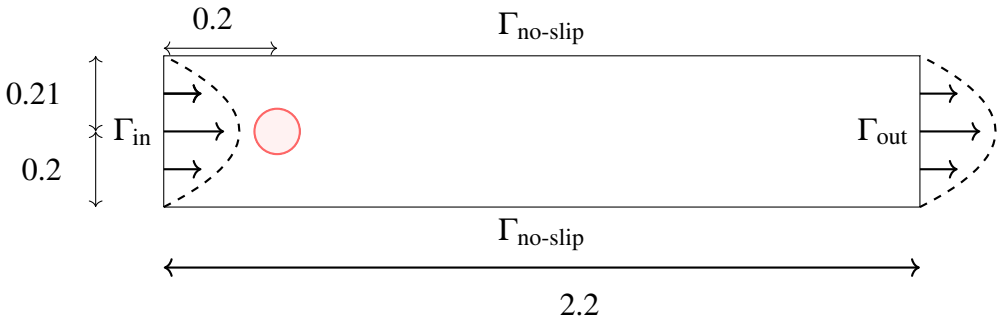

Figure 4.3: Configuration of flow around a cylinder benchmark.

Dirichlet boundary is defined at the inlet Γ_{in} with a parabolic profile

$$u_x(y) = \left(\frac{4.0 U_{\max} y(0.41 - y)}{(0.41)^2}, 0\right), \tag{4.5.1}$$

having maximum velocity $U_{\max} = 0.3$. The corresponding mean velocity $\mathcal{U}_{\text{mean}}$ is defined as

$$\mathcal{U}_{\text{mean}} = \frac{2}{3} U_{\max}. \tag{4.5.2}$$

No slip boundary condition is defined at the upper and lower walls and do-nothing boundary condition is defined at the outlet Γ_{out}. The characteristic length of the cylinder ($L = 2r_c = 0.1$) along with the viscosity η and mean velocity yields the Reynolds number $Re = 20$, depicting a laminar flow. Here r_c is the radius of the cylinder.

$$Re = \frac{\mathcal{U}_{\text{mean}} L}{\eta}. \tag{4.5.3}$$

Force acting on cylinder surface has two components i.e. lift and drag. Lift is perpendicular to the direction of flow, whereas drag is parallel to the direction of flow. The mathematical expressions for lift and drag are defined as (see [91])

$$\mathcal{F}_L = -\int_S (\eta \frac{\partial \mathbf{u}_\tau}{\partial \mathbf{n}} \mathbf{n}_1 - p\mathbf{n}_2) ds, \quad \mathcal{F}_D = \int_S (\eta \frac{\partial \mathbf{u}_\tau}{\partial \mathbf{u}} \mathbf{n}_2 - p\mathbf{n}_1) ds. \tag{4.5.4}$$

The dimensionless drag and lift coefficients are calculated with following definitions

$$C_D = \frac{2}{U_{\text{mean}}^2 L} \mathcal{F}_D, \qquad C_L = \frac{2}{U_{\text{mean}}^2 L} \mathcal{F}_L. \tag{4.5.5}$$

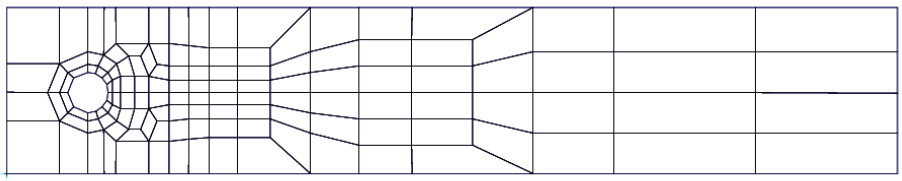

Figure 4.4: Flow around a cylinder benchmark coarse mesh.

4.5.1 Numerical Results

For testing the robustness and the efficiency of the resulting discretization in comparison with the standard Navier-Stokes solver. The numerical results illustrating the performance of system (2.0.1) for flow around a cylinder benchmark are presented in Table 4.1. Numerical results in the form of lift/drag coefficients are compared and validated with the

reference values [90] given as,

$$C_D = 5.57953523384, \qquad C_L = 0.010618948146,$$

and with the results of Damanik [77]. Convergence of the solution is presented for higher order finite elements (Q_2/P_1^{disc}). Where "NL" denotes non-linear iterations and "LL" denotes the average number of multigrid iterations. Each refinement level shows a strong agreement with the reference results. The qualitative solution in terms of velocity magnitude, pressure, and stream functions are presented in Fig. 4.5. Furthermore, an extended numerical study of the single-phase three-field system is conducted in Afaq et al. [25] as an intermediate step toward the validation of the monolithic multiphase three-field solver against the established benchmark problems.

Table 4.1: Validation of the lift and drag values of the flow around a cylinder in a rectangular channel. "NL" denotes non-linear iterations, "LL" denotes the average number of multigrid iterations. "L.I." and "V.I." stands for the line and volume integral.

	L.I.	**V.I.**		**Damanik (L.I.) [77]**	
Level	Lift/Drag	Lift/Drag	NL/LL	Lift/Drag	NL/LL
1	0.009497543/5.5550	0.009447476/5.5424	9/1	0.009498/5.5550	9/2
2	0.010600652/5.5722	0.010468846/5.5672	9/1	0.010601/5.5722	9/2
3	0.010615639/5.5776	0.010567879/5.5761	9/1	0.010616/5.5776	9/1
4	0.010617798/5.5791	0.010603975/5.5787	8/1	0.010618/5.5790	8/1
5	0.010618726/5.5794	0.010615029/5.5793	7/1		

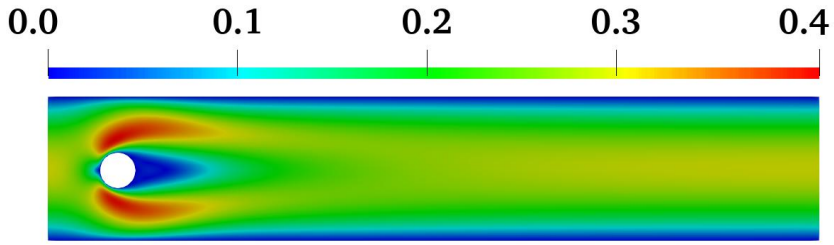

(a) Velocity magnitude

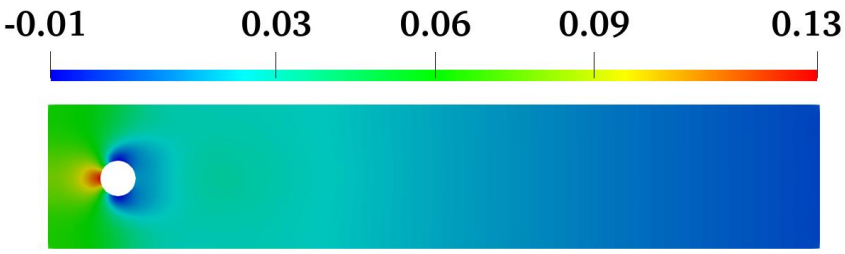

(b) Pressure distribution

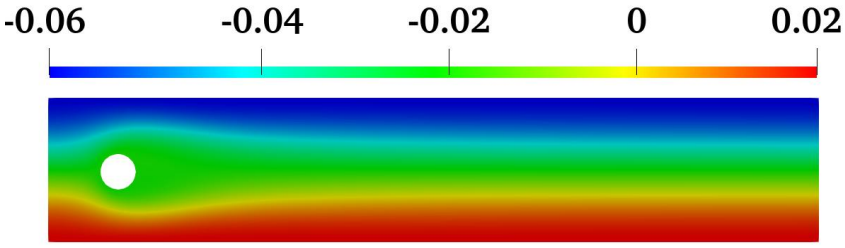

(c) Stream function

Figure 4.5: Visualization of the velocity, pressure, and stream function.

5

Numerical Studies

In this chapter, a series of detailed numerical experiments are conducted for a range of representative configurations involving multiphase flows. These studies aim to investigate the solvability and stability of the proposed computational framework. The approach is based on a three-field formulation, where the dynamics of a material cut-off function ψ are governed by an advection equation.

To ensure accurate spatial resolution, higher-order finite elements are employed: Q_2 element is used for both the velocity field and the material cut-off function, while the pressure field is discretized using discontinuous linear element P_1^{disc}. The entire non-linear system is solved monolithically, which allows for strong coupling between the variables and enhances the stability of the solution, particularly important for multiphase flows where sharp interfaces and strong gradients are present.

In the subsequent sections, the static bubble test is considered as an initial validation step, wherein the solver's performance is evaluated against an analytical expression (2.1.4) for the force applied on the right-hand side of the governing equations. Following successful validation, the multiphase model is applied to the same configuration, highlighting the ability of the formulation (2.6.3) to produce stable and physically consistent results while minimizing spurious numerical artifacts. Subsequently, an oscillating bubble scenario is examined to assess the temporal accuracy and robustness of the time integration schemes, as well as to study the role of surface tension in dynamic interface motion. The final part of the chapter addresses the capillary time step restriction (a critical constraint in unsteady multiphase flow simulations) and evaluates the solver's performance under this condition.

5.1 Static Bubble

A static bubble [92, 93, 94, 95] in a two-dimensional incompressible two-phase flow is a simple example for demonstrating the prototypical behaviour of multiphase flows. For simplicity, we consider a stationary bubble at equilibrium. Since the bubble is at rest inside the domain so it should show a zero velocity field but unfortunately spurious velocity is observed near the interface [92, 93, 94, 95]. Approximation of the incompressibility constraints, the interface and the local external force are the possible responsible sources for this phenomena [93]. The flow dynamics depends strongly on the magnitude of the spurious velocity, consequently, a non-physical movement of the interface might also be observed.

5.1.1 Geometrical Configuration

Both fluids are immiscible and separated by an interface Γ. The first fluid Ω_1 is completely inside of the second fluid Ω_2, as shown in Fig. 5.1. A circular static bubble of radius $r = 0.25$ is placed at the center $[0.5, 0.5]$ of a unit square $\overline{\Omega} = [0,1]^2$. The surface tension coefficient, viscosities, and densities are set to unity in the absence of the gravitational force.

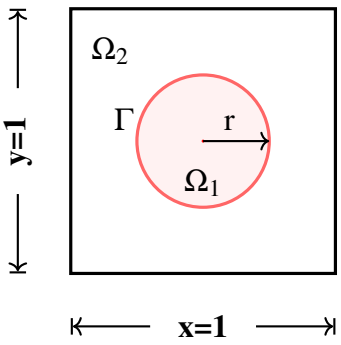

Figure 5.1: Geometrical configuration for the static bubble test.

The relation between the pressure (inside and outside the bubble) should satisfies Laplace-Young law

$$p_i = p_o + \frac{\sigma}{r}. \tag{5.1.1}$$

Here, p_i is the pressure inside the bubble, p_o is the pressure outside the bubble, and σ is the surface tension coefficient.

To begin with, a detailed numerical investigation is carried out for the CSF formulation

(2.1.4) and the results are compared against the benchmark data reported by Turek et al. [92]. The performance assessment focuses on the velocity magnitude errors, evaluated in both the $\|.\|_0$ and $\|.\|_1$ norms. The obtained results, given in Table 5.1, show very good agreement with the reference data and the pressure field is observed to satisfy Laplace-Young law.

	CSF formulation (2.1.4)				**Turek et al. [92]**			
L	$\frac{\|\mathbf{p_i}-\mathbf{p_o}\|}{(\sigma/\mathbf{r})}$	$\|\mathbf{u}-\mathbf{u_h}\|_{\mathbf{0}}$	$\|\mathbf{u}-\mathbf{u_h}\|_{\mathbf{1,h}}$	**NL/LL**	$\frac{\|\mathbf{p_i}-\mathbf{p_o}\|}{(\sigma/\mathbf{r})}$	$\|\mathbf{u}-\mathbf{u_h}\|_{\mathbf{0}}$	$\|\mathbf{u}-\mathbf{u_h}\|_{\mathbf{1,h}}$	**NL/LL**
4	1.040583	$1.22e-3$	$5.63e-2$	4/1	0.954349	$2.61e-3$	$2.08e-1$	5/1
5	0.999839	$9.58e-5$	$1.28e-2$	5/1	0.979682	$9.71e-4$	$1.54e-1$	5/1
6	1.000969	$4.98e-5$	$5.26e-3$	5/1	0.992961	$3.62e-4$	$1.13e-1$	4/1
7	1.000204	$2.10e-6$	$1.03e-3$	6/1	0.997166	$1.38e-4$	$8.21e-2$	4/1

Table 5.1: Validation of pressure and velocity errors for the static bubble test with Turek et al. [92], at mesh refinement $h = 1/16$, $1/32$, $1/64$, and $1/128$.

An important observation is the noticeable reduction of spurious velocity, even at the 5th refinement level ($h = 1/32$), which can be attributed to the higher-order velocity approximation employed in the discretization. This enhanced spatial accuracy contributes significantly to suppressing non-physical oscillations near the fluid interface. At the finest investigated mesh resolution $h = 1/128$, the magnitude of the spurious velocity decreases to $1e-6$, which is lower than the corresponding values reported in the reference study [92]. Any inaccuracy in curvature computation or in velocity interpolation can lead to an imbalance, which manifests as spurious currents. By resolving the interface geometry and velocity field more accurately, the higher-order discretization reduces curvature approximation errors and improves the consistency between the discrete pressure and velocity fields, thereby suppressing non-physical oscillations. This effect becomes more pronounced at finer mesh levels, explaining the observed superior performance compared to the reference results.

5.1.2 Finite Element Choice for Material Cut-off Function

The selection of a suitable finite element space for the material cut-off function ψ is a crucial aspect of the numerical formulation. The chosen element should strike an optimal balance between minimizing numerical errors and maintaining computational efficiency. To investigate this trade-off, a comparative study is carried out using three different finite element discretizations for ψ i.e. P_1^{disc}, Q_1, and Q_2, respectively, summarized in Table 5.2.

DOF	$\mathbf{u}, p, \psi$	$\frac{\|\mathbf{p_i}-\mathbf{p_o}\|}{(\sigma/\mathbf{r})}$	$\|\mathbf{u}-\mathbf{u_h}\|_{\mathbf{0}}$	$\|\mathbf{u}-\mathbf{u_h}\|_{\mathbf{1,h}}$
57858	$Q_2P_1^{disc}P_1^{disc}$	0.980040	$3.66e-4$	$3.67e-2$
49795	$Q_2P_1^{disc}Q_1$	1.033480	$5.44e-5$	$2.17e-2$
62211	$Q_2P_1^{disc}Q_2$	1.036427	$1.62e-7$	$7.57e-5$

Table 5.2: Pressure and velocity errors obtained for three different sets of finite elements, at the mesh refinement $h = 1/64$.

One of the key physical checks of the proposed formulation is its ability to reproduce the pressure difference according to the Laplace-Young law. For the Q_2 and Q_1 elements, this condition is satisfied accurately, indicating that the pressure field remains physically consistent. In contrast, for the P_1^{disc} element, the computed pressure ratio approaches unity but is not exact, exhibiting a slight deviation from the ideal physical balance. The velocity error analysis, based on both L_2 and H_1 norms, shows that Q_2 provides the most accurate results, followed by Q_1, with P_1^{disc} being the least accurate in this respect.

5.1.3 Numerical Results

The numerical study is carried out for the systems of equations (2.6.3), a three-field formulation. The interface thickness ϵ is chosen to be $1.5h$ and $0.7h$, the time step is fixed at $\Delta t = 1e-2$ until time $t = 100$.

The study reveals the presence of spurious velocity (parasitic currents), which are visualized in Fig. 5.2 (a,b). Despite the occurrence of these small non-physical flows, the computed pressure difference converges to the theoretical value of 4. This agreement confirms that the pressure jump across the interface satisfies the Laplace-Young law, shown in Fig. 5.2 (c,d) and 5.3, indicating that the surface tension force is correctly represented in this formulation.

A key numerical parameter influencing the solution is the interface thickness ϵ, which controls the smoothing of the material cut-off function. Reducing ϵ produces a narrower transition region between two fluids, thereby localizing the interface representation. In this approach, the surface tension force is computed directly from the gradient of the ψ, without requiring explicit curvature calculation. A smaller ϵ steepens this gradient, effectively concentrating the force in a thinner region and yielding a sharper and more pronounced pressure jump. This explains why decreasing ϵ leads to more distinct interface representation in both the pressure and ψ profiles. While such sharpness can enhance physical accuracy, it also demands careful consideration, as excessively small values of ϵ

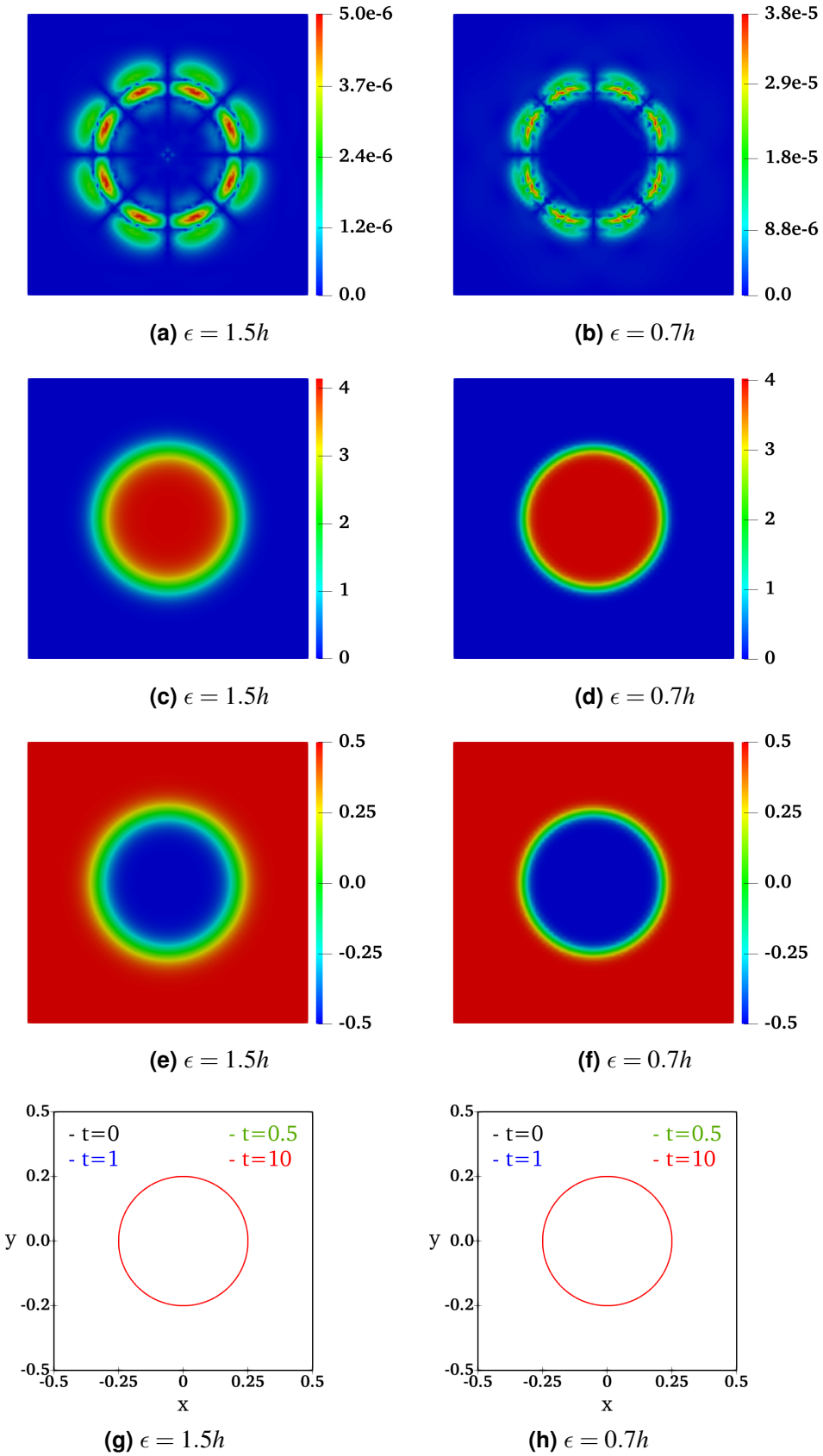

(a) $\epsilon = 1.5h$ **(b)** $\epsilon = 0.7h$

(c) $\epsilon = 1.5h$ **(d)** $\epsilon = 0.7h$

(e) $\epsilon = 1.5h$ **(f)** $\epsilon = 0.7h$

(g) $\epsilon = 1.5h$ **(h)** $\epsilon = 0.7h$

Figure 5.2: Magnitude of spurious velocity (a,b), pressure (c,d), ψ (e,f), and bubble shape (g,h), for two interface thickness ϵ, at mesh refinement $h = 1/64$.

may introduce numerical oscillations (see results in section 5.1.7). Similarly, the material cut-off function ψ, shown in Fig. 5.2 (e,f), reflects the same influence of ϵ. A smaller interface thickness parameter results in a sharper step profile along the cut-line, confirming the direct link between ϵ and the resolution of the interface in the computational domain.

The bubble shape, depicted in Fig. 5.2 (g,h), demonstrates that the formulation maintains an accurate and stable interface throughout the simulation.

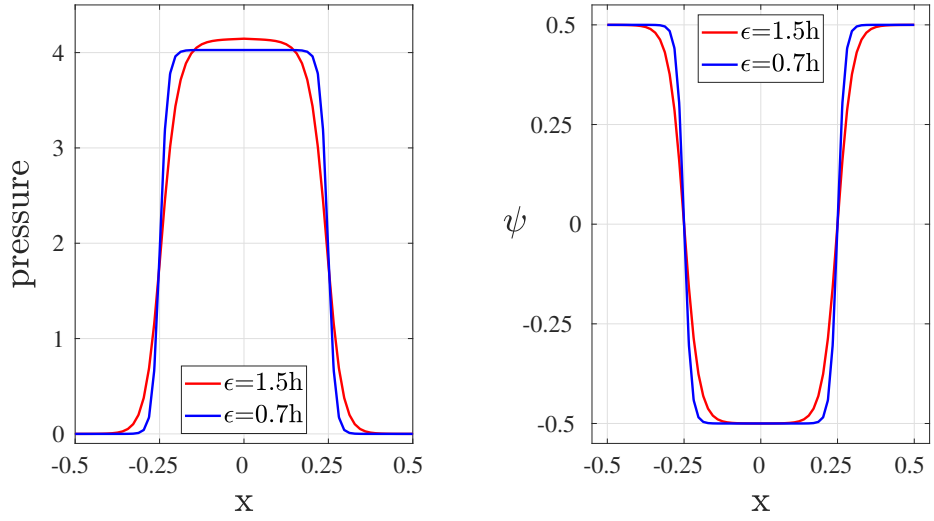

Figure 5.3: Pressure and ψ profiles along a cut-line at $y = 0$, for two interface thickness ϵ, at mesh refinement $h = 1/64$.

5.1.4 Surface Tension Effects

Surface tension is a key physical mechanism in multiphase flows, as it directly influences the stability and dynamics of the interface separating different fluid phases. In the present curvature free material cut-off formulation, the magnitude of the surface tension force is determined by the coefficient σ, which appears in the momentum equation (2.6.3). To assess its influence, a numerical study is conducted, consisting a focused evaluation of how changes in σ affect numerical artifacts, particularly the magnitude of spurious velocity.

In this study, the value of σ is progressively increased from 1 to 100. The results, shown in Fig. 5.4, demonstrate a clear trend: as σ increases, the magnitude of spurious velocity rises from approximately $1e-6$ to $1e-3$. This behavior can be attributed to the stronger interfacial force generated by higher σ values, which in turn amplifies any imbalance in the discrete momentum equation. The current CSS framework avoids the noise amplification often associated with curvature estimation. Nevertheless, the increased force intensity

at higher σ still magnifies local discretization errors, which appear as larger spurious currents. Hence, it can lead to interface displacement errors over time and in extreme cases, misrepresent the actual flow physics.

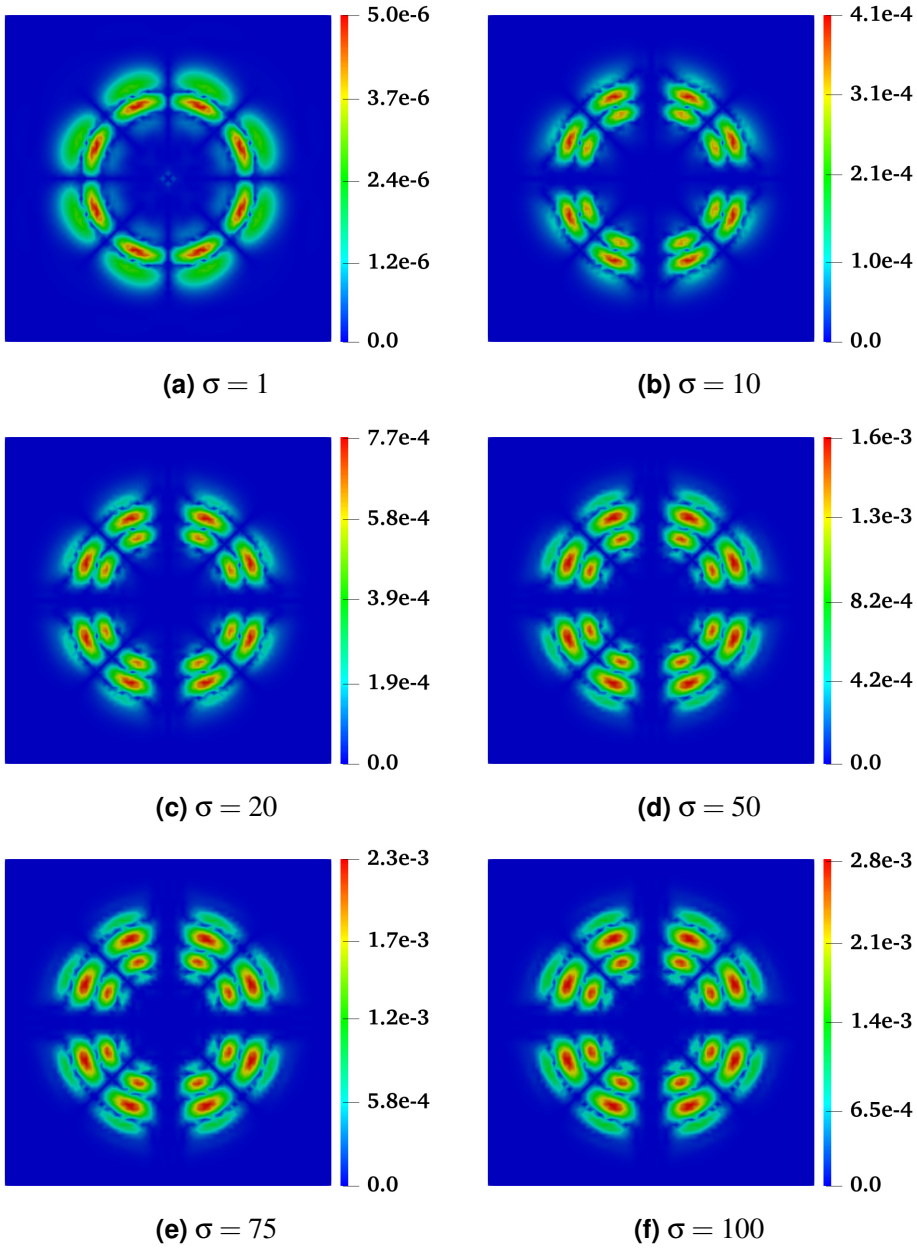

(a) $\sigma = 1$ **(b)** $\sigma = 10$

(c) $\sigma = 20$ **(d)** $\sigma = 50$

(e) $\sigma = 75$ **(f)** $\sigma = 100$

Figure 5.4: Spurious velocity magnitude for different values of surface tension constant ($\sigma = 1$, 10, 20, 50, 75, and 100), at mesh refinement $h = 1/64$.

5.1.5 Capillary Time Restriction

One of the most significant numerical implications of surface tension force treatment in multiphase flow simulations is its influence on the allowable time step size. When the surface tension term is incorporated explicitly, a stability constraint arises, imposing an upper bound on the time step Δt. This limit is widely known as the capillary time step restriction [21], which can severely impact computational efficiency and total execution time [96]. In the case of an explicit treatment of the surface tension force, the discrete stability condition takes the form [21]

$$\frac{c^{\text{cap}}\Delta t_h^{\text{cap}}}{h} < 1, \tag{5.1.2}$$

where c^{cap} is the phase velocity of capillary waves and h is the mesh size. Substituting the capillary wave speed into this expression yields the more familiar form

$$\Delta t_h^{\text{cap}} < \sqrt{\frac{\rho h^3}{\sigma}}, \tag{5.1.3}$$

with ρ denoting the fluid density and σ the surface tension coefficient. This relation shows that the maximum stable time step decreases rapidly with mesh refinement ($h \to 0$) or with larger σ, making simulations computationally expensive for fine resolutions or high surface tension flows.

Brackbill et al. [21] hypothesized that an implicit treatment of surface tension could relax or even completely remove this restriction. In the present framework, the surface tension force is incorporated fully implicitly within the momentum equation. This approach inherently avoids the explicit stability limitation and enables larger time steps without compromising stability. From a numerical perspective, the implicit formulation couples the surface tension force directly with the velocity-pressure solution process, meaning that the interfacial restoring force is balanced within the same non-linear solver step rather than being treated as a separate explicit update. As a result, high frequency capillary waves (which are responsible for the severe time step constraint) are effectively damped, allowing stable simulations with much larger Δt. The advantages of this treatment are demonstrated in Fig. 5.5, which compares the CSF formulation (2.1.9) with the CSS formulations (2.3.23) and (2.6.3) in the static bubble test.

The numerical study is performed using a mesh resolution of $h = 1/64$, which, according to the capillary time step restriction, suggests that Δt should not exceed 0.002 (when surface tension is treated explicitly). This value is calculated after substituting the corre-

sponding parameters value ($\rho = 1$, $\sigma = 1$, $h = 1/64$) in the equation (5.1.3). The results reveal that, for the level set based CSF formulation, the computed pressure difference fails to satisfy the Laplace-Young law when using large time steps ($\Delta t = 5$ and 10). In contrast, both implementations of the CSS formulation accurately reproduce the expected pressure jump of magnitude 4 across the interface, even for these large time steps. This provides clear numerical evidence that the CSS formulation, with its fully implicit treatment of surface tension, is not subject to the capillary time step restriction and remains stable and accurate for time steps well beyond the explicit stability limit.

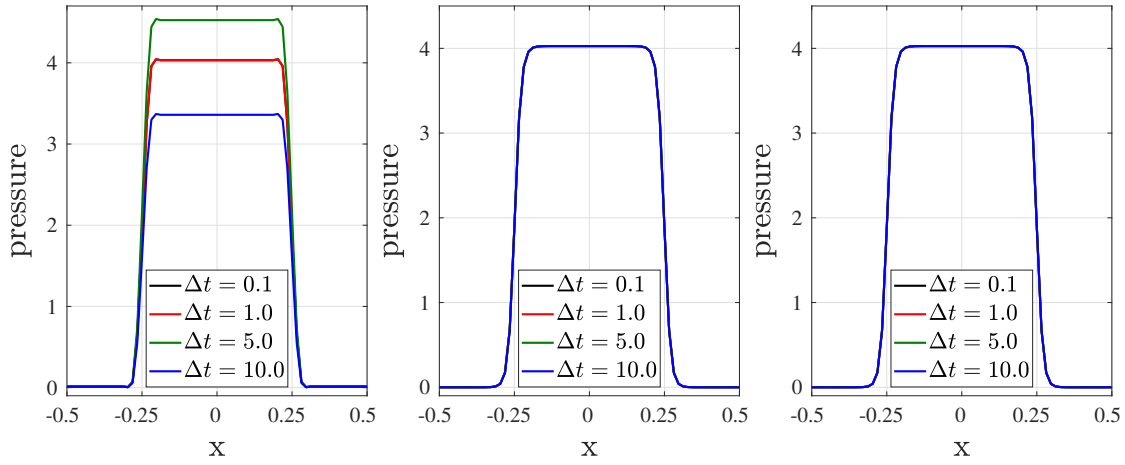

(a) Level set approach **(b)** Curvature free level set **(c)** Curvature free cut-off

Figure 5.5: Pressure profiles along the cut-line $y = 0$ obtained using the CSF formulation (a) and the CSS formulations (b, c), for four different time step sizes Δt, at mesh refinement $h = 1/64$.

5.1.6 Choice of Interface Thickness

As previously discussed, the interface thickness plays a pivotal role in the accuracy of multiphase flow simulations. To examine this influence, five distinct values of ϵ are evaluated using a refined spatial resolution of $h = 1/128$. The corresponding physical fields such as velocity magnitude, pressure difference, and ψ are illustrated in Figs. 5.6, 5.7, 5.8, and 5.9, respectively. As anticipated, an excessively small interface thickness ($\epsilon = 0.25h$) leads to noticeable inaccuracies, whereas the remaining values of ϵ yield results in close agreement with the expected physical behaviour.

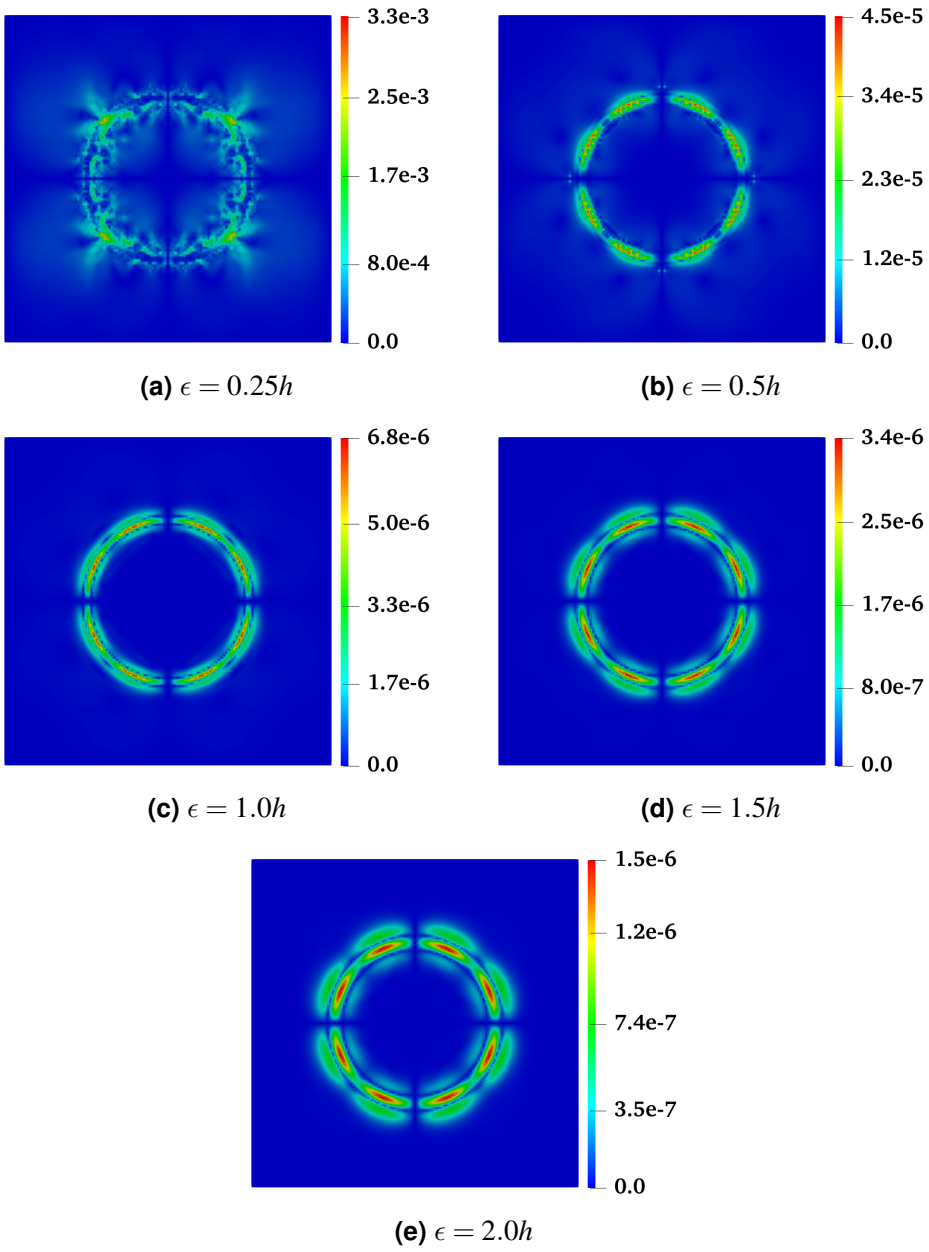

(a) $\epsilon = 0.25h$ **(b)** $\epsilon = 0.5h$

(c) $\epsilon = 1.0h$ **(d)** $\epsilon = 1.5h$

(e) $\epsilon = 2.0h$

Figure 5.6: Magnitude of the spurious velocity for different interface thickness ϵ, at mesh refinement $h = 1/128$.

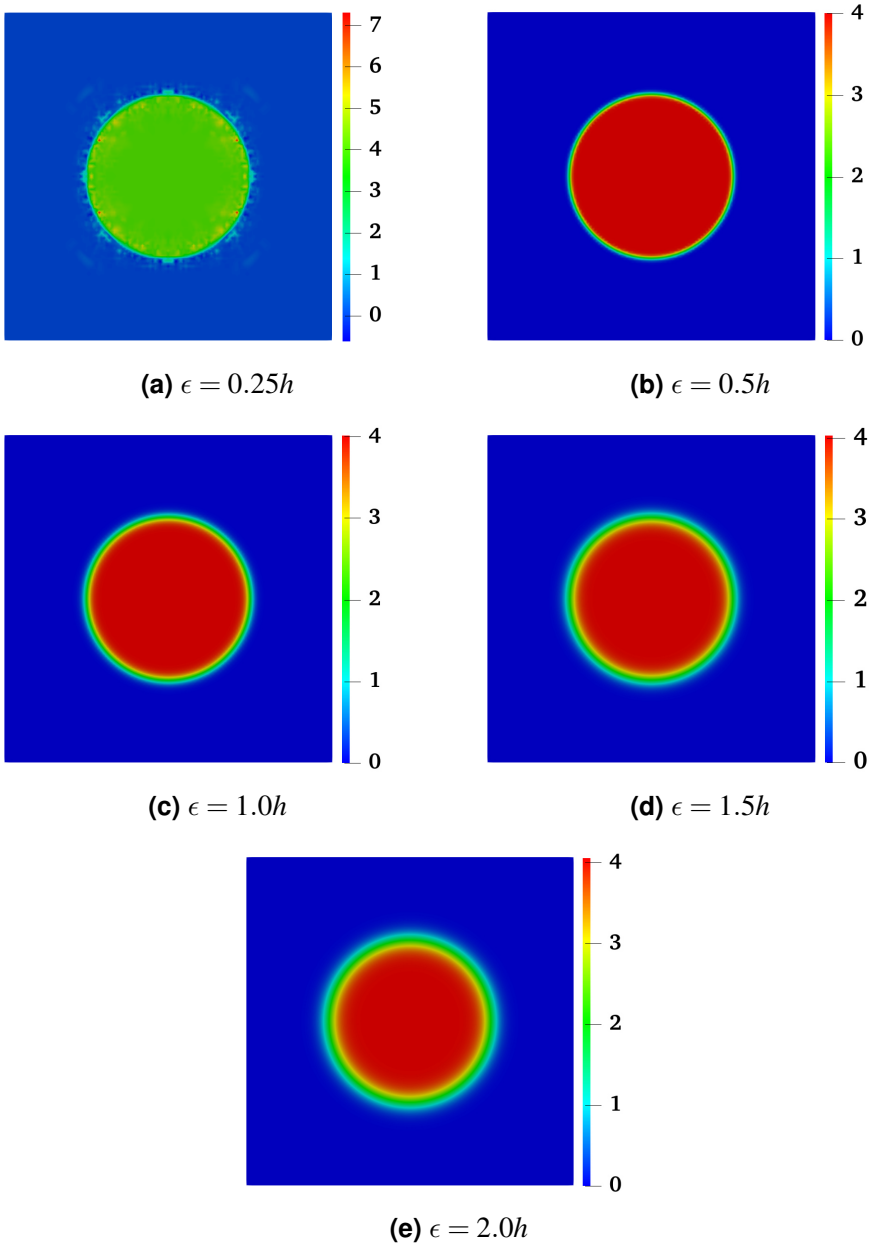

(a) $\epsilon = 0.25h$ **(b)** $\epsilon = 0.5h$

(c) $\epsilon = 1.0h$ **(d)** $\epsilon = 1.5h$

(e) $\epsilon = 2.0h$

Figure 5.7: Magnitude of the pressure for different interface thickness ϵ, at mesh refinement $h = 1/128$.

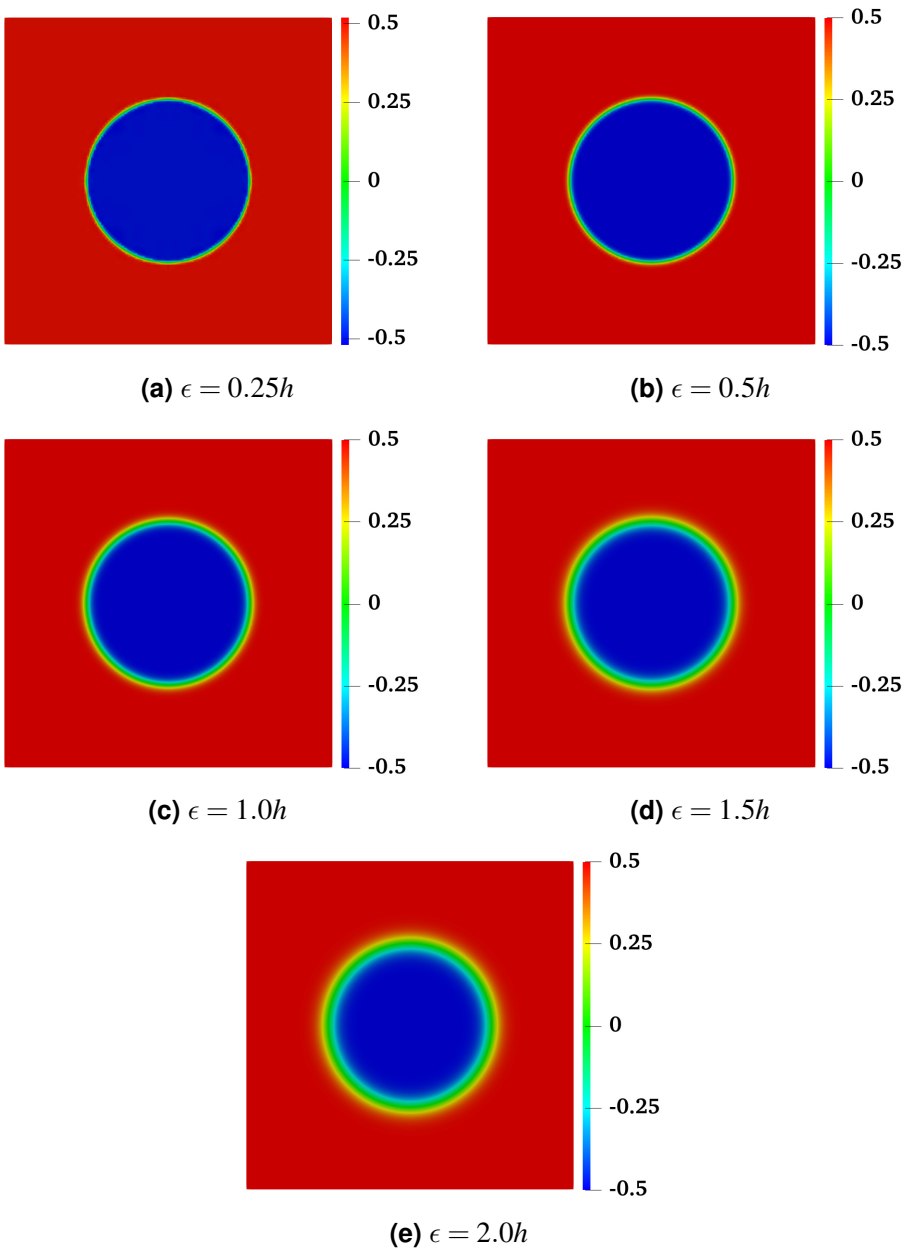

(a) $\epsilon = 0.25h$ **(b)** $\epsilon = 0.5h$

(c) $\epsilon = 1.0h$ **(d)** $\epsilon = 1.5h$

(e) $\epsilon = 2.0h$

Figure 5.8: Magnitude of the material cut-off function for different interface thickness ϵ, at mesh refinement $h = 1/128$.

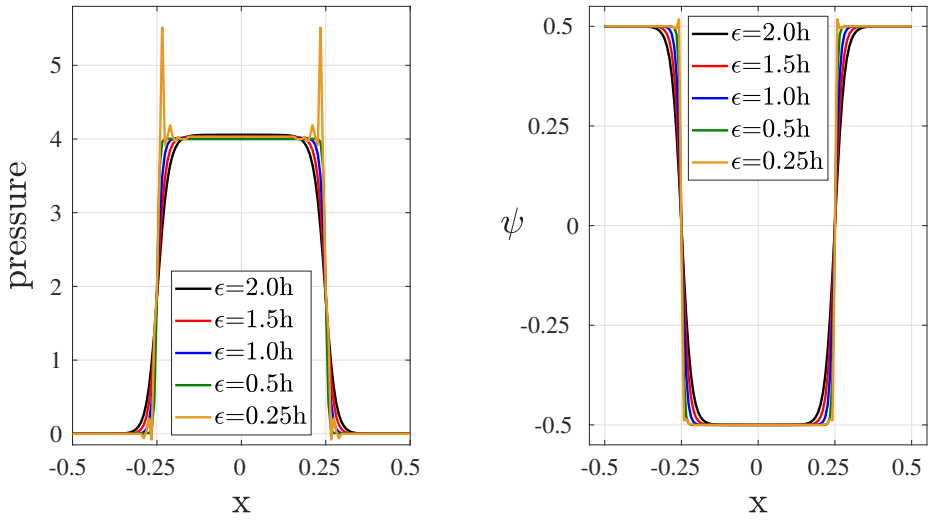

Figure 5.9: Pressure and ψ profiles along a cut-line at $y = 0$, for different interface thickness ϵ, at mesh refinement $h = 1/128$.

5.1.7 Compression and Diffusion Effects

In the preceding subsections, we have already examined several key parameters, including the interface thickness parameter ϵ, the surface tension coefficient σ, and the time step Δt. In this section, we focus on assessing the influence of two additional terms, the compression and diffusion contributions in the transport equation of ψ. Although the static bubble configuration used here is relatively simple and free from strong non-linear effects, it provides a controlled setting to study the impact of these terms on the behavior of the material cut-off function.

The investigation proceeds by varying the parameters γ_1 (compression) and γ_2 (diffusion). In the top row of Fig. 5.10, we observe the effect of increasing γ_1: a higher compression magnitude distorts the range ψ, pushing it outside its intended bounds. To counteract this, we adjust γ_2 in the bottom row of Fig. 5.10, keeping $\gamma_1 = 1e-2$ fixed. The results clearly show that suitable values of γ_2 restore the correct range of ψ.

This behavior aligns with the earlier discussion that γ_2 plays a beneficial role: the diffusion term counterbalances the compression term and controls the smoothness of the interface. This influence is demonstrated in Figs. 5.11 and 5.12. In these results, a small and appropriately chosen value of γ_2 is introduced into the previously oscillatory static bubble solution obtained with an excessively small interface thickness ϵ. The inclusion of this diffusive contribution significantly improves numerical stability, allowing the solution to converge and recover the correct pressure jump in accordance with the Laplace-Young

law. This clearly highlights the role of diffusion term: by providing localized smoothing when the interface is unrealistically sharp, it mitigates convergence issues and suppresses spurious oscillations, as evidenced by the comparison in Fig. 5.12.

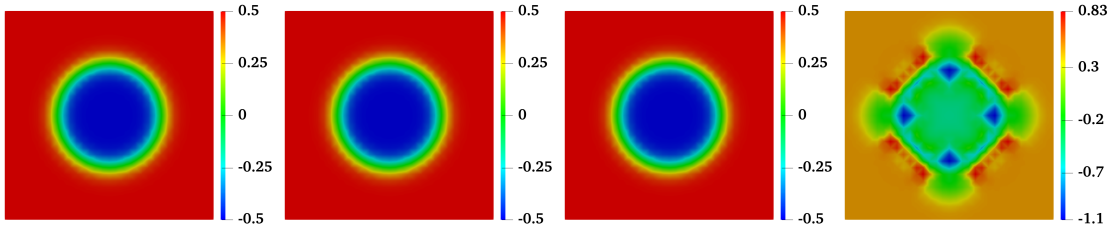

(a) $\gamma_1 = 1e-5$ **(b)** $\gamma_1 = 1e-4$ **(c)** $\gamma_1 = 1e-3$ **(d)** $\gamma_1 = 1e-2$

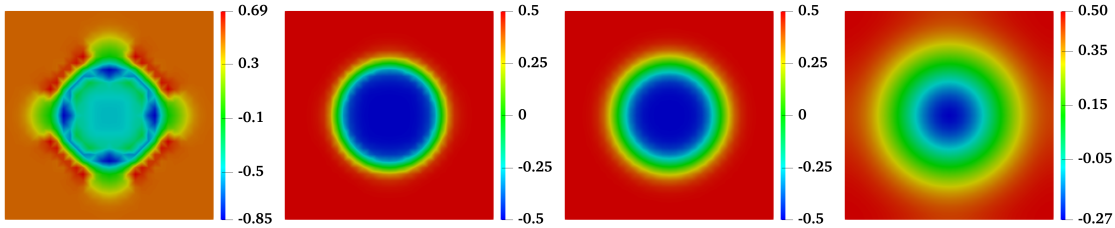

(e) $\gamma_2 = 1e-5$ **(f)** $\gamma_2 = 1e-4$ **(g)** $\gamma_2 = 1e-3$ **(h)** $\gamma_2 = 1e-2$

Figure 5.10: Magnitude of ψ for different magnitudes of the compression γ_1 and the diffusion γ_2, at mesh refinement $h = 1/64$.

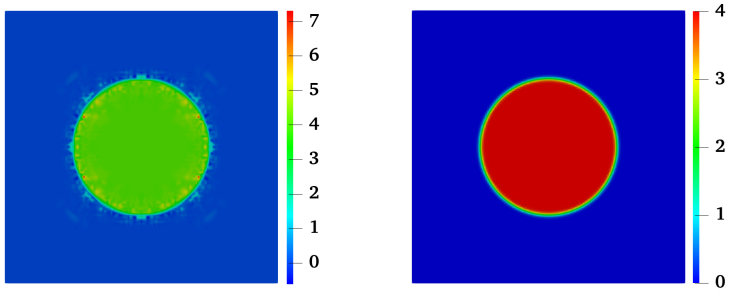

(a) $\gamma_2 = 0$ **(b)** $\gamma_2 = 1e-5$

Figure 5.11: Magnitude of the pressure with and without γ_2 for interface thickness $\epsilon = 0.25h$, at mesh refinement $h = 1/128$.

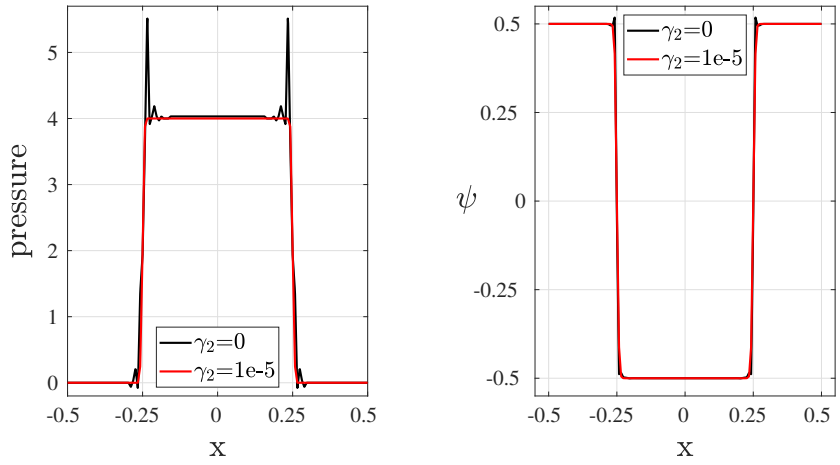

Figure 5.12: Pressure and ψ profiles along a cut-line at $y = 0$ with and without γ_2, for interface thickness $\epsilon = 0.25h$, at mesh refinement $h = 1/128$.

5.2 Oscillating Bubble

In this section, a more advanced and dynamic configuration the oscillating bubble is examined, where the interface evolves in time rather than being stationary. The initial geometry consists of a stationary ellipse with semi-major axis $r_x = 0.25$ and semi-minor axis $r_y = 0.125$, positioned at the center $[0.5, 0.5]$ of the unit square domain $\overline{\Omega} = [0,1]^2$, illustrated in Fig. 5.13. The surface tension coefficient, viscosities, and densities are set to unity, γ_1 and γ_2 are set to zero and gravitational effects are neglected. According to the analytical expectation, the surface tension will drive the interface toward a state of minimal curvature, causing the initially elliptical bubble to undergo oscillations and eventually relax into its equilibrium configuration, a stable circular bubble [72]. This well-defined physical behavior makes the oscillating bubble an excellent example for validating the ability of a numerical solver to handle dynamic multiphase interfaces with high accuracy.

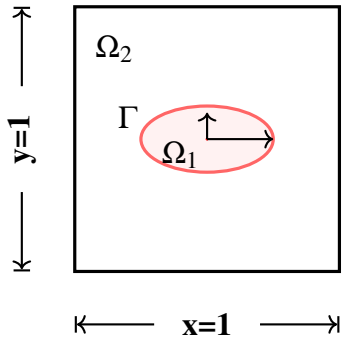

Figure 5.13: Geometrical configuration for the oscillating bubble test.

The numerical study is performed for a fixed time step of $\Delta t = 1e-2$ until time $t = 100$. To evaluate the accuracy and stability of the method, two physically relevant quantities are monitored: the instantaneous bubble radius and the corresponding surface area. The bubble radius provides insight into the relaxation dynamics and confirms whether the bubble evolves toward its expected equilibrium configuration, namely a stable circular shape. At the same time, monitoring the surface area offers a direct measure of numerical mass conservation, since the enclosed volume of the bubble should remain invariant during the oscillation process. Together, these diagnostics ensure that the formulation not only captures the transient oscillatory behavior correctly but also maintains the accuracy of the solution.

5.2.1 Comparison of Time Stepping Schemes

As outlined previously in section 4.1, both the Crank-Nicolson (CN) and Backward Euler (BE) schemes are A-stable and therefore suitable candidates for unsteady multiphase simulations. Nevertheless, each scheme has distinct characteristics, which motivates a comparative investigation in the oscillating bubble to assess whether one should be preferred over the other.

The tests are conducted for the system of equations (2.6.3) using three mesh refinements $h = 1/16$, $1/32$, and $1/64$, respectively. The temporal evolution of the bubble radii (in both x- and y-directions) and its surface area are shown in Figs. 5.14 and 5.15, with logarithmic views presented in the right column. The results demonstrate that, after an initial phase of few oscillations, the bubble relaxes into a steady equilibrium state. Moreover, the results confirm that the enclosed area remains constant throughout the simulation, indicating no mass loss providing the mesh is refined enough. As theoretically expected, the initially elliptical bubble evolves into a stable circular shape. In conclusion, both time discretization schemes yield stable solutions without numerical instabilities. However, since CN provides second order accuracy in time, it is preferred choice in subsequent studies.

The evolution of the bubble shape is illustrated in Figs. 5.16 and 5.17. These snapshots highlight the transition from the initial elliptical geometry to the final circular equilibrium shape. The zoom-in views further capture the interface dynamics, showing that after approximately $t = 5$, the bubble has largely relaxed and a stable circular configuration is achieved.

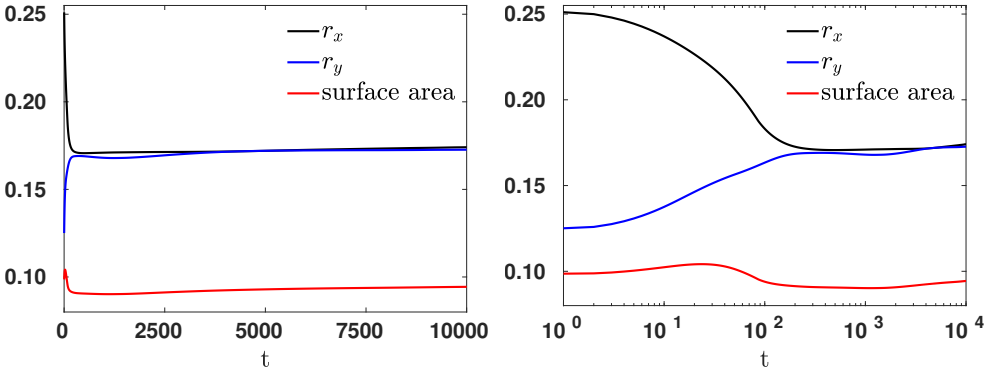

(a) $h = 1/16$ **(b)** $h = 1/16$, log-scale

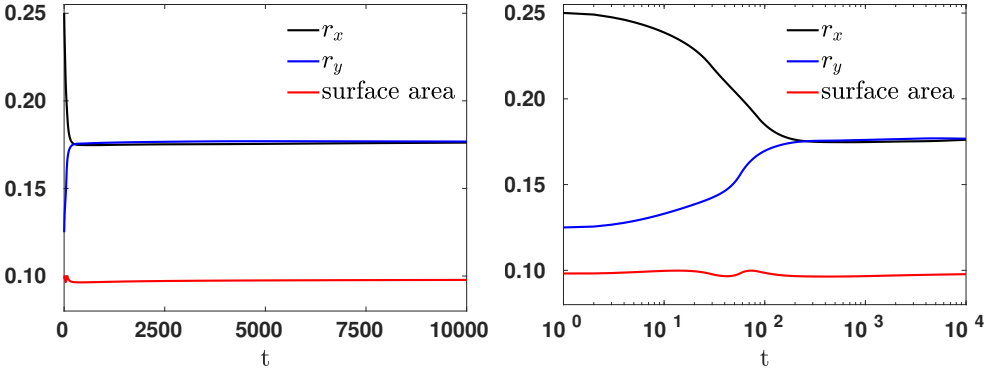

(c) $h = 1/32$ **(d)** $h = 1/32$, log-scale

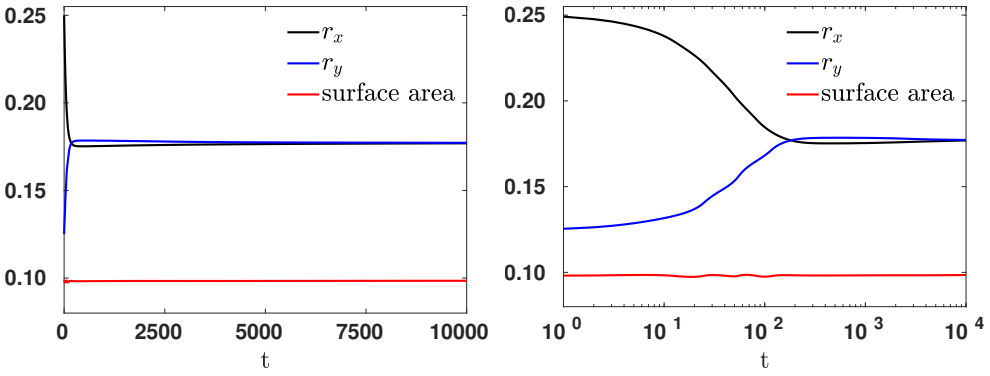

(e) $h = 1/64$ **(f)** $h = 1/64$, log-scale

Figure 5.14: Bubble Radii (r_x, r_y) and surface area, using Crank-Nicolson scheme for $\epsilon = 1.5h$, at mesh refinement level $h = 1/16,\ 1/32$, and $1/64$.

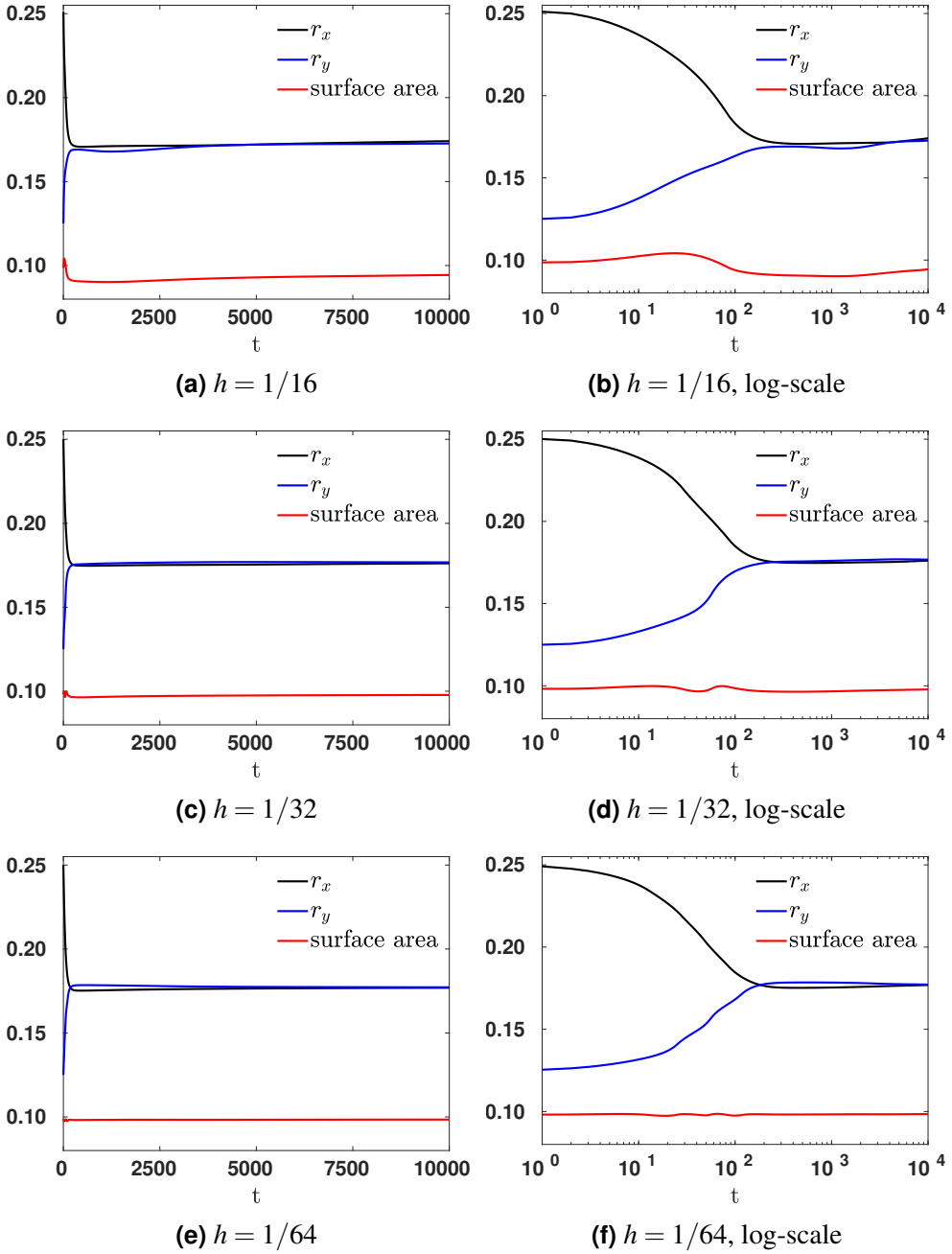

(a) $h = 1/16$ **(b)** $h = 1/16$, log-scale

(c) $h = 1/32$ **(d)** $h = 1/32$, log-scale

(e) $h = 1/64$ **(f)** $h = 1/64$, log-scale

Figure 5.15: Bubble Radii (r_x, r_y) and surface area, using Backward Euler scheme for $\epsilon = 1.5h$, at mesh refinement level $h = 1/16,\ 1/32$, and $1/64$.

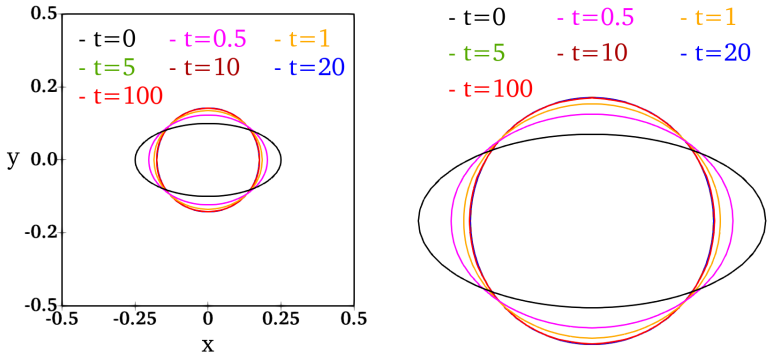

(a) $h = 1/64$ **(b)** $h = 1/64$, zoom-view

Figure 5.16: Bubble evolution, using Crank-Nicolson scheme for $\epsilon = 1.5h$, at mesh refinement level $h = 1/16,\ 1/32$, and $1/64$.

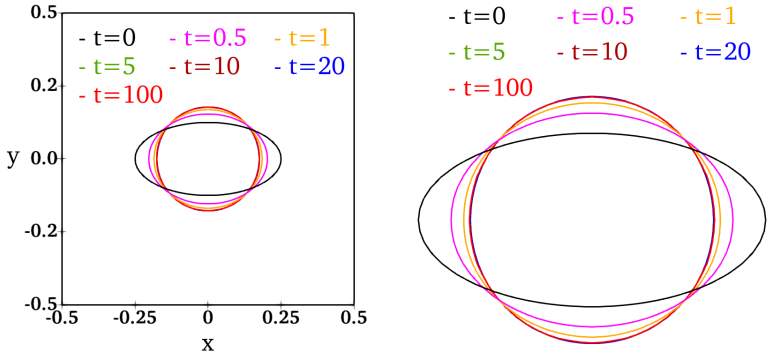

(a) $h = 1/64$ **(b)** $h = 1/64$, zoom-view

Figure 5.17: Bubble evolution, using Backward Euler scheme for $\epsilon = 1.5h$, at mesh refinement level $h = 1/16,\ 1/32$, and $1/64$.

5.2.2 Surface Tension Effects

In continuation of the static bubble analysis, we now investigate the influence of surface tension on the oscillating bubble configuration. The numerical study is carried out for the system of equations (2.6.3) with a fixed time step $\Delta t = 1e-2$, integrated up to a final time $t = 100$. The compression and diffusion terms are deactivated ($\gamma_1 = \gamma_2 = 0$), while the surface tension coefficient is chosen as $\sigma = 1$, 10, 25, 50, and 100, respectively. The computations are performed on mesh refinement $h = 1/32$, employing the Crank-Nicolson time discretization scheme.

The temporal evolution of the bubble radii (r_x, r_y) and the corresponding surface area, containing the original time (left) and its logarithmic representation (right), are presented in Fig. 5.19. For clarity, both the original time series (left column) and their logarithmic representation (right column) are shown. The results reveal that increasing σ accelerates

the relaxation process of the interface, allowing the bubble to reach its steady circular configuration more rapidly. This trend is particularly evident in the logarithmic plots, where higher values of σ display steeper damping of oscillations. However, it is also observed that for $\sigma > 1$, the surface area does not remain constant, indicating a gradual mass loss during the evolution.

To further investigate the influence of σ, representative bubble shapes at selected time instants are depicted in Fig. 5.20. These visualizations confirm that, except for the lowest value $\sigma = 1$, all other cases achieve nearly circular equilibrium shape already by $t \approx 0.5$. A noteworthy observation is shown in Fig. 5.21, where the final bubble shape remains circular as expected, but its centroid exhibits a slight displacement from the initial position.

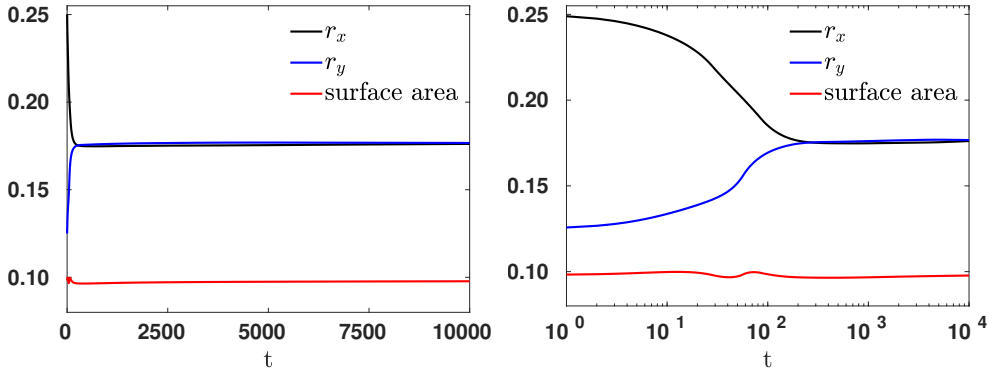

(a) $\sigma = 1$ **(b)** $\sigma = 1$, log-scale

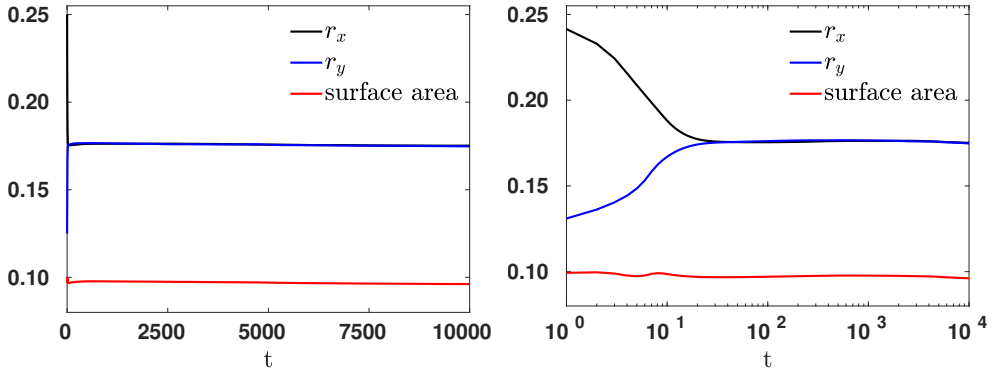

(c) $\sigma = 10$ **(d)** $\sigma = 10$, log-scale

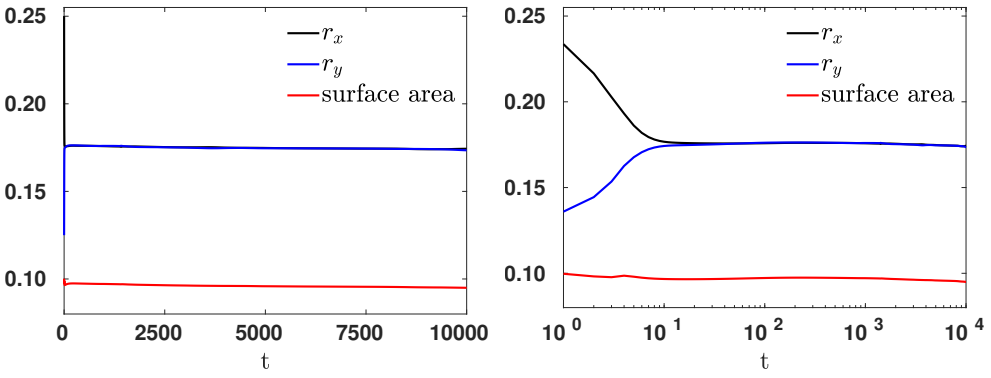

(a) $\sigma = 25$ **(b)** $\sigma = 25$, log-scale

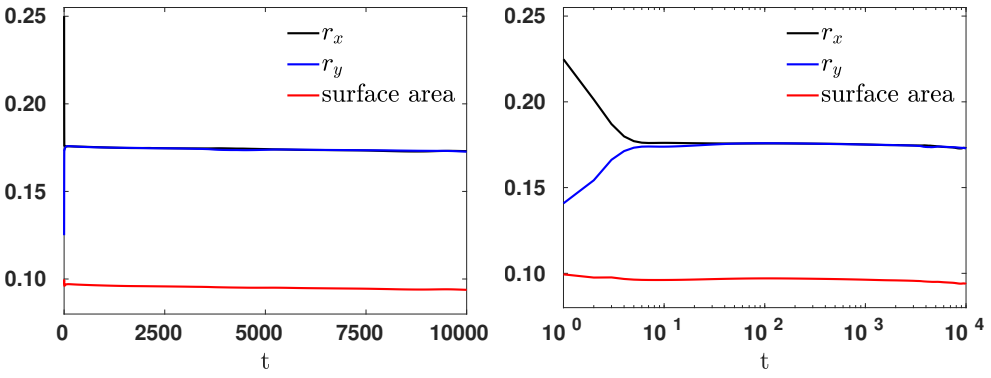

(c) $\sigma = 50$ **(d)** $\sigma = 50$, log-scale

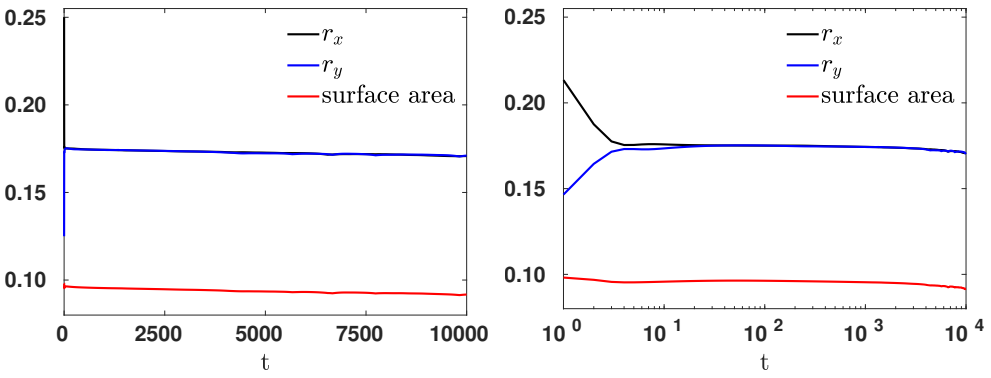

(e) $\sigma = 100$ **(f)** $\sigma = 100$, log-scale

Figure 5.19: Bubble Radii (r_x, r_y) and surface area for different values of surface tension constant ($\sigma = 1$, 10, 25, 50, and 100), at mesh refinement $h = 1/32$.

From a physical perspective, these results are consistent with the role of surface tension in multiphase flows. A larger σ increases the restoring force associated with curvature, which enhances the speed of interface relaxation and suppresses long-lasting oscillations. At the same time, higher values of σ amplify capillary-induced velocities, which in a numerical setting may generate stronger spurious currents. These unphysical flows can distort the phase distribution and lead to deviations in conserved quantities such as mass (observed as surface area reduction in the present study). The slight displacement of the bubble center for high σ further reflects the sensitivity to such spurious effects, despite the fact that the final equilibrium shape is correctly recovered.

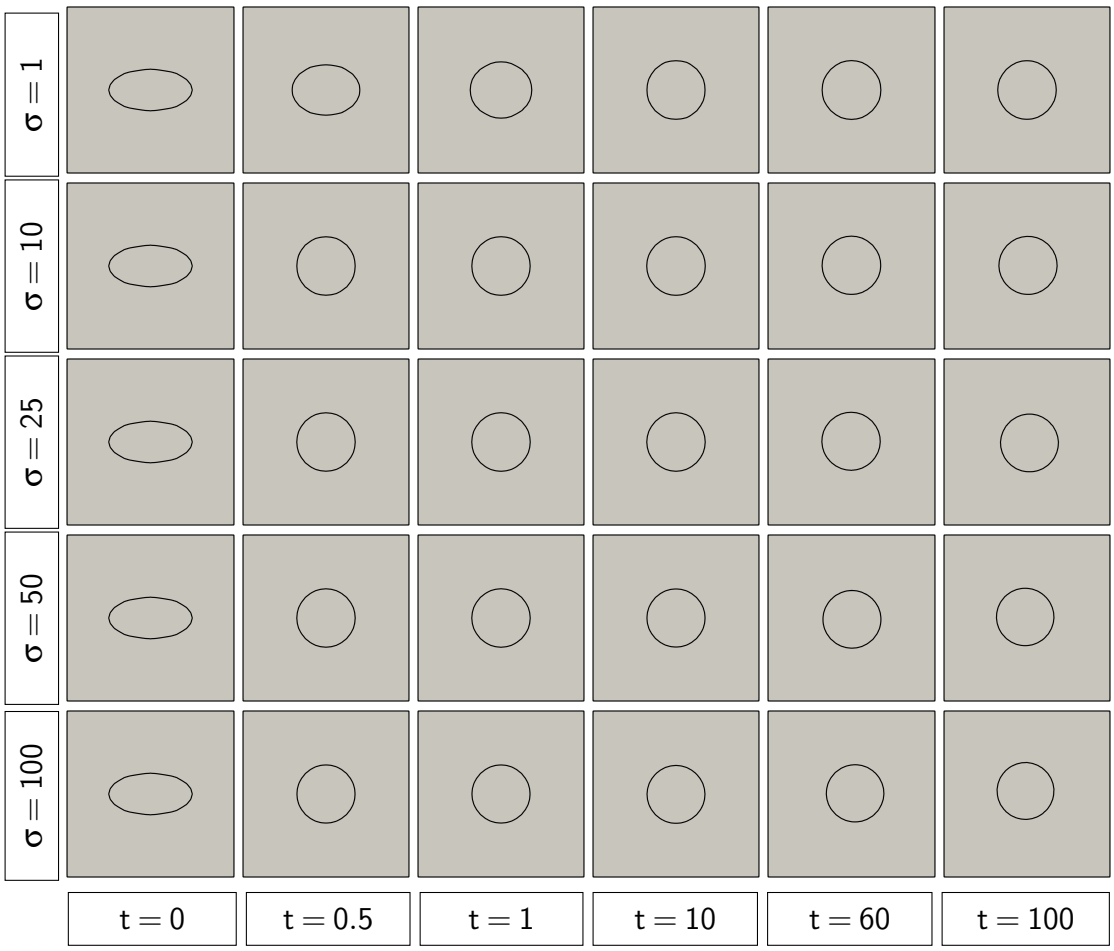

Figure 5.20: Bubble evolution for different values of surface tension constant ($\sigma = 1$, 10, 25, 50, and 100), at mesh refinement $h = 1/32$.

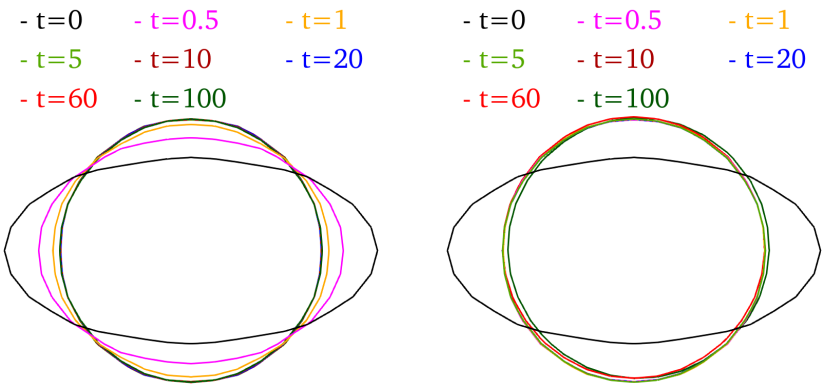

(a) $\sigma = 1$ **(b)** $\sigma = 10$

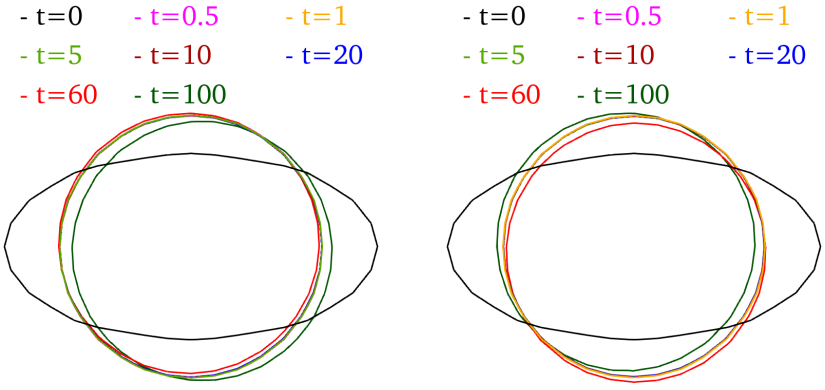

(c) $\sigma = 25$ **(d)** $\sigma = 50$

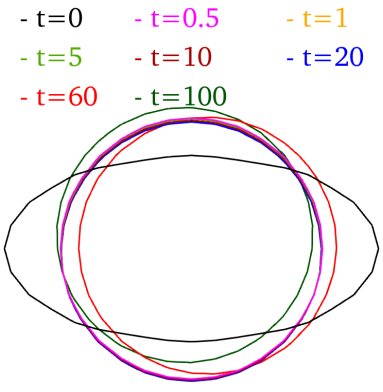

(e) $\sigma = 100$

Figure 5.21: Bubble evolution for different values of surface tension constant ($\sigma = 1$, 10, 25, 50, and 100), at mesh refinement $h = 1/32$.

5.2.3 Capillary Time Restriction

Analogous to the static bubble case, a capillary time restriction study is also conducted for the oscillating bubble. Using the chosen parameters ($\rho = 1$, $\sigma = 1$, $h = 1/32$), the capillary time step is estimated as $\Delta t^{\text{cap}} = 0.0055$. In the present simulations, however, a much larger time step of $\Delta t = 1e-1$ is employed, which exceeds the capillary restriction by almost a factor of 19. For comparison, the reference study of Hysing [72] is considered, where the selected time step is $\Delta t = 5$, while the corresponding capillary time for the refinement level 5 is $\Delta t^{\text{cap}} = 0.17$. Importantly, the Hysing benchmark relies on the classical CSF method, whereas the present work employs the curvature free CSS formulation.

The comparative results, shown in Figs. 5.22 and 5.23, highlight a clear distinction between the two approaches. In the CSF framework, the violation of the capillary condition leads to numerical instabilities and severe interface distortions, as expected. In contrast, the current CSS formulation delivers stable and accurate results throughout the entire simulation, despite the deliberate choice of a time step far beyond the capillary restriction. The oscillating ellipse successfully relaxes to a circular steady state without any spurious interface deformation. This confirms that the implicit treatment of surface tension in the CSS methodology effectively removes the capillary time step constraint, providing both stability and accuracy without requiring additional stabilization mechanisms.

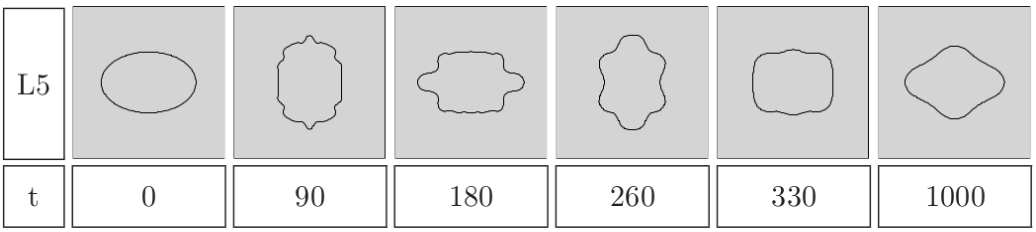

Figure 5.22: Bubble evolution [72] for the standard explicit CSF method.

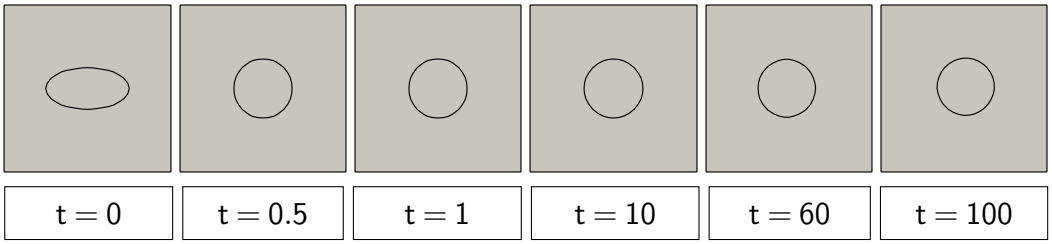

Figure 5.23: Bubble evolution for the CSS formulation with $\Delta t = 1e-1$, at mesh refinement $h = 1/32$.

5.3 Rising Bubble

The rising bubble [28] is a widely used problem for multiphase flow solvers. It considers two immiscible fluids with different densities and viscosities confined in a two-dimensional rectangular domain $\Omega = (0,1) \times (0,2)$, separated by an interface Γ. The lighter fluid Ω_2 forms a bubble of radius $r = 0.2$, initially placed at the center $c = (0.5, 0.5)$ inside the heavier surrounding fluid Ω_1, illustrated in Fig. 5.24. Boundary conditions are imposed such that no-slip ($\mathbf{u} = 0$) holds at the top and bottom walls, while free-slip condition is applied at the vertical boundaries. The physical parameters for both fluids are summarized in Table 5.3.

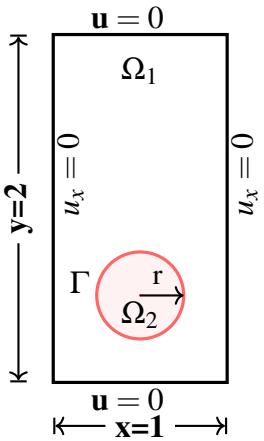

Figure 5.24: Configuration for the rising bubble test.

ρ_1	ρ_2	μ_1	μ_2	g	σ
10^4	10^3	1	1	-8 $\times 10^{-4}$	0.5

Table 5.3: The physical parameters for the rising bubble test.

According to the theoretical and experimental studies reported in Clift et al. [97], the expected long time behavior of the bubble is that it deforms and evolves towards an ellipsoidal equilibrium shape as it rises under buoyancy. The objective of the present study is to assess the capability of the proposed curvature free material cut-off formulation in handling this more challenging two-phase flow configuration, while remaining free from the classical capillary time step restriction.

For a two-phase immiscible system, the capillary time restriction is defined as:

$$\Delta t_h^{\text{cap}} = \sqrt{\frac{(\rho_1 + \rho_2) h^3}{4\pi\sigma}}, \tag{5.3.1}$$

where ρ_1 and ρ_2 denote the densities of the two fluids, h is the grid spacing, and σ is the surface tension coefficient. Substituting the physical parameters for the mesh refinement $h = 1/64$ yields $\Delta t^{\text{cap}} = 0.08$.

To investigate the robustness of the method, simulations are performed with time steps $\Delta t = 0.5$ and $\Delta t = 1.0$, both are an order of magnitude larger than the capillary restriction. The comparison with the standard CSF approach, taken from Hysing [28] and shown in Fig. 5.25, highlights the well-known instability of the CSF method when the capillary time condition is violated. Consequently, the bubble interface becomes severely distorted and the numerical solution deteriorates.

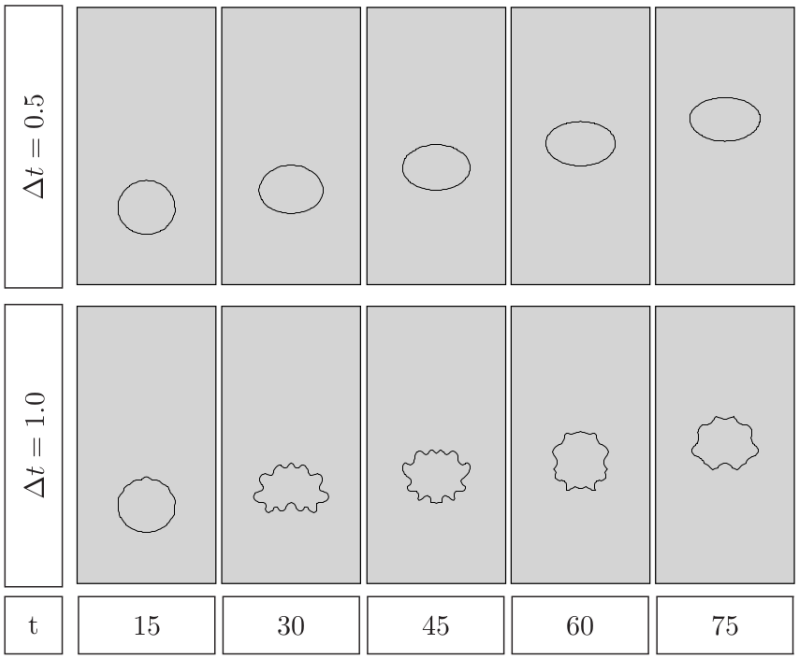

Figure 5.25: Bubble evolution [72] for the standard explicit CSF method, $\Delta t = 0.5$ and $\Delta t = 1.0$, at mesh refinement $h = 1/80$.

By contrast, the results obtained with the CSS formulation (see Fig. 5.26) remain stable and physically consistent, even at these large time steps. The bubble evolves smoothly, maintaining its interface integrity and exhibiting the expected ellipsoidal deformation without artificial distortions. This demonstrates the effectiveness of the implicit surface tension treatment inherent to the CSS methodology, which removes the restrictive capillary time step constraint and allows for accurate and stable simulations of multiphase flows at significantly larger time steps.

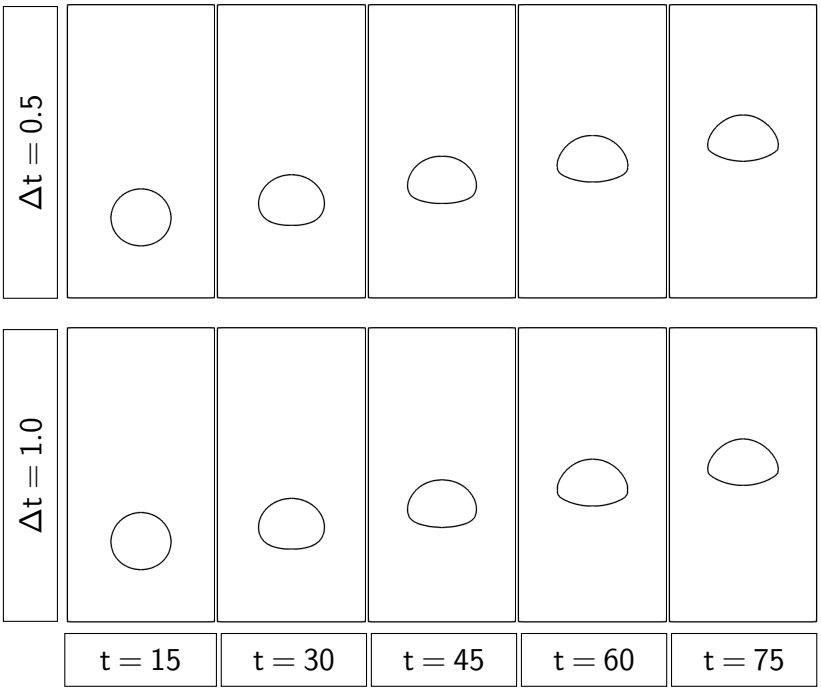

Figure 5.26: Bubble evolution for the CSS formulation with $\Delta t = 0.5$ (top) and $\Delta t = 1.0$ (bottom), at mesh refinement $h = 1/64$.

6

Rising Bubble Benchmark

In the preceding chapters, the formulation and systematic development of a monolithic solver for interfacial flow problems is presented. The robustness and accuracy of the solver is first examined through canonical multiphase flow configurations, namely the static and oscillating bubble tests [23, 98]. These preliminary studies served as essential validation steps, ensuring that the solver can reliably capture fundamental interfacial dynamics before advancing to more demanding scenarios.

In the present chapter, attention is directed towards the numerical investigation of the well-established rising bubble benchmark (test case 1 and 2) [28, 99]. This benchmark, despite its relatively simple geometric setup, is characterized by pronounced interfacial deformations and topological changes, which render it a stringent test for any multiphase flow solver. By confronting such challenges, the benchmark provides a rigorous assessment of both the accuracy and stability of the proposed methodology.

6.1 Benchmark Configuration

The classical rising bubble benchmark [28] serves as a widely accepted test case for assessing multiphase flow solvers. It considers a two-dimensional rectangular computational domain, defined as

$$\Omega = \Omega_1 \cup \Omega_2 = (0,1) \times (0,2), \tag{6.1.1}$$

occupied by two immiscible, incompressible fluids with distinct density and viscosity contrasts. The two phases are separated by a sharp interface Γ, across which discontinuities in material properties are present.

In this setup, the lighter phase Ω_2 takes the form of a circular bubble of radius $r = 0.25$, initially positioned at the point $(0.5, 0.5)$ within the domain, and is fully surrounded by the heavier fluid Ω_1, illustrated in Fig. 6.1. This configuration naturally induces buoyancy-driven motion, making it an ideal candidate for evaluating the ability of numerical methods to capture interface dynamics, deformation, and topological variations.

To complete the problem specification, appropriate boundary conditions are imposed on the domain boundaries. No-slip condition, $\mathbf{u} = 0$, is prescribed at the horizontal walls (top and bottom), ensuring zero velocity at the solid boundaries. Along the vertical walls, free-slip condition is applied, given by

$$\mathbf{u} \cdot \mathbf{n} = 0, \ \boldsymbol{\tau} \cdot \left(\nabla \mathbf{u} + (\nabla \mathbf{u})^T \right) \cdot \mathbf{n} = 0, \tag{6.1.2}$$

where $\mathbf{n}$ and τ denote the outward normal and tangential unit vectors, respectively.

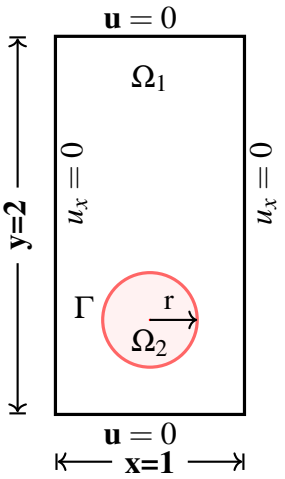

Figure 6.1: Configuration for the rising bubble benchmark.

6.2 Parameters

The material properties of both phases employed in the benchmark are summarized in Table 6.1. As the bubble ascends, the interface undergoes time-dependent deformation driven by the competing effects of inertia, viscous stresses, and surface tension forces.

In the first benchmark configuration, the ratios of density and viscosity between the two

fluids are relatively modest, leading to only moderate deformation of the bubble interface. Conversely, the second benchmark case is characterized by substantially larger density and viscosity contrasts, which amplify the imbalance between buoyancy and surface tension, thereby producing more pronounced interfacial deformations. This contrast between the two cases provides a systematic mean of assessing the robustness of numerical methods across regimes of increasing physical complexity.

The interplay between the dominant forces acting on the bubble can be quantified in terms of dimensionless numbers, namely the Reynolds and Eötvös numbers. The Reynolds number

$$Re = \frac{\rho_1 \sqrt{g}(2r)^{3/2}}{\mu_1}, \tag{6.2.1}$$

represents the ratio of inertial to viscous forces, while the Eötvös number

$$Eo = 4\rho_1 g r^2/\sigma, \tag{6.2.2}$$

measures the relative importance of buoyancy forces compared to surface tension. Here, ρ_1 and μ_1 denote the density and viscosity of the surrounding fluid Ω_1, g is the gravitational acceleration, r is the bubble radius, and σ is the surface tension coefficient. Together, these non-dimensional parameters provide a compact characterization of the flow regime and are commonly used for benchmarking interfacial flow solvers.

Test case	ρ_1	ρ_2	μ_1	μ_2	g	σ	Re	Eo	ρ_1/ρ_2	μ_1/μ_2
1	1000	100	10	1	0.98	24.5	35	10	10	10
2	1000	1	10	0.1	0.98	1.96	35	125	1000	100

Table 6.1: Physical parameters and dimensionless numbers of the test cases.

6.3 Benchmark Quantities

To rigorously assess the accuracy of the proposed formulation (2.6.3) against the established benchmark, a set of quantitative and qualitative measures are evaluated. The primary diagnostic quantities include the bubble rise velocity, center of mass, and circularity. In addition, the temporal evolution of the bubble interface is monitored and compared with the reference data provided by the TP2D (Transport Phenomena in Two Dimensions) [28]. These measures collectively provide a comprehensive validation framework,

capturing both the kinematic and geometric characteristics of the rising bubble.

The rise velocity [100] characterizes the average vertical motion of the lighter phase Ω_2 as it ascends through the surrounding fluid, obtained by averaging the velocity field over the bubble volume

$$\mathcal{U}_b = \frac{\int_{\Omega_2} \mathbf{u} dx}{\int_{\Omega_2} 1 dx}. \tag{6.3.1}$$

This provides direct insight into the balance between buoyancy-driven acceleration and viscous resistance.

The trajectory of the bubble is tracked via the evolution of the center of mass (or centroid) [101, 102, 103, 104]. At each time step, the centroid coordinates (x_c, y_c) are computed as

$$X_c = (x_c, y_c) = \frac{\int_{\Omega_2} \mathbf{x} dx}{\int_{\Omega_2} 1 dx}. \tag{6.3.2}$$

Monitoring the centroid allows for quantifying both the vertical displacement and any potential lateral migration of the bubble. While local geometric markers (e.g. the uppermost or lowermost points) can provide approximate positions, the centroid offers a more robust global measure of bubble motion.

Circularity [105] serves as a non-dimensional measure of bubble deformation, defined as the ratio between the perimeter of a circle with the equivalent diameter d_a and the actual perimeter P_b of the bubble

$$\phi = \frac{P_a}{P_b} = \frac{\pi d_a}{P_b}. \tag{6.3.3}$$

Here, a value of $\phi = 1$ corresponds to a perfectly circular bubble, while deviations below unity indicate change in the shape due to interfacial forces. This parameter is particularly useful for characterizing the degree of elongation or flattening of the bubble shape over time.

In addition to these scalar quantities, the instantaneous bubble morphology is recorded throughout the simulation. Visualization of the bubble contour enables a qualitative comparison with benchmark results and provides further validation of the solver's ability to capture complex interfacial dynamics.

6.4 Error Analysis and Convergence Assessment

To quantitatively evaluate the accuracy of the proposed formulation, error are computed by comparing the numerically obtained quantities with the reference benchmark data. The discrepancies are characterized using standard vector norms, namely the l_1, l_2, and l_∞ norms, which provide complementary perspectives on the error distribution in time. Specifically, the temporal errors are defined as

$$\|e\|_1 = \frac{\sum_{t=1}^{N} \left| q_{t,\mathrm{ref}} - q_t \right|}{\sum_{t=1}^{N} \left| q_{t,\mathrm{ref}} \right|}, \tag{6.4.1}$$

$$\|e\|_2 = \left(\frac{\sum_{t=1}^{N} \left| q_{t,\mathrm{ref}} - q_t \right|^2}{\sum_{t=1}^{N} \left| q_{t,\mathrm{ref}} \right|^2} \right)^{1/2}, \tag{6.4.2}$$

$$\|e\|_\infty = \frac{\max_t \left| q_{t,\mathrm{ref}} - q_t \right|}{\max_t \left| q_{t,\mathrm{ref}} \right|}, \tag{6.4.3}$$

where $\|e\|_1$, $\|e\|_2$, and $\|e\|_\infty$ denote the normalized l_1-, l_2-, and l_∞-error norms, respectively. Here, q_t represents the computed value of the diagnostic quantity (such as rise velocity, centroid, circularity) at time t, while $q_{t,\mathrm{ref}}$ denotes the corresponding reference solution. The total number of temporal sampling points is given by $N = \big((t_{\max} - t_1)/\Delta t\big) + 1$.

The different norms highlight distinct aspects of the error

- The l_1-norm provides a measure of the *average relative deviation* accumulated over time.
- The l_2-norm emphasizes the *root-mean-square error*, giving higher weight to larger deviations.
- The l_∞-norm quantifies the *maximum pointwise discrepancy*, which is critical for identifying extreme local deviations from the reference solution.

In addition to absolute error quantification, the estimated order of convergence (EOC) is evaluated to determine the asymptotic rate at which the numerical error decreases under spatial refinement. For two successive mesh resolutions h_{i-1} and h_i, the EOC is computed as

$$EOC = \frac{log(\|e_{i-1}\| / \|e_i\|)}{log(h_{i-1}/h_i)}, \tag{6.4.4}$$

this convergence indicator is calculated for all key benchmark quantities, namely the bubble rise velocity, center of mass, and circularity, thereby providing a systematic verification of the solver's accuracy and consistency with theoretical expectations.

6.5 Test Case 1

To ensure the reliability and accuracy of the numerical solver, it is crucial to identify the optimal set of governing numerical parameters that influence the interface dynamics and overall solution quality. These parameters include the magnitude of compression γ_1, diffusion γ_2, interface thickness ϵ, and time step size Δt. A series of parametric studies are conducted to examine their individual and collective effects on the accuracy.

The investigations are performed on structured meshes with resolutions 32×64 ($h = 1/32$), 64×128 ($h = 1/64$), and 128×256 ($h = 1/128$), ensuring consistent assessment of mesh-dependent behavior. The following sections present a detailed analysis of each parameter, beginning with the influence of the reinitialization terms governed by γ_1 and γ_2.

6.5.1 Compression and diffusion parameters

In the system of equations (2.6.3), the compression and the diffusion parameters, γ_1 and γ_2, are inherently sensitive and exert a significant influence on the accuracy of interface capturing, conservation of mass, and the overall convergence behavior of the scheme.

At present, the literature does not provide explicit guidelines or systematic investigations regarding the appropriate choice of these parameters. Motivated by this gap, the present work undertakes a detailed study aimed at exploring the optimal range of γ_1 and γ_2. The study is performed under fixed numerical conditions, namely a uniform mesh refinement of $h = 1/64$, time step size $\Delta t = 5e-3$ and an interface thickness $\epsilon = 0.010$ ($0.6h$).

The structure of this study involves configuring multiple combinations of γ_1 and γ_2. For each prescribed value of γ_1, three different magnitudes of γ_2 are considered. The performance of each parameter set is assessed by computing the bubble rise velocity, center of mass, circularity, and comparing them against the established reference data from TP2D [28]. The corresponding results are presented in Fig. 6.2 to Fig. 6.8, where the superimposed curves of the physical quantities highlight the influence of the compression and diffusion terms on the bubble dynamics.

In test case 1, significant morphological changes in the bubble shape (from an initially

circular configuration to an elliptical form) become evident after approximately $t = 1$. At this stage, reinitialization of the material cut-off function is necessary to avoid numerical deterioration of the interface representation. Consequently, the reinitialization terms governed by the parameters γ_1 and γ_2 are activated from $t = 1$ onwards. Following both qualitative and quantitative assessments, the numerical outcomes can be categorized into three distinct regimes.

The first block represents the upper limit of γ_1 values for which the solver fails to converge. These cases are highlighted in red color in Table 6.2. Specifically, when γ_1 is chosen as $1e-0$ or $1e-1$, the numerical scheme breaks down regardless of the selected γ_2. For most of these combinations, the simulations terminate prematurely thus the results are absent in Fig. 6.2. Only the marginal case with $\gamma_2 = 1e-2$ reaches the final simulation time. However, the predicted quantities deviate significantly from the reference results.

The second block encompasses parameter values that allow stable computations to reach the final time. This range spans from $\gamma_1 = 1e-2$ down to $\gamma_1 = 1e-20$. Within this interval, an important observation emerges: when γ_1 is relatively large (e.g. $1e-2$ or $1e-3$) and the diffusion parameter γ_2 is comparable or larger ($\gamma_2 \geq \gamma_1$), the solver suffers from stability issues. In such cases, the bubble gradually shrinks and ultimately vanishes due to excessive diffusion. Despite this, most combinations within this block yield meaningful results, as illustrated in Figs. 6.4, 6.5, and 6.6.

Among all tested configurations, the most accurate agreement with the benchmark data, both qualitatively and quantitatively is obtained for $\gamma_1 = 1e-4$ and $\gamma_2 = 1e-5$. These optimal results are presented in Fig. 6.4 (a), (c), and (e). The associated quantitative comparison (Table 6.2) confirms excellent consistency with the reference solution. It should be emphasized, however, that this optimal parameter set is specific to the present benchmark (test case 1) with its chosen discretization parameters (mesh size h, interface thickness ϵ, and time step Δt). For different numerical resolutions, the optimal values may shift. Nevertheless, the deviation is not expected to be drastic and the present findings provide a practical guideline for selecting robust parameter ranges.

The third block corresponds to the lower limit of the values, also highlighted in red color in Table 6.2. The breakdown in this block is primarily attributed to the absence of γ_1 and very large value of γ_2, preventing the computation from reaching the final time.

To further probe the influence of minimal parameter magnitudes, two special set of values are tested in which one parameter is set to a very small value while the other is completely switched off, as shown in Table 6.3. In the first part of the table, it is interesting to note that the solver remains numerically stable and convergent even under these limiting conditions. This behavior can be attributed to the presence of a sufficient value of diffusion

parameter γ_2, which effectively stabilizes the solution when the interface thickness is very small. Conversely, for cases involving a relatively diffuse interface, the inclusion of the compression term governed by γ_1 becomes essential to maintain interface sharpness and prevent excessive smearing. In the second part, the solver fails to converge because of the absence of γ_2: the compressive flux gets strong as compared to the diffusion, which might over-sharpen the interface and leads to the point of numerical oscillations or even spurious break-up of the bubble. It is also noteworthy that the inclusion of the reinitialization terms does not adversely impact the overall computational efficiency of the solver, as the number of non-linear iterations remains effectively unchanged.

On the contrary, these terms contribute to enhanced numerical robustness, facilitating faster convergence, particularly in regimes where strong non-linearities (e.g. too sharp interface) dominate the flow dynamics.

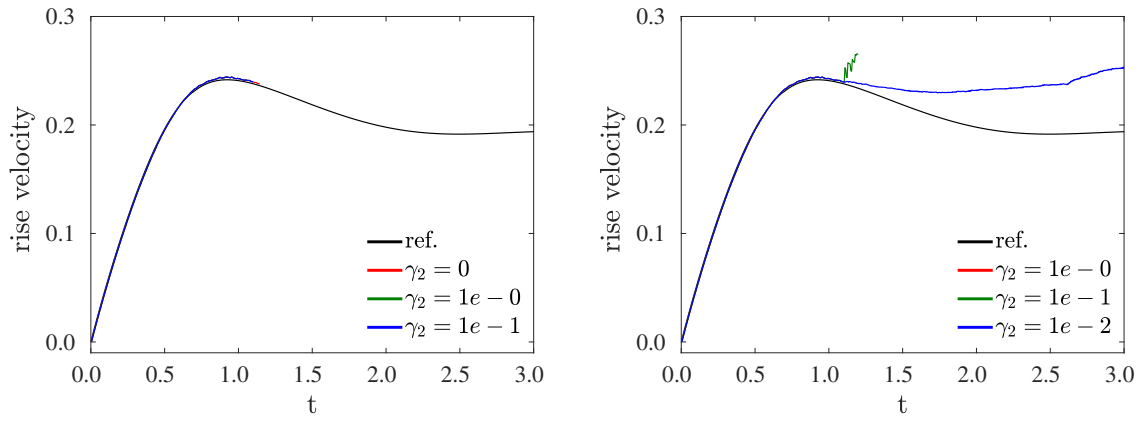

(a) $\gamma_1 = 1e-0$ **(b)** $\gamma_1 = 1e-1$

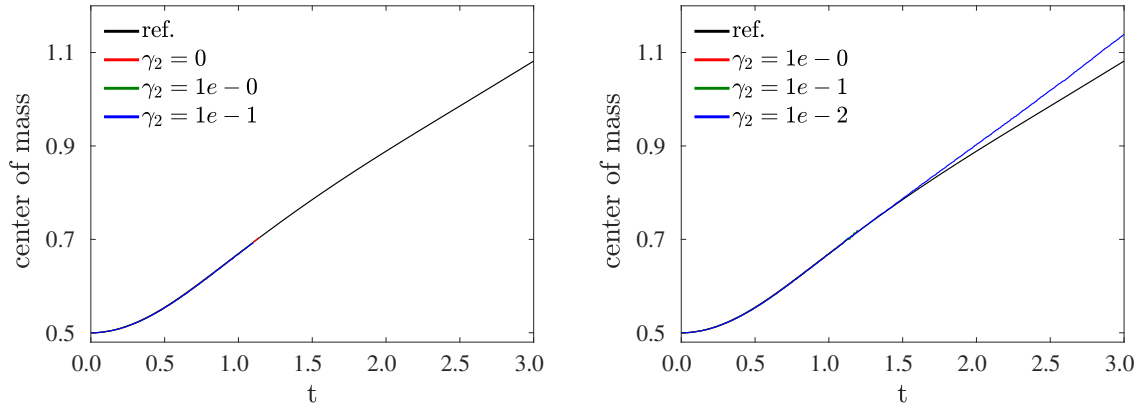

(c) $\gamma_1 = 1e-0$ **(d)** $\gamma_1 = 1e-1$

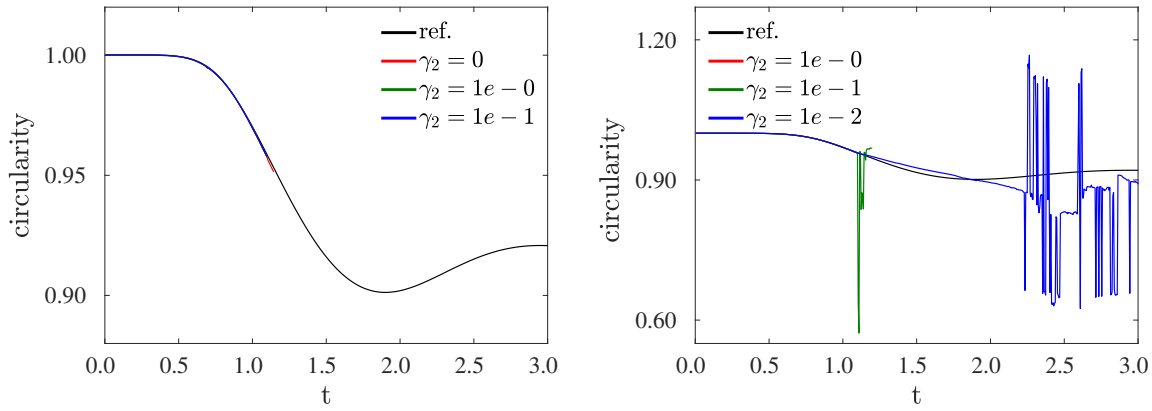

(e) $\gamma_1 = 1e-0$ **(f)** $\gamma_1 = 1e-1$

Figure 6.2: The bubble rise velocity, center of mass, and circularity for different combinations of γ_1 and γ_2, mesh refinement $h = 1/64$, interface thickness $\epsilon = 0.010$ $(0.6h)$.

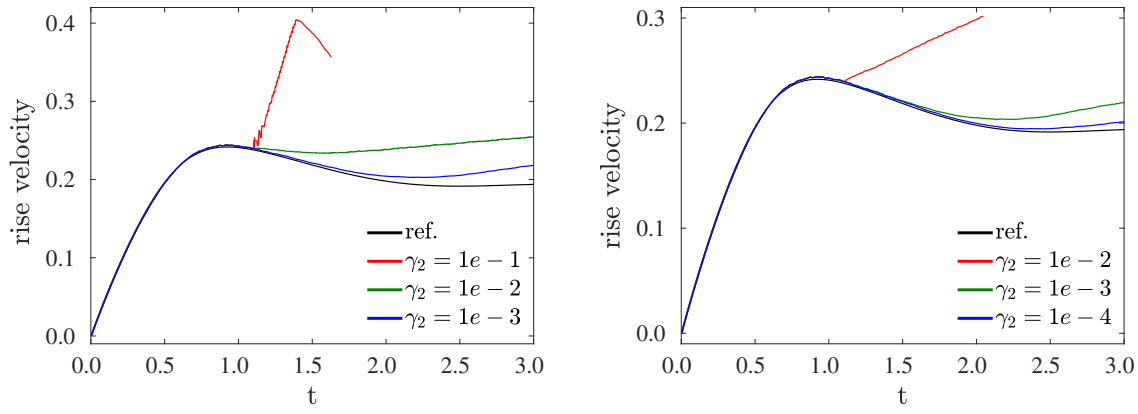

(a) $\gamma_1 = 1e-2$

(b) $\gamma_1 = 1e-3$

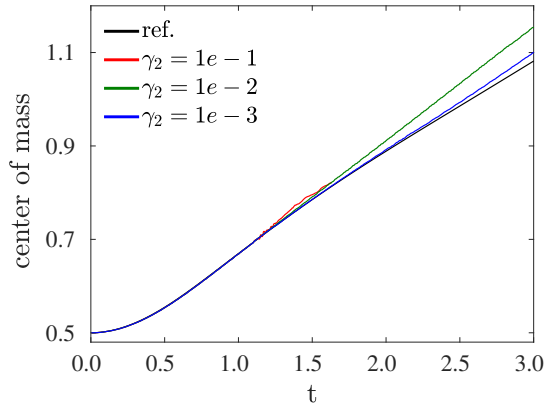

(c) $\gamma_1 = 1e-2$

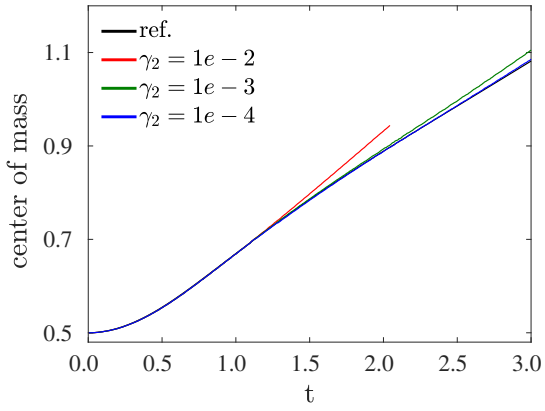

(d) $\gamma_1 = 1e-3$

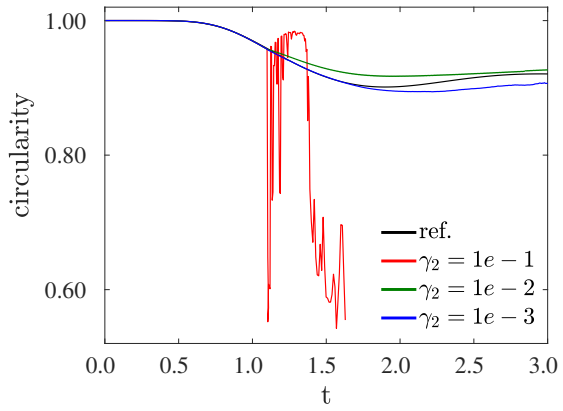

(e) $\gamma_1 = 1e-2$

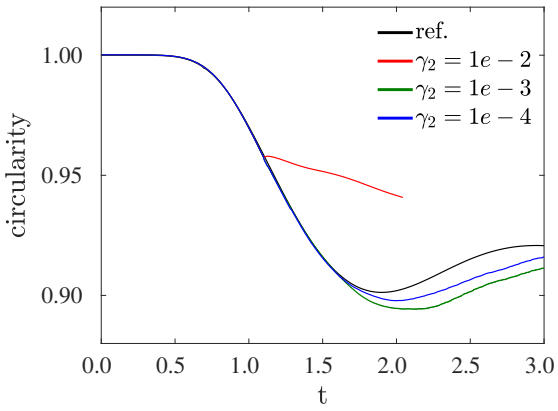

(f) $\gamma_1 = 1e-3$

Figure 6.3: The bubble rise velocity, center of mass, and circularity for different combinations of γ_1 and γ_2, mesh refinement $h = 1/64$, interface thickness $\epsilon = 0.010$ $(0.6h)$.

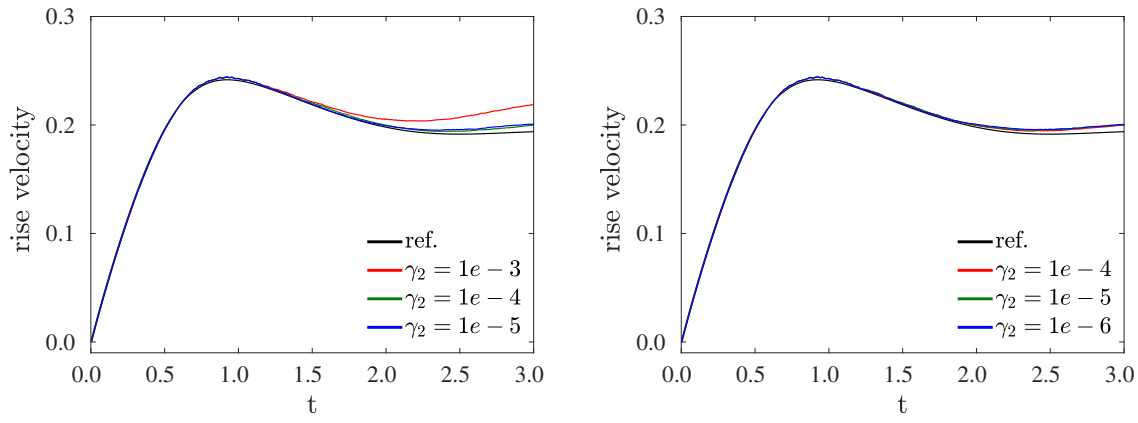

(a) $\gamma_1 = 1e-4$ **(b)** $\gamma_1 = 1e-5$

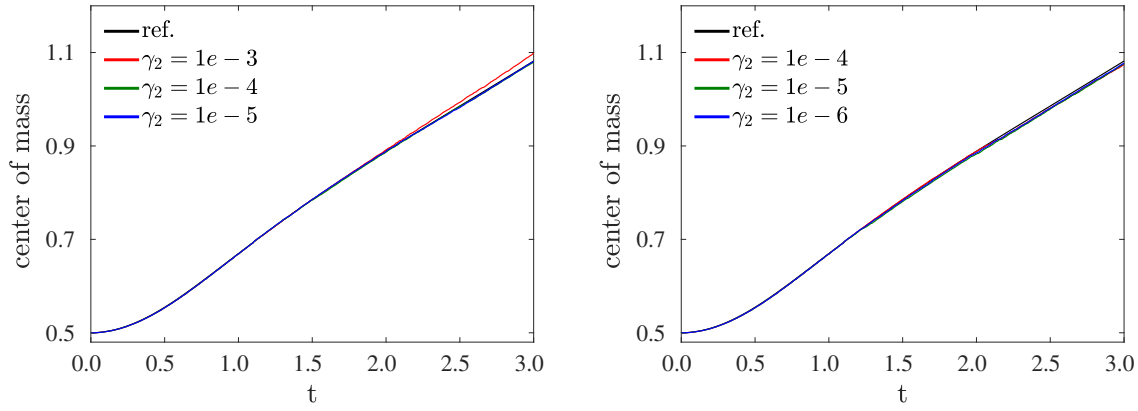

(c) $\gamma_1 = 1e-4$ **(d)** $\gamma_1 = 1e-5$

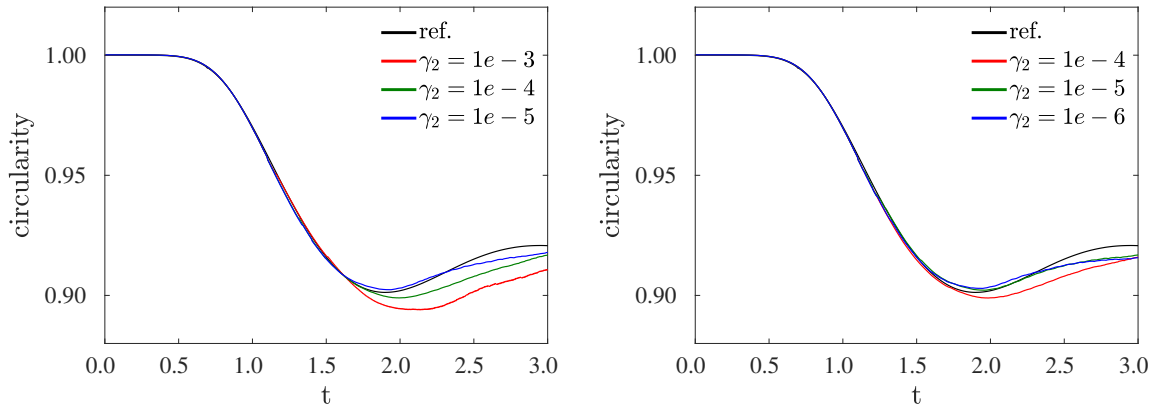

(e) $\gamma_1 = 1e-4$ **(f)** $\gamma_1 = 1e-5$

Figure 6.4: The bubble rise velocity, center of mass, and circularity for different combinations of γ_1 and γ_2, mesh refinement $h = 1/64$, interface thickness $\epsilon = 0.010$ $(0.6h)$.

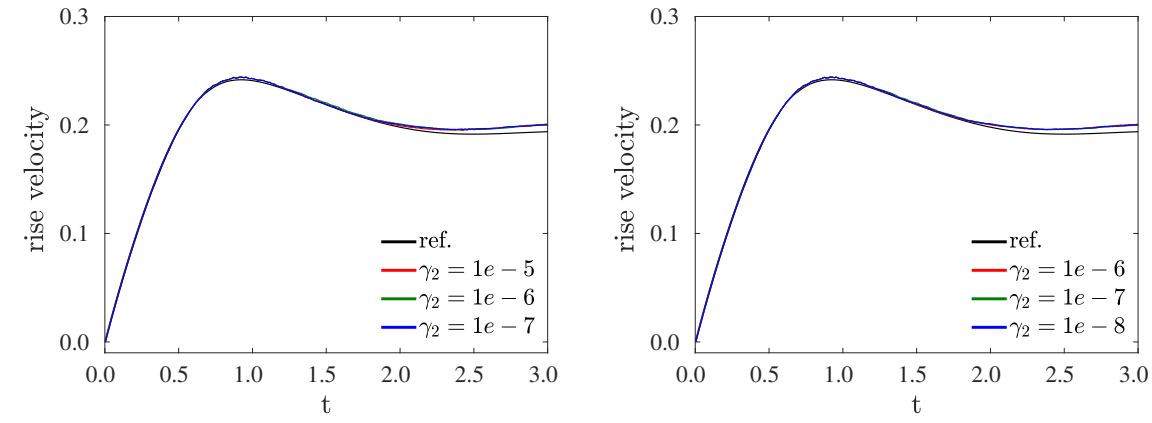

(a) $\gamma_1 = 1e-6$

(b) $\gamma_1 = 1e-7$

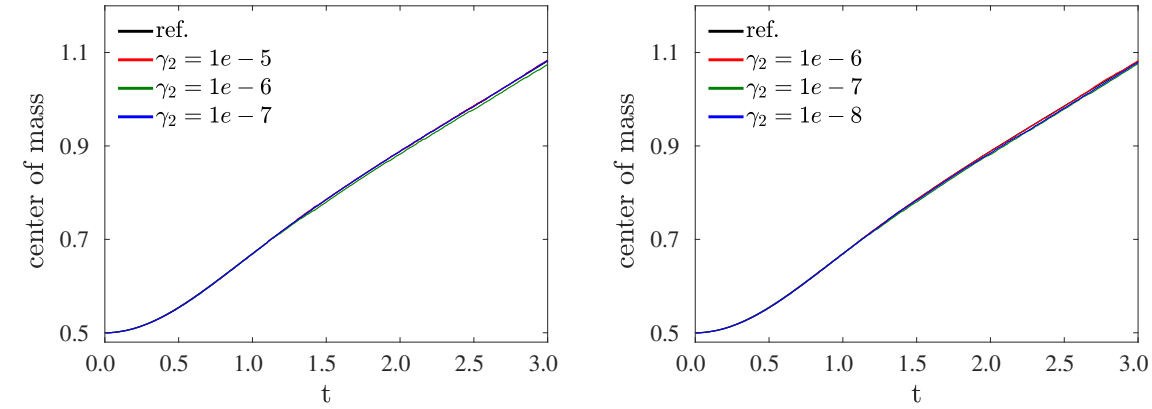

(c) $\gamma_1 = 1e-6$

(d) $\gamma_1 = 1e-7$

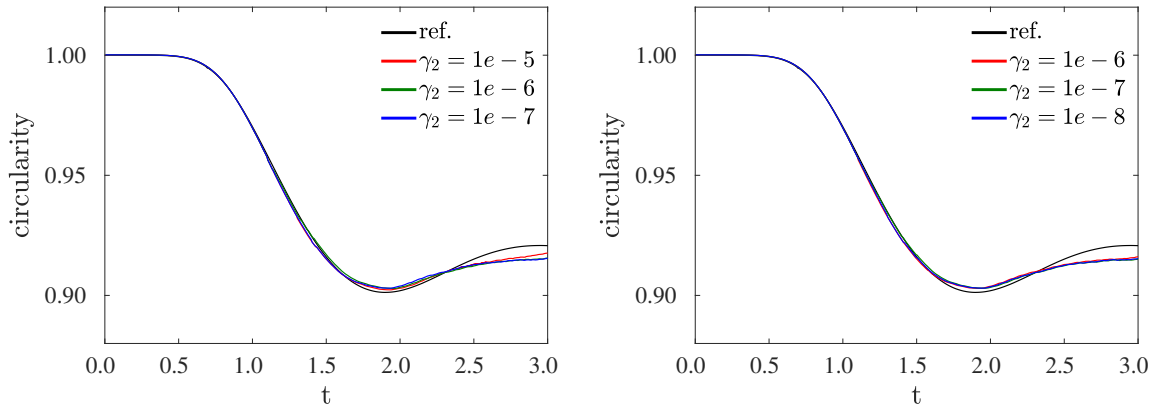

(e) $\gamma_1 = 1e-6$

(f) $\gamma_1 = 1e-7$

Figure 6.5: The bubble rise velocity, center of mass, and circularity for different combinations of γ_1 and γ_2, mesh refinement $h = 1/64$, interface thickness $\epsilon = 0.010$ $(0.6h)$.

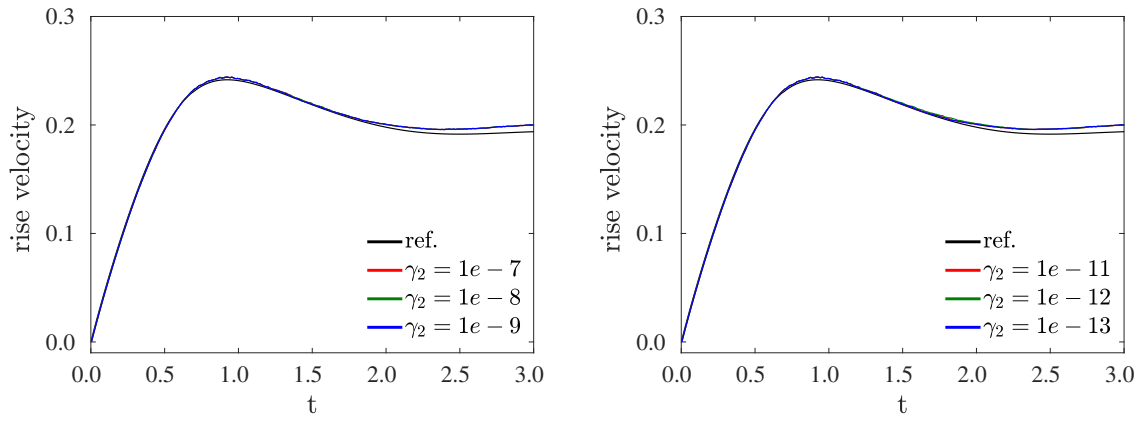

(a) $\gamma_1 = 1e-8$ **(b)** $\gamma_1 = 1e-12$

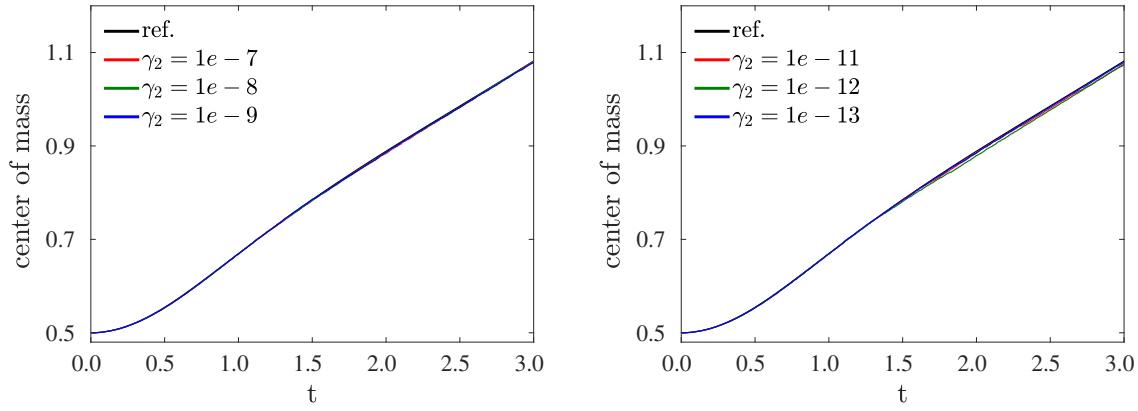

(c) $\gamma_1 = 1e-8$ **(d)** $\gamma_1 = 1e-12$

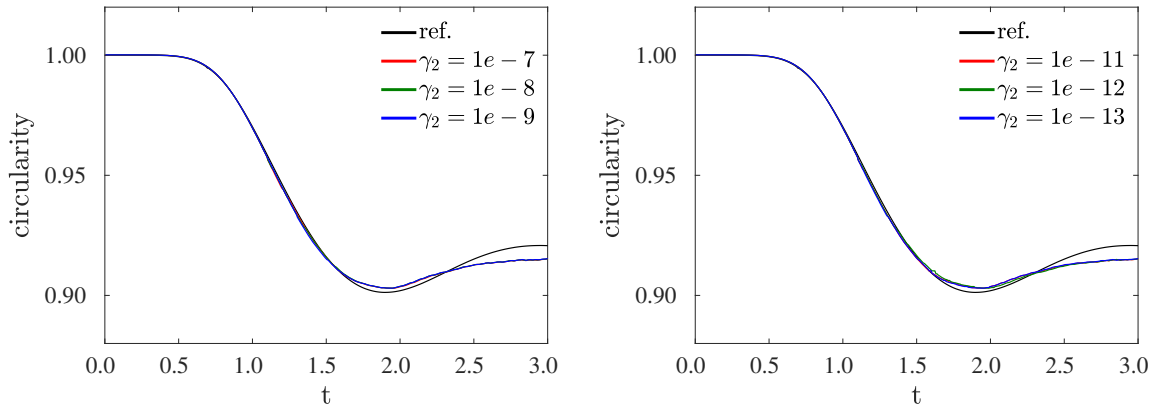

(e) $\gamma_1 = 1e-8$ **(f)** $\gamma_1 = 1e-12$

Figure 6.6: The bubble rise velocity, center of mass, and circularity for different combinations of γ_1 and γ_2, mesh refinement $h = 1/64$, interface thickness $\epsilon = 0.010$ $(0.6h)$.

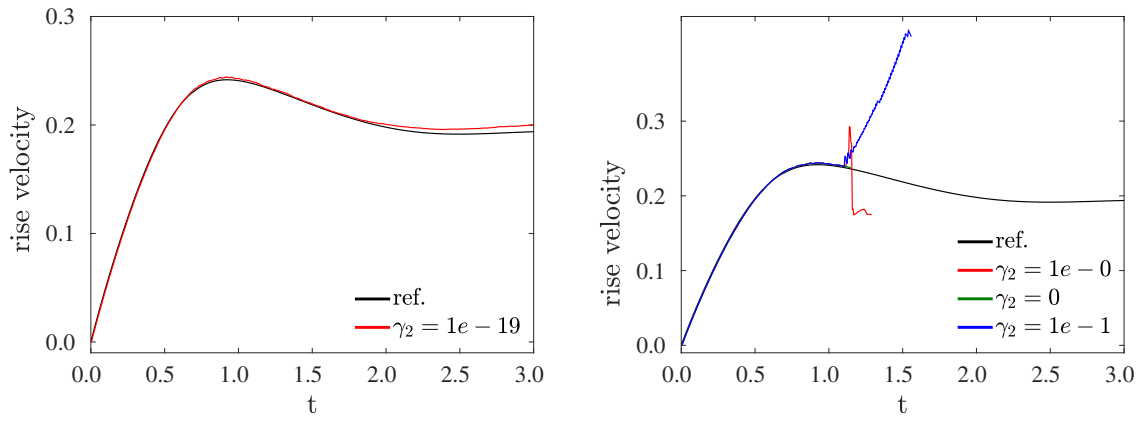

(a) $\gamma_1 = 1e-20$

(b) $\gamma_1 = 0$

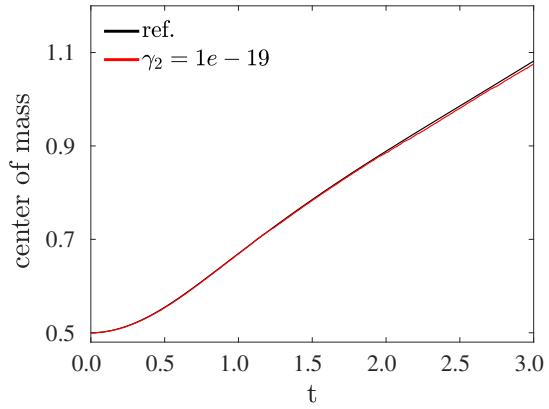

(c) $\gamma_1 = 1e-20$

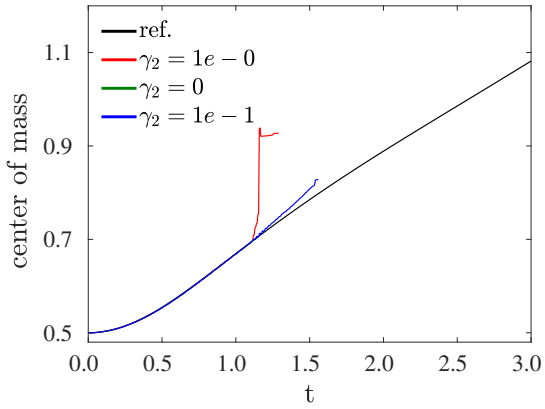

(d) $\gamma_1 = 0$

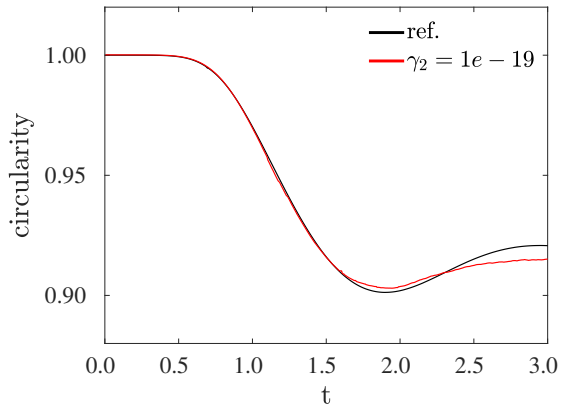

(e) $\gamma_1 = 1e-20$

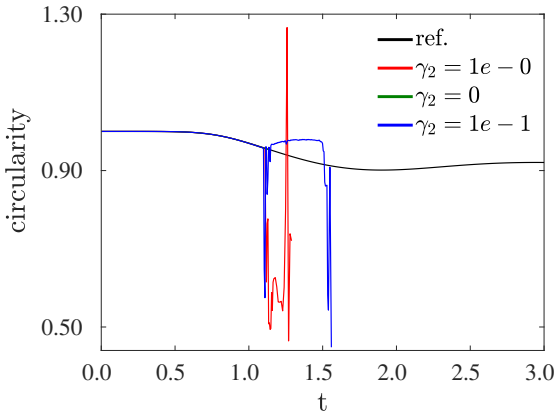

(f) $\gamma_1 = 0$

Figure 6.7: The bubble rise velocity, center of mass, and circularity for different combinations of γ_1 and γ_2, mesh refinement $h = 1/64$, interface thickness $\epsilon = 0.010$ $(0.6h)$.

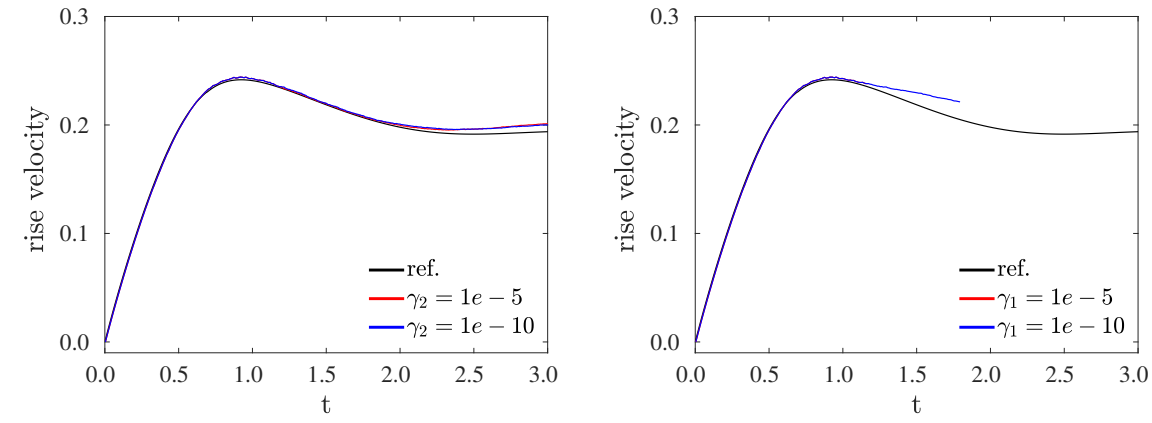

(a) $\gamma_1 = 0$ **(b)** $\gamma_2 = 0$

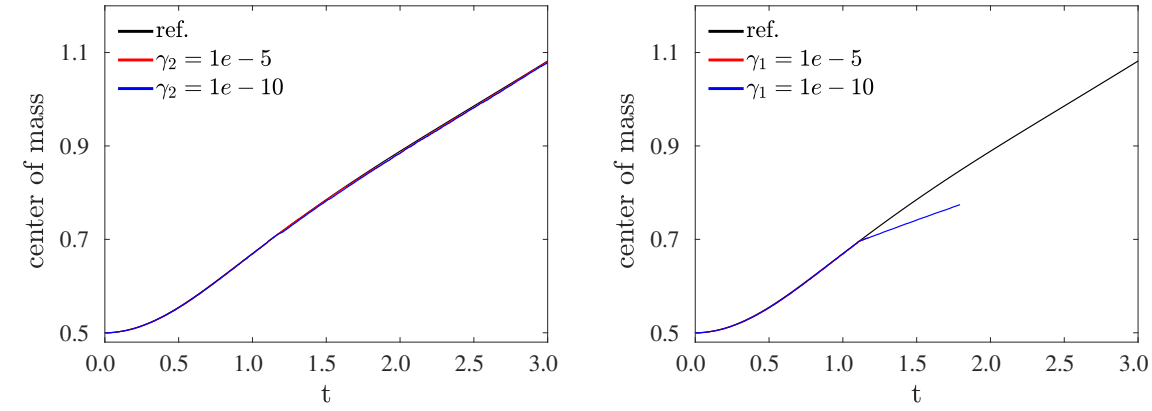

(c) $\gamma_1 = 0$ **(d)** $\gamma_2 = 0$

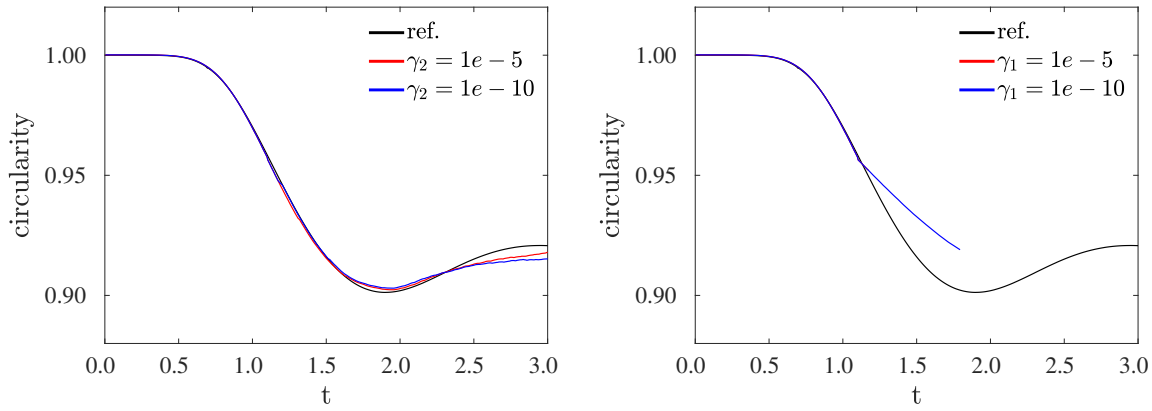

(e) $\gamma_1 = 0$ **(f)** $\gamma_2 = 0$

Figure 6.8: The bubble rise velocity, center of mass, and circularity for different combinations of γ_1 and γ_2, mesh refinement $h = 1/64$, interface thickness $\epsilon = 0.010$ $(0.6h)$.

γ_1	γ_2	$\phi_{\min}$	$t\|_{\phi=\phi_{\min}}$	$\mathbf{u}_{\max}$	$t\|_{\mathbf{u}=\mathbf{u}_{\max}}$	$X(t=3)$
$1e-0$	0	—	—	—	—	—
	$1e-0$	—	—	—	—	—
	$1e-1$	—	—	—	—	—
$1e-1$	$1e-0$	—	—	—	—	—
	$1e-1$	—	—	—	—	—
	$1e-2$	0.6246	2.610	0.2545	3.050	1.1383
$1e-2$	$1e-1$	—	—	—	—	—
	$1e-2$	0.9169	1.930	0.2554	3.050	1.1541
	$1e-3$	0.8942	2.220	0.2443	0.920	1.1004
$1e-3$	$1e-2$	—	—	—	—	—
	$1e-3$	0.8942	2.130	0.2443	0.920	1.1048
	$1e-4$	0.8978	2.000	0.2443	0.920	1.0854
$1e-4$	$1e-3$	0.8940	2.130	0.2443	0.920	1.0985
	$1e-4$	0.8990	2.000	0.2443	0.920	1.0788
	$1e-5$	0.9024	1.940	0.2443	0.920	1.0810
$1e-5$	$1e-4$	0.8989	1.990	0.2443	0.920	1.0740
	$1e-5$	0.9022	1.960	0.2443	0.920	1.0762
	$1e-6$	0.9029	1.950	0.2443	0.920	1.0767
$1e-6$	$1e-5$	0.9023	1.940	0.2443	0.920	1.0837
	$1e-6$	0.9029	1.970	0.2443	0.920	1.0741
	$1e-7$	0.9030	1.935	0.2443	0.920	1.0830
$1e-7$	$1e-6$	0.9029	1.940	0.2443	0.920	1.0818
	$1e-7$	0.9030	1.960	0.2443	0.920	1.0761
	$1e-8$	0.9030	1.955	0.2443	0.920	1.0787
$1e-8$	$1e-7$	0.9030	1.955	0.2443	0.920	1.0807
	$1e-8$	0.9030	1.950	0.2443	0.920	1.0799
	$1e-9$	0.9030	1.950	0.2443	0.920	1.0786
$1e-12$	$1e-11$	0.9030	1.955	0.2443	0.920	1.0751
	$1e-12$	0.9030	1.985	0.2443	0.920	1.0732
	$1e-13$	0.9030	1.950	0.2443	0.920	1.0786
$1e-20$	$1e-19$	0.9030	1.940	0.2443	0.920	1.0751
0	$1e-0$	—	—	—	—	—
	0	—	—	—	—	—
	$1e-1$	—	—	—	—	—
ref.		0.9013	1.9041	0.2417	0.9213	1.0813

Table 6.2: The quantitative results for different combinations of γ_1 and γ_2, mesh refinement $h = 1/64$, interface thickness $\epsilon = 0.010$ $(0.6h)$, along with the reference results (TP2D [28]).

γ_1	γ_2	$\phi_{\min}$	$t\|_{\phi=\phi_{\min}}$	$\mathbf{u}_{\max}$	$t\|_{\mathbf{u}=\mathbf{u}_{\max}}$	$X(t=3)$
0	$1e-5$	0.9024	1.960	0.2443	0.920	1.0798
	$1e-10$	0.9030	1.955	0.2443	0.920	1.0777
$1e-5$	0	—	—	—	—	—
$1e-10$	0	—	—	—	—	—
ref.		0.9013	1.9041	0.2417	0.9213	1.0813

Table 6.3: The quantitative results for different combinations of γ_1 and γ_2, mesh refinement $h = 1/64$, interface thickness $\epsilon = 0.010$ $(0.6h)$, along with the reference results (TP2D [28]).

6.5.2 Choice of interface thickness

In interface capturing methods, the interface thickness ϵ plays a significant role in the accuracy of the numerical study. A larger interface thickness results in a smoother representation of the material cut-off function. In general, the optimal relation between interface thickness and mesh is defined as $\epsilon \propto h$. Adequate resolution of the interface is essential; without a sufficient number of elements across the interface, numerical simulations may fail to produce accurate results due to under-sampling effects [95, 106].

In order to explore the suitable values of ϵ for test case 1, a range of the interface thickness values for each mesh refinement is tested, where the time step size is fixed to $\Delta t = 5e-3$, $\gamma_1 = 1e-4$ and $\gamma_2 = 1e-5$. The measured physical quantities (rise velocity, centre of mass, and circularity) are illustrated in Figs. 6.9, 6.10, and 6.11. In all figures, the obtained results are superimposed on the reference results (TP2D) [28].

For the coarser mesh with $h = 1/32$ (Fig. 6.9), the qualitative results (specifically circularity) gets closer to the reference as the ϵ gets smaller. The potential of our monolithic multiphase solver, in conjunction with the CSS formulation, is evident from the behavior of the ϵ parameter. Remarkably, even the ϵ values, smaller than the mesh size exhibit good convergence toward the reference results. Moreover, the subsequent mesh refinement $h = 1/64$ with $\epsilon = 0.010$ $(0.6h)$, as well as the finest mesh for this numerical test $h = 1/128$ with $\epsilon = 0.005$ $(0.6h)$, yield the most accurate results. These configurations demonstrate high precision across all evaluated physical quantities. This is further validated by the quantitative results presented in Table. 6.4.

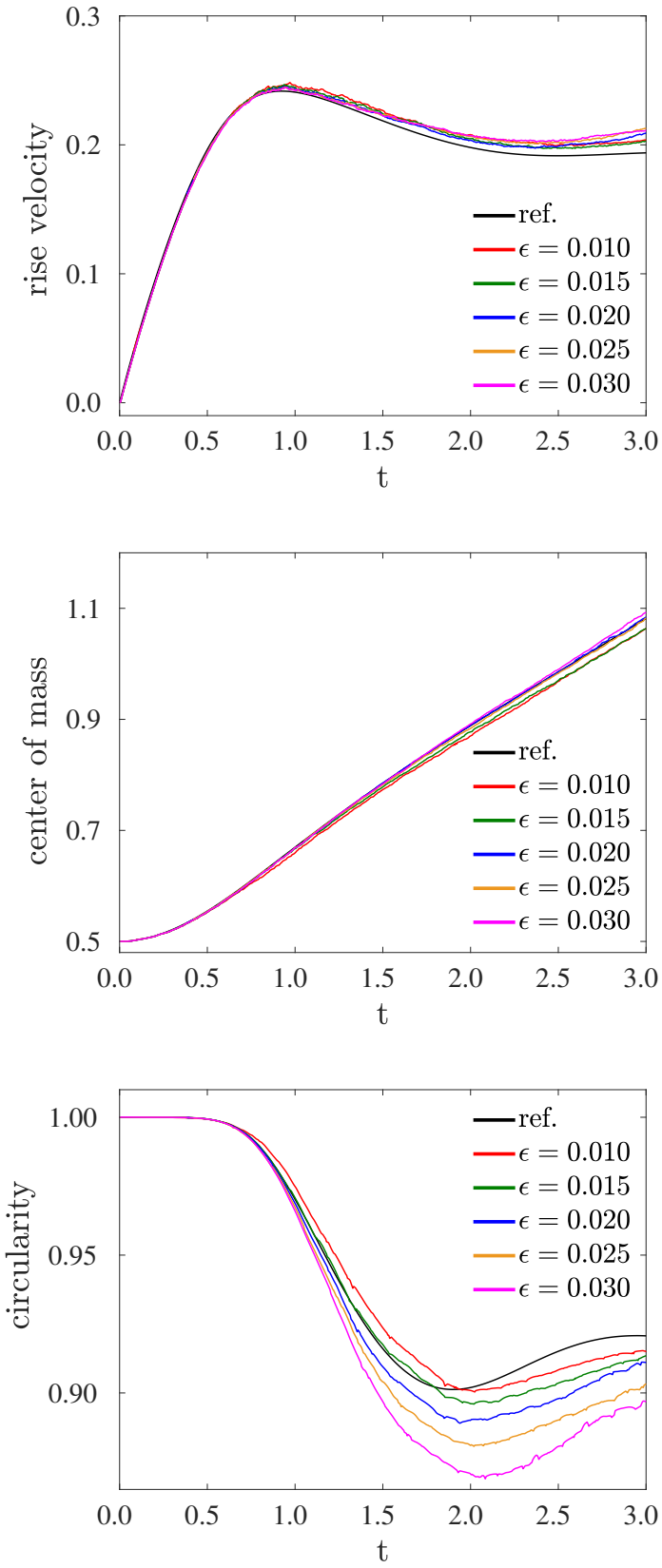

Figure 6.9: The bubble rise velocity, center of mass, and circularity for different values of ϵ, mesh refinement $h = 1/32$.

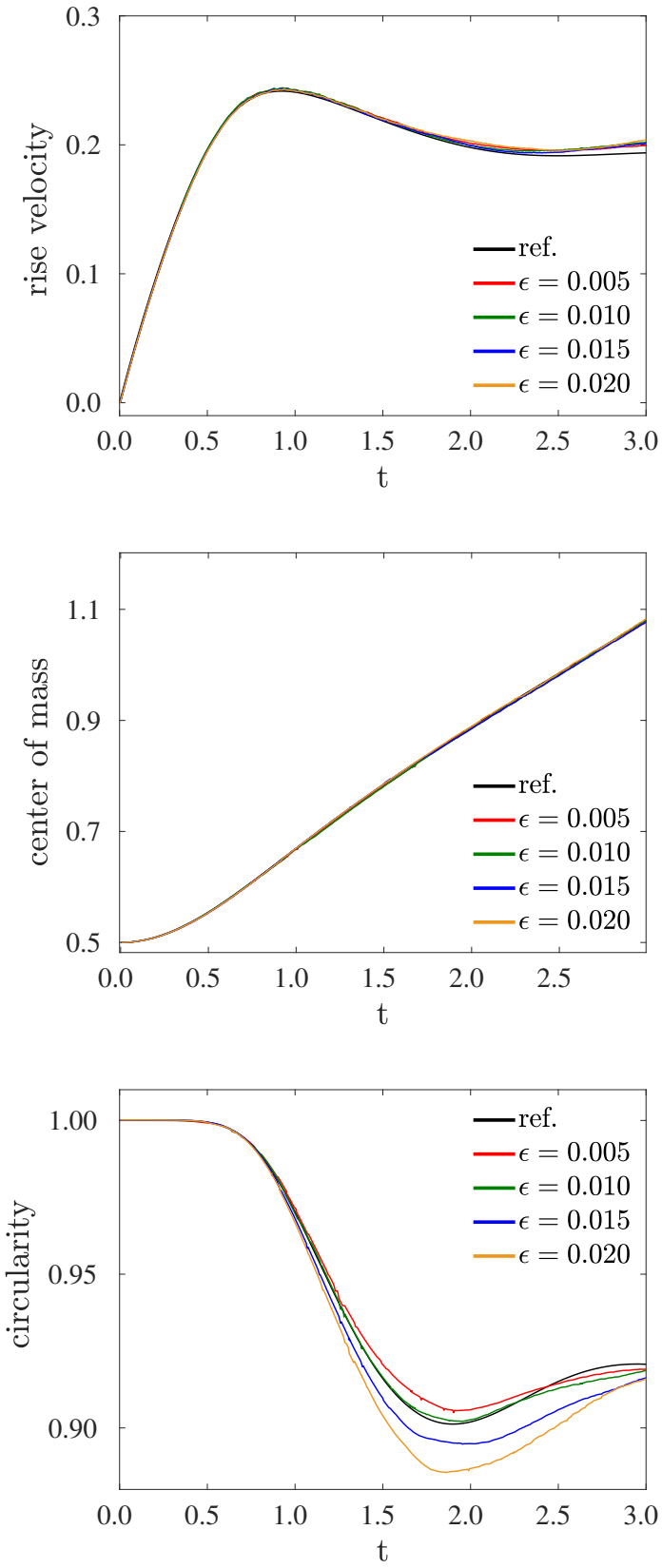

Figure 6.10: The bubble rise velocity, center of mass, and circularity for different values of ϵ, mesh refinement $h = 1/64$.

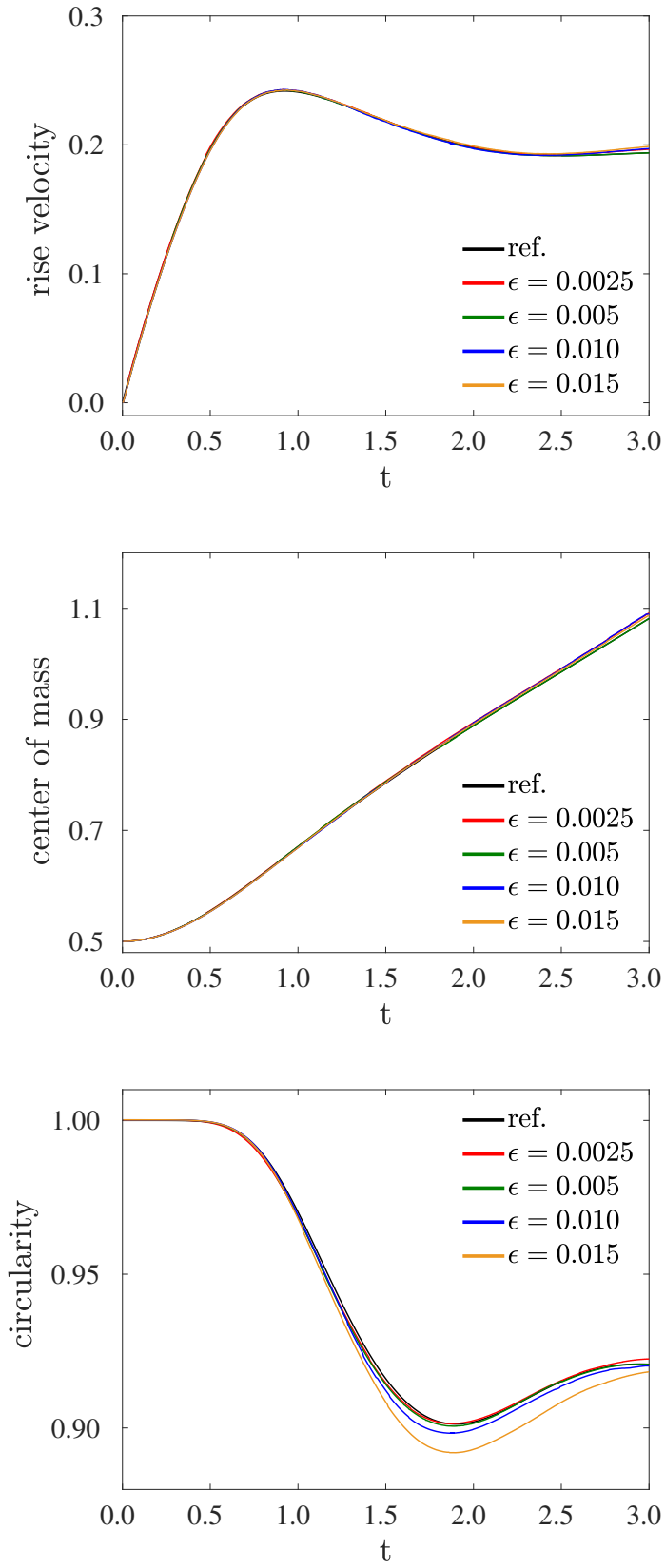

Figure 6.11: The bubble rise velocity, center of mass, and circularity for different values of ϵ, mesh refinement $h = 1/128$.

h	ϵ	$\phi_{\min}$	$t\|_{\phi=\phi_{\min}}$	$\mathbf{u}_{\max}$	$t\|_{\mathbf{u}=\mathbf{u}_{\max}}$	$X(t=3)$
1/32	0.010	0.9004	2.025	0.2483	0.970	1.0634
	0.015	0.8946	2.020	0.2468	0.940	1.0650
	0.020	0.8890	1.940	0.2453	0.940	1.0839
	0.025	0.8806	2.020	0.2449	0.945	1.0824
	0.030	0.8688	2.085	0.2445	0.945	1.0924
1/64	0.005	0.9050	1.905	0.2440	0.930	1.0777
	0.010	0.9024	1.940	0.2443	0.920	1.0810
	0.015	0.8947	1.955	0.2437	0.930	1.0782
	0.020	0.8855	1.860	0.2433	0.935	1.0835
1/128	0.0025	0.9014	1.870	0.2427	0.910	1.0913
	0.005	0.9010	1.890	0.2426	0.915	1.0815
	0.010	0.8983	1.870	0.2428	0.930	1.0895
	0.015	0.8919	1.900	0.2425	0.940	1.0865
ref.		0.9013	1.9041	0.2417	0.9213	1.0813

Table 6.4: The quantitative results for different interface thickness values with their corresponding refinement levels along with the reference results (TP2D [28]).

6.5.3 Time Step Study

In this section, we examine the impact of the time step size Δt on the performance of the numerical study. The time step size is a crucial parameter and often selected to be as small as necessary to enhance accuracy. Our analysis evaluates how effectively the chosen Δt preserves essential physical quantities ensuring consistency with the expected dynamics.

The study is performed with three time step values: $\Delta t = 5e-2$, $5e-3$, and $5e-4$, at mesh refinement $h = 1/64$. The results are presented in Fig. 6.12 and Table 6.5.

For $\Delta t = 5e-2$, the bubble rise velocity, center of mass, and circularity follow the trend of the reference solution up to $t = 1.5$. However, beyond this point, the simulation encounters challenges and the accuracy begins to deteriorate. The bubble ascends at a slower velocity compared to the reference, indicating that its position deviates from the reference and is located at a lower height.

No significant differences are observed between the results obtained using $\Delta t = 5e-3$ and $5e-4$, as both time steps closely align with the reference solution. Consequently, $\Delta t = 5e-3$ is selected for subsequent studies, as it provides accurate results while being computationally less expensive compared to $\Delta t = 5e-4$.

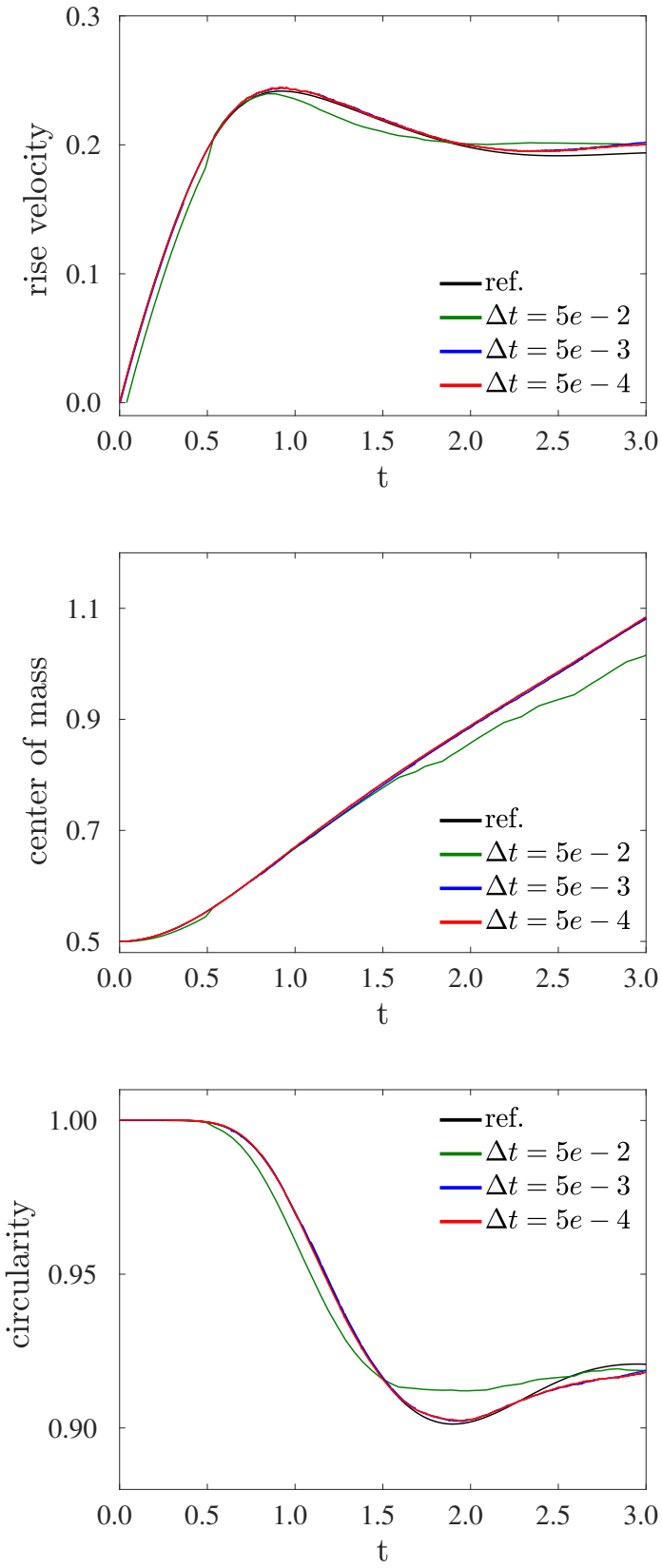

Figure 6.12: The bubble rise velocity, center of mass, and circularity for three time steps, mesh refinement $h = 1/64$, interface thickness $\epsilon = 0.010$ $(0.6h)$.

h	Δt	$\phi_{\min}$	$t\|_{\phi=\phi_{\min}}$	$\mathbf{u}_{\max}$	$t\|_{\mathbf{u}=\mathbf{u}_{\max}}$	$X(t=3)$
1/64	$5e-2$	0.9121	1.95	0.2396	0.85	1.0141
	$5e-3$	0.9024	1.940	0.2443	0.920	1.0810
	$5e-4$	0.9024	1.9470	0.2448	0.9170	1.0820
ref.		0.9013	1.9041	0.2417	0.9213	1.0813

Table 6.5: The quantitative results for three time steps, mesh refinement $h = 1/64$, interface thickness $\epsilon = 0.010$ $(0.6h)$, along with the reference results (TP2D [28]).

6.5.4 Effects of mesh refinement

The spatial discretization, represented by the mesh size h, constitutes a critical factor in multiphase flow simulations, as it governs the precision with which fluid interfaces and associated structures are resolved. Employing finer meshes generally enhances numerical accuracy by reducing spatial discretization errors and enabling the capture of delicate interfacial dynamics and small scale features.

Following the comprehensive parametric studies, the optimal parameter values are selected for validating the rising bubble benchmark (test case 1), with an appropriate interface thickness $(0.6h)$, $\Delta t = 5e-3$, $\gamma_1 = 1e-4$, and $\gamma_2 = 1e-5$.

For the coarser resolution ($h = 1/32$), the computed observables qualitatively reproduce the benchmark dynamics, but noticeable deviations emerge, particularly in the circularity beyond $t = 1.5$. As the mesh is progressively refined, the deviations from the benchmark diminish significantly. In particular, the mesh refinements $h = 1/64$ and $h = 1/128$ exhibit excellent agreement with the reference results. This improvement highlights the indispensable role of mesh refinement in faithfully reproducing the bubble dynamics and resolving fine interfacial features. All quantities (rise velocity, center of mass, and circularity) converge to the reference solution [28] as shown in Fig. 6.13.

The temporal evolution of the bubble shape is captured at seven different time intervals to track its development over time, with the final shape superimposed on the reference solution [28], illustrated in Fig. 6.14.

To gain a deeper understanding of bubble temporal evolution (given the specified parameters, outlined in Table 6.1), the bubble shapes shown in Fig. 6.14 are analyzed and classified into two distinct phases. In the first phase $0 \leq t \leq 1.5$, the initially circular bubble stretches horizontally, and a dimple forms at the bottom, within the wake region.

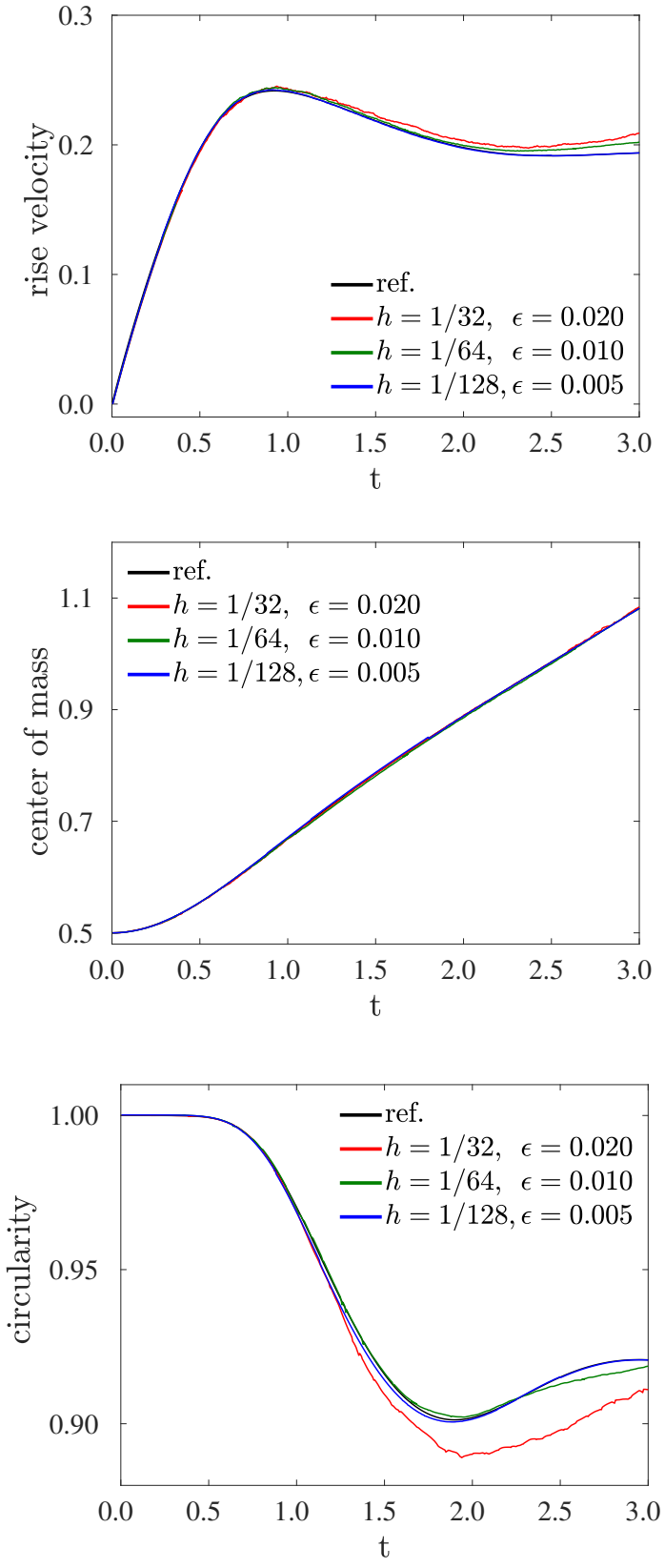

Figure 6.13: The bubble rise velocity, center of mass, and circularity for mesh refinements $h = 1/32$, $1/64$, and $1/128$.

In the second phase $1.5 \leq t \leq 3.0$, the bubble undergoes a complete transformation into an elliptical shape, consistent with experimental findings reported in [97]: The initially circular bubble, defined by the specified Reynolds (Re) and Eötvös (Eo) numbers, is expected to evolve into an elliptical shape. The Eötvös number serves as a key parameter for describing bubble shapes by quantifying the ratio of buoyancy forces to surface tension forces. In this case, the low Eötvös number indicates a dominant surface tension force, which acts along the interface to maintain the integrity of the bubble shape. Hence, with increasing the mesh refinement, a notable convergence toward the reference solution is observed, demonstrating the improved accuracy.

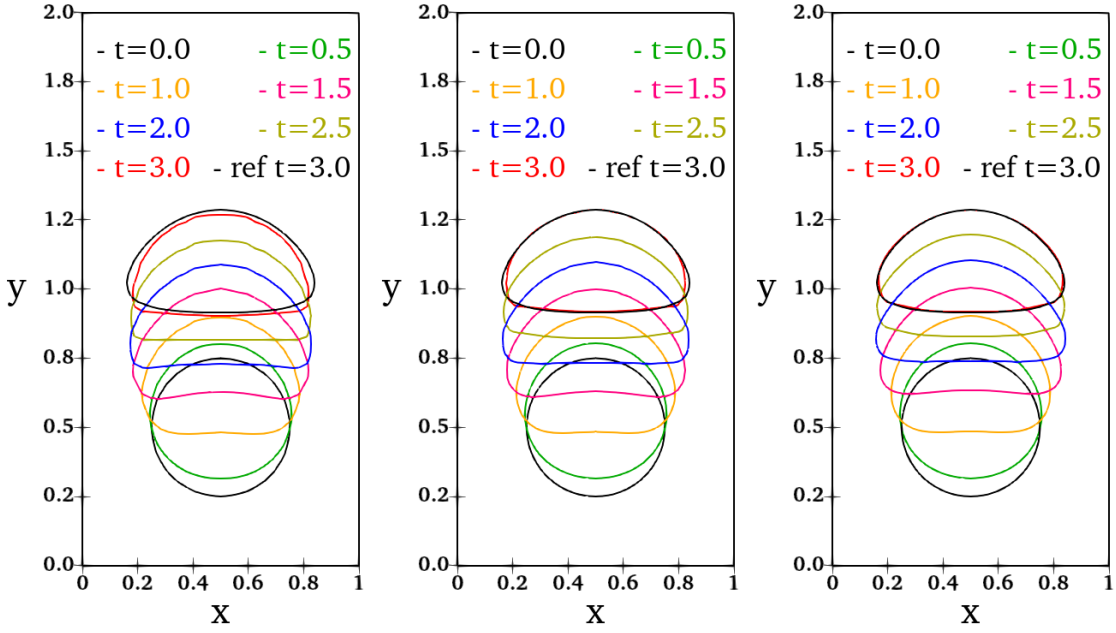

(a) $h = 1/32$ **(b)** $h = 1/64$ **(c)** $h = 1/128$

Figure 6.14: Bubble evolution at mesh refinements $h = 1/32$, $1/64$, and $1/128$, superimposed on the reference (TP2D [28]) at final time $t = 3.0$.

h	ϵ	$\phi_{\min}$	$t\|_{\phi=\phi_{\min}}$	$\mathbf{u}_{\max}$	$t\|_{\mathbf{u}=\mathbf{u}_{\max}}$	$X(t=3)$
1/32	0.020	0.8890	1.940	0.2453	0.940	1.0839
1/64	0.010	0.9024	1.940	0.2443	0.920	1.0810
1/128	0.005	0.9010	1.890	0.2426	0.915	1.0815
ref.		0.9013	1.9041	0.2417	0.9213	1.0813

Table 6.6: The quantitative results for three mesh refinements $h = 1/32$, $1/64$, and $1/128$ along with the reference results (TP2D [28]).

In addition to the qualitative and quantitative analysis, the relative error norms of the principal physical quantities are summarized in Table 6.7. The finest numerical solution of

Hysing et al. [28] is employed as the reference against which all errors and their corresponding convergence rates are evaluated. The $\|.\|_1$, $\|.\|_2$, and $\|.\|_\infty$ norms of the bubble rise velocity, center of mass, and circularity are computed for three mesh refinements, each paired with its respective optimal interface thickness $\epsilon = 0.6h$.

The results demonstrate that the estimated order of convergence (EOC) for all investigated quantities consistently falls between unity and approximately two across all considered norms.

q	h	ϵ	$\|e\|_1$	EOC_1	$\|e\|_2$	EOC_2	$\|e\|_\infty$	EOC_∞
X	1/32	0.020	0.0042		0.0051		0.0073	
	1/64	0.010	0.0022	0.9329	0.0025	1.0286	0.0036	1.0605
	1/128	0.005	0.0012	0.8745	0.0013	0.9434	0.0017	1.0825
u	1/32	0.020	0.0222		0.0279		0.0644	
	1/64	0.010	0.0109	1.0262	0.0148	0.9146	0.0350	0.8797
	1/128	0.005	0.0026	2.0677	0.0039	1.9241	0.0097	1.8513
ϕ	1/32	0.020	0.0074		0.0096		0.0170	
	1/64	0.010	0.0014	2.4021	0.0018	2.4150	0.0043	1.9831
	1/128	0.005	0.0006	1.2224	0.0008	1.0825	0.0021	1.0339

Table 6.7: The relative error norms and the estimated order of convergence for the benchmark quantities.

6.6 Test Case 2

This section is devoted to the parametric investigation of the rising bubble benchmark (test case 2), with particular emphasis on the influence of interface thickness ϵ, spatial mesh resolution h, and temporal discretization step size Δt. Unlike test case 1, this configuration is characterized by significantly larger density and viscosity contrasts between the two phases Ω_1 and Ω_2.

These pronounced material imbalance amplify the buoyancy driven motion and intensify interfacial stresses, giving rise to substantial deformations of the bubble interface. As a result, test case 2 serves as a more demanding benchmark, providing a rigorous framework for assessing the accuracy, stability, and robustness of the proposed numerical formulation under challenging multiphase flow conditions.

6.6.1 Choice of interface thickness

As highlighted in Section 6.5.2, the interface thickness parameter ϵ plays a pivotal role and directly influences the sharpness of the interface, thereby affects the accuracy of interfacial force modeling. To assess the appropriate choice of ϵ for this challenging case, a dedicated parametric investigation is carried out across three mesh refinements: $h = 1/32$, $1/64$, and $1/128$, with $\Delta t = 5e-3$, while the reinitialization parameters are chosen as $\gamma_1 = 1e-4$ and $\gamma_2 = 1e-5$. The outcomes of the present study are summarized in Table 6.8.

The influence of ϵ on the principal physical quantities is depicted in Figs. 6.15, 6.16, and 6.17. The corresponding bubble morphologies at the final time $t = 3.0$ for all resolutions and interface thickness values are illustrated in Figs. 6.18, 6.19, and 6.20, together with magnified interface views. In each case, our results are superimposed on the reference solution (TP2D [28] at mesh refinement $h = 1/640$).

For the coarser grid resolution ($h = 1/32$), the temporal evolution of the bubble dynamics already follows the qualitative trend of the benchmark solution, as shown in Fig. 6.15. Upon refinement to $h = 1/64$, noticeable improvements in accuracy and convergence are observed (Fig. 6.16). With the finest resolution ($h = 1/128$), the agreement with the reference solution becomes excellent across all investigated values of ϵ, indicating the consistency of the scheme in capturing interfacial dynamics.

The morphology of the bubble deserves further discussion owing to the characteristic formation of long, slender tails in the wake region. Previous benchmark studies have reported distinct differences in the tail structure across numerical methods: the TP2D solution features separated tail ends, while others yield connected tails of different thickness [28]. The shape of these thin structures is highly sensitive to the chosen numerical methodology [107], mesh topology (structured vs. unstructured), discretization approach (Eulerian, adaptive, hybrid), and the polynomial order of the finite element basis employed for the material cut-off function approximation (Q_1, Q_2, P_1^{disc}). A detailed comparison of different solvers and grid types has been presented in [108].

In the present simulations, the bubble shapes at $t = 3.0$ exhibit a consistent deformation pattern, characterized by upward motion and the development of elongated tails. At $h = 1/32$, five different values of ϵ are tested, and the corresponding close-up views (Fig. 6.18) reveal that no tail separation occurs. Similar behavior is observed for $h = 1/64$ (Fig. 6.19), where four different ϵ values yield tails that remain connected and free from spurious breakup. For the finest grid ($h = 1/128$), smooth and well resolved tail structures are obtained consistently across all tested interface thickness values. These results under-

line the robustness of the numerical framework, particularly in combination with CSS formulation, in accurately resolving thin interfacial structures even in regions of strong curvature.

A particularly noteworthy observation is that the solver maintains numerical stability and accuracy even when the interface thickness is chosen smaller than the mesh size. This robustness highlights the reliability of the proposed monolithic multiphase solver and confirms the suitability of the CSS based formulation for tackling challenging interfacial flow benchmarks characterized by severe deformations and strong property contrasts. The reliability of the present simulations is further supported by the quantitative assessment summarized in Table 6.8, where the computed results are compared against the reference. This comparison enables the identification of optimal interface thickness values for each mesh resolution, exhibiting excellent agreement with the benchmark solution. Consequently, these values are adopted in the subsequent numerical investigations to maintain both accuracy and consistency.

The outcomes of this study also provide an important practical guideline for parameter selection: the optimal interface thickness can be chosen as $\epsilon \approx h/2$. This proportionality strikes a balance between maintaining a sufficiently sharp interface representation and ensuring numerical stability, thereby offering a robust criterion for designing highly precise multiphase flow simulations.

h	ϵ	$\phi_{\min}$	$t\|_{\phi=\phi_{\min}}$	$\mathbf{u}_{\max,1}$	$t\|_{\mathbf{u}=\mathbf{u}_{\max,1}}$	$\mathbf{u}_{\max,2}$	$t\|_{\mathbf{u}=\mathbf{u}_{\max,2}}$	$X(t=3)$
1/32	0.010	0.5103	3.000	0.2523	0.720	0.2433	1.760	1.1210
	0.015	0.5086	3.000	0.2515	0.725	0.2424	1.850	1.1190
	0.020	0.5059	3.000	0.2514	0.725	0.2405	1.905	1.1094
	0.025	0.5098	3.000	0.2517	0.725	0.2422	1.915	1.1100
	0.030	0.5082	3.000	0.2517	0.725	0.2406	1.915	1.1102
1/64	0.005	0.5168	3.000	0.2505	0.720	0.2416	1.970	1.1245
	0.010	0.5191	3.000	0.2500	0.720	0.2392	1.955	1.1206
	0.015	0.5120	3.000	0.2500	0.720	0.2403	2.050	1.1227
	0.020	0.5157	3.000	0.2499	0.720	0.2394	1.970	1.1205
1/128	0.0025	0.5194	3.000	0.2503	0.755	0.2401	1.980	1.1354
	0.005	0.5199	3.000	0.2502	0.725	0.2407	1.970	1.1373
	0.010	0.5193	3.000	0.2501	0.750	0.2391	1.985	1.1332
	0.015	0.5191	3.000	0.2500	0.725	0.2388	2.045	1.1285
ref.		0.5869	2.4004	0.2524	0.7332	0.2434	2.0705	1.1380

Table 6.8: The quantitative results for different interface thickness values with their corresponding refinement levels along with the reference results (TP2D [28]).

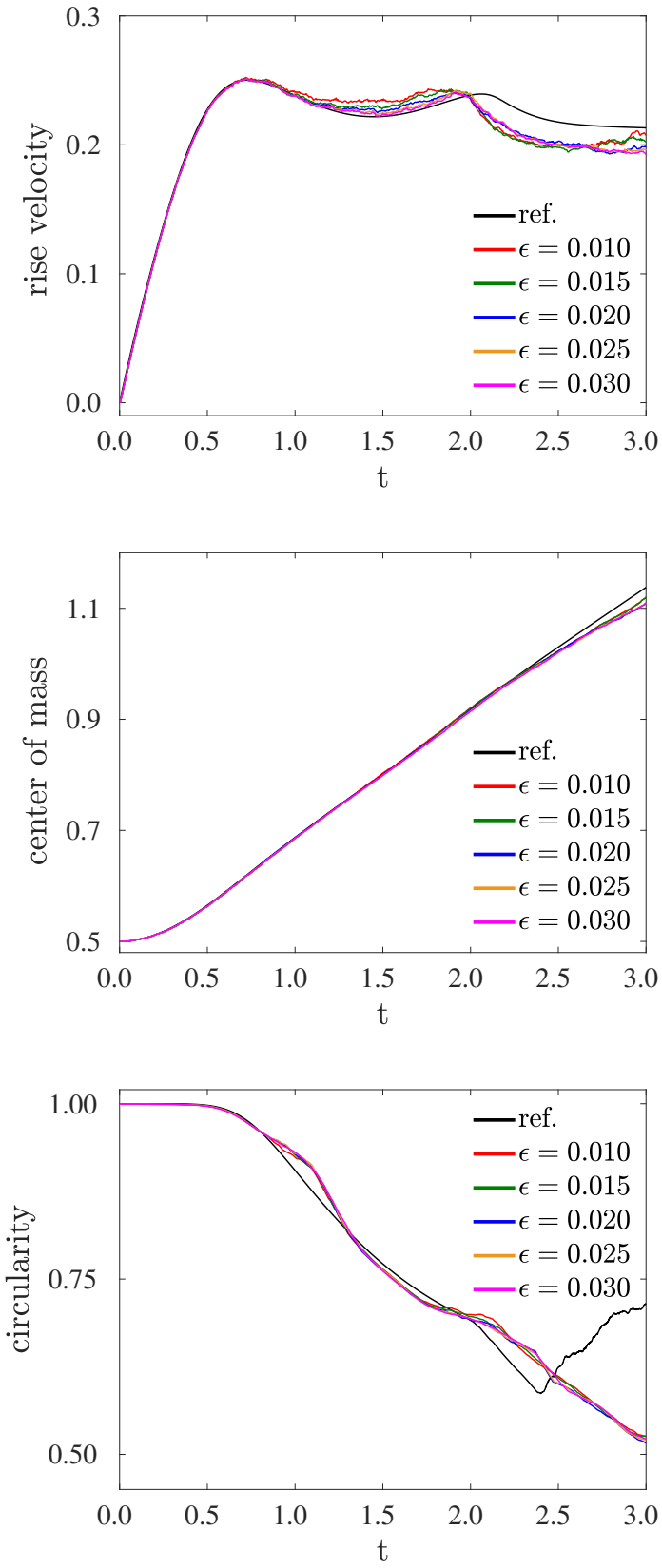

Figure 6.15: The bubble rise velocity, center of mass, and circularity for different values of ϵ, mesh refinement $h = 1/32$.

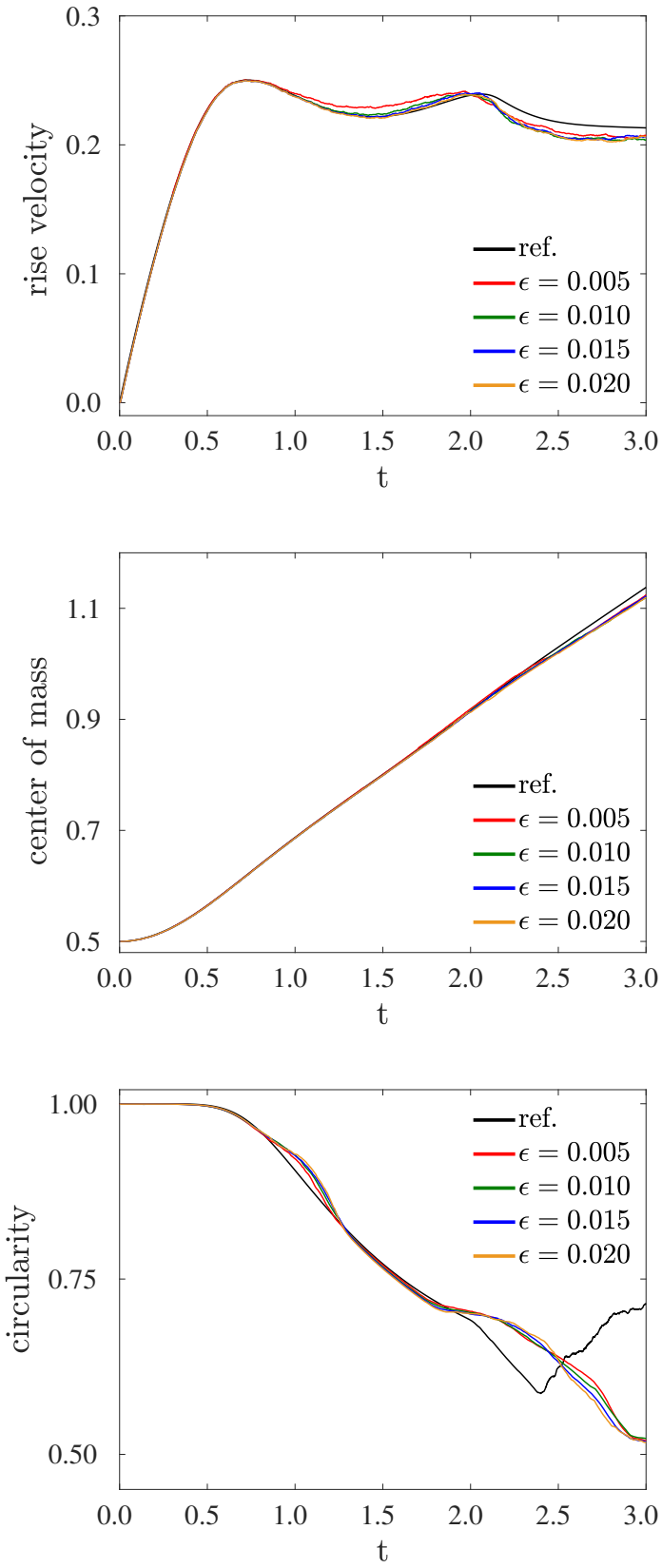

Figure 6.16: The bubble rise velocity, center of mass, and circularity for different values of ϵ, mesh refinement $h = 1/64$.

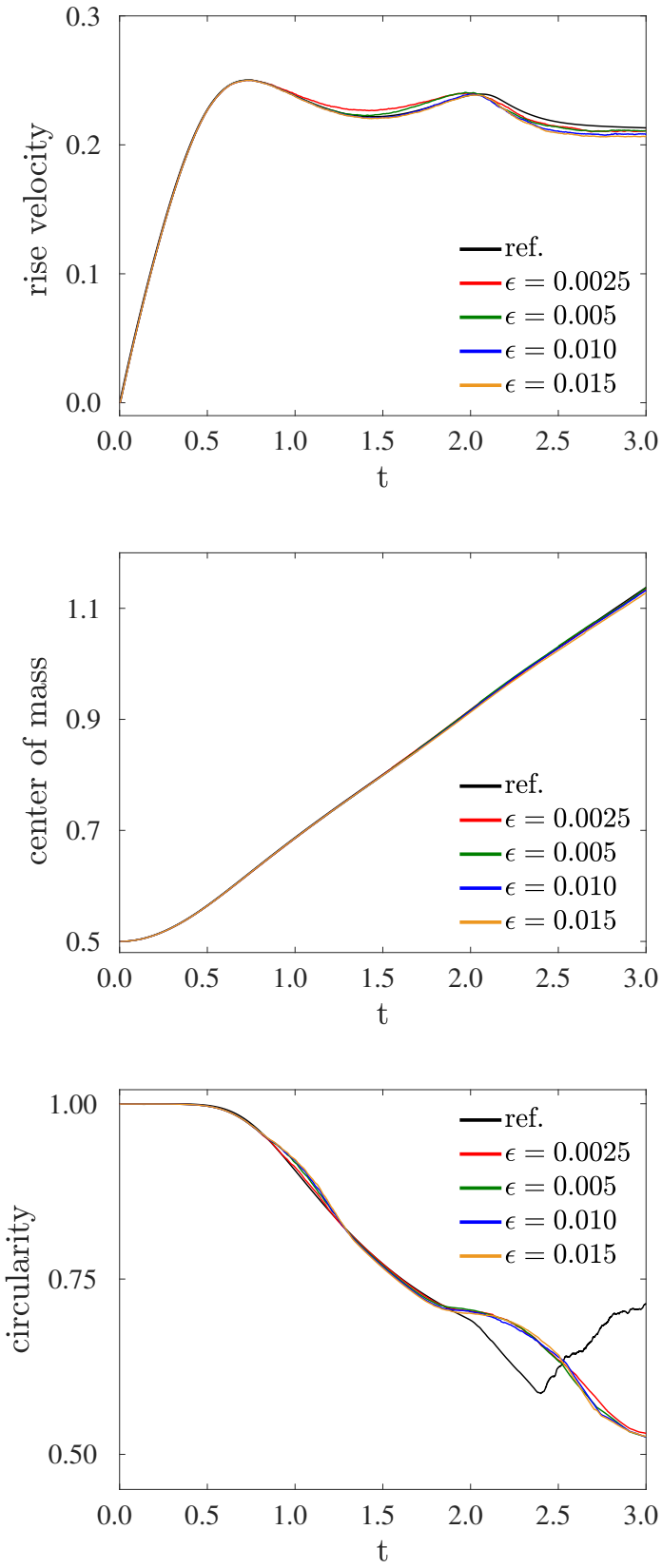

Figure 6.17: The bubble rise velocity, center of mass, and circularity for different values of ϵ, mesh refinement $h = 1/128$.

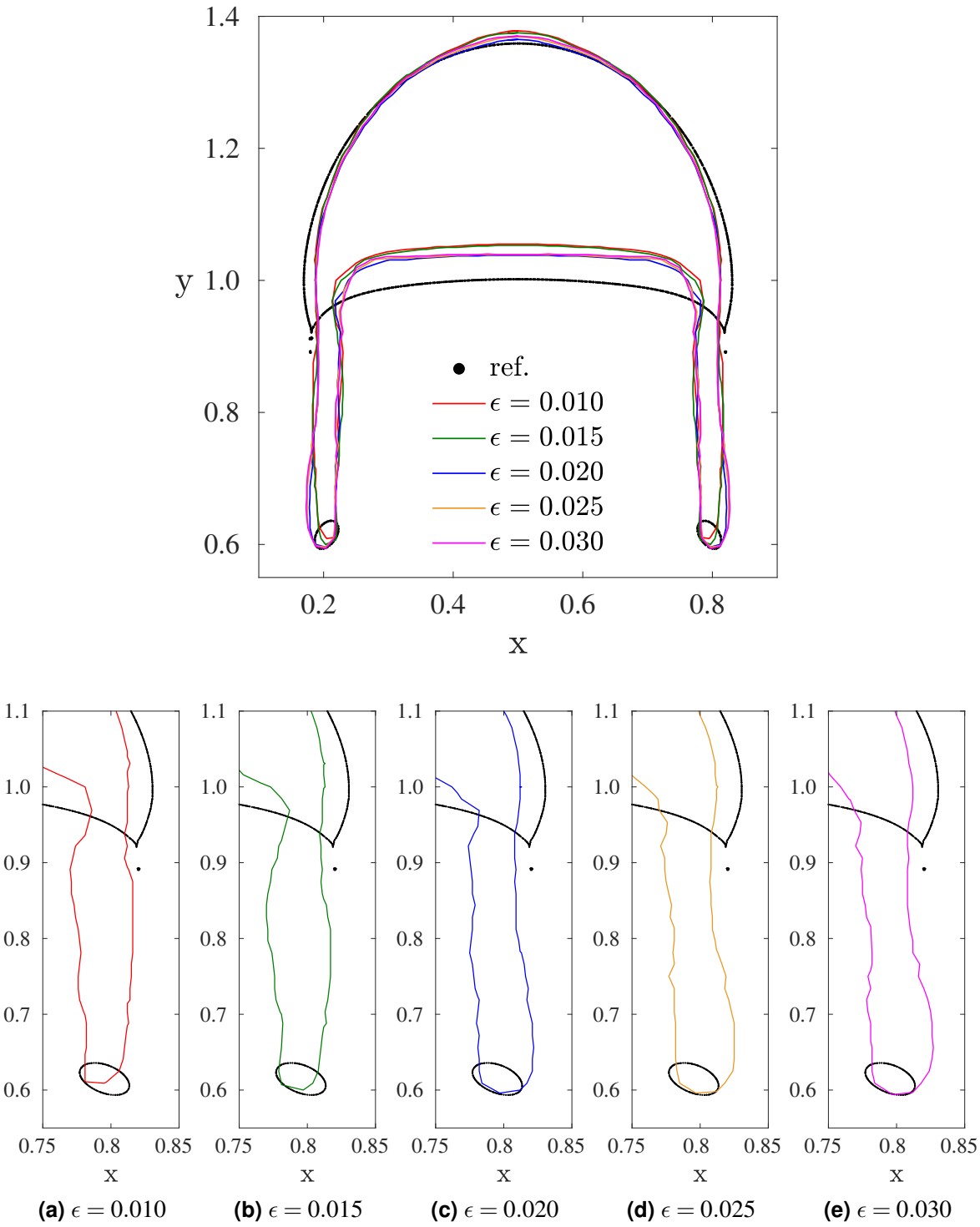

(a) $\epsilon = 0.010$ **(b)** $\epsilon = 0.015$ **(c)** $\epsilon = 0.020$ **(d)** $\epsilon = 0.025$ **(e)** $\epsilon = 0.030$

Figure 6.18: The bubble shape for different interface thickness values, at mesh refinement $h = 1/32$, superimposed on the reference (TP2D [28]) at final time $t = 3.0$.

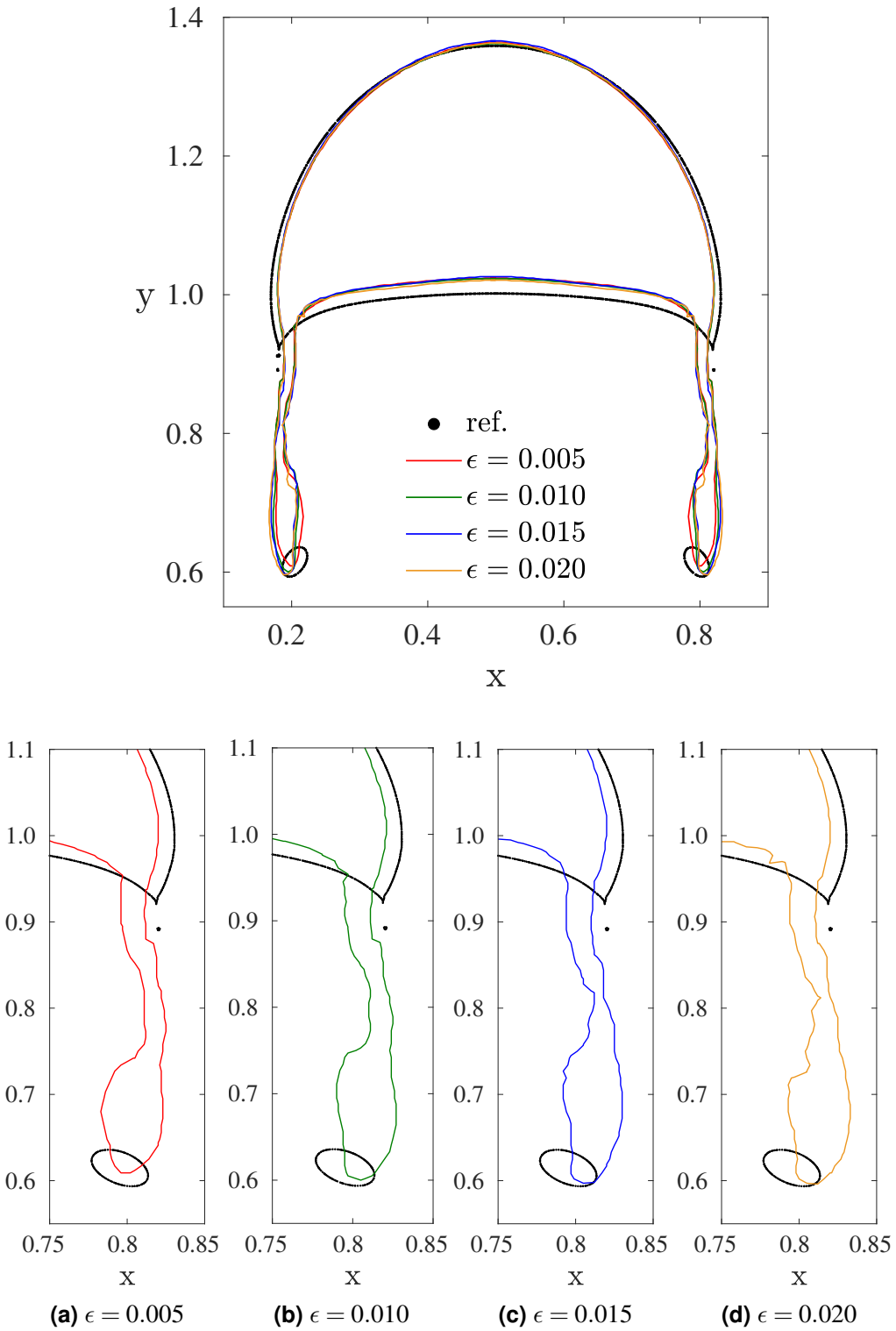

Figure 6.19: The bubble shape for different interface thickness values, at mesh refinement $h = 1/64$, superimposed on the reference (TP2D [28]) at final time $t = 3.0$.

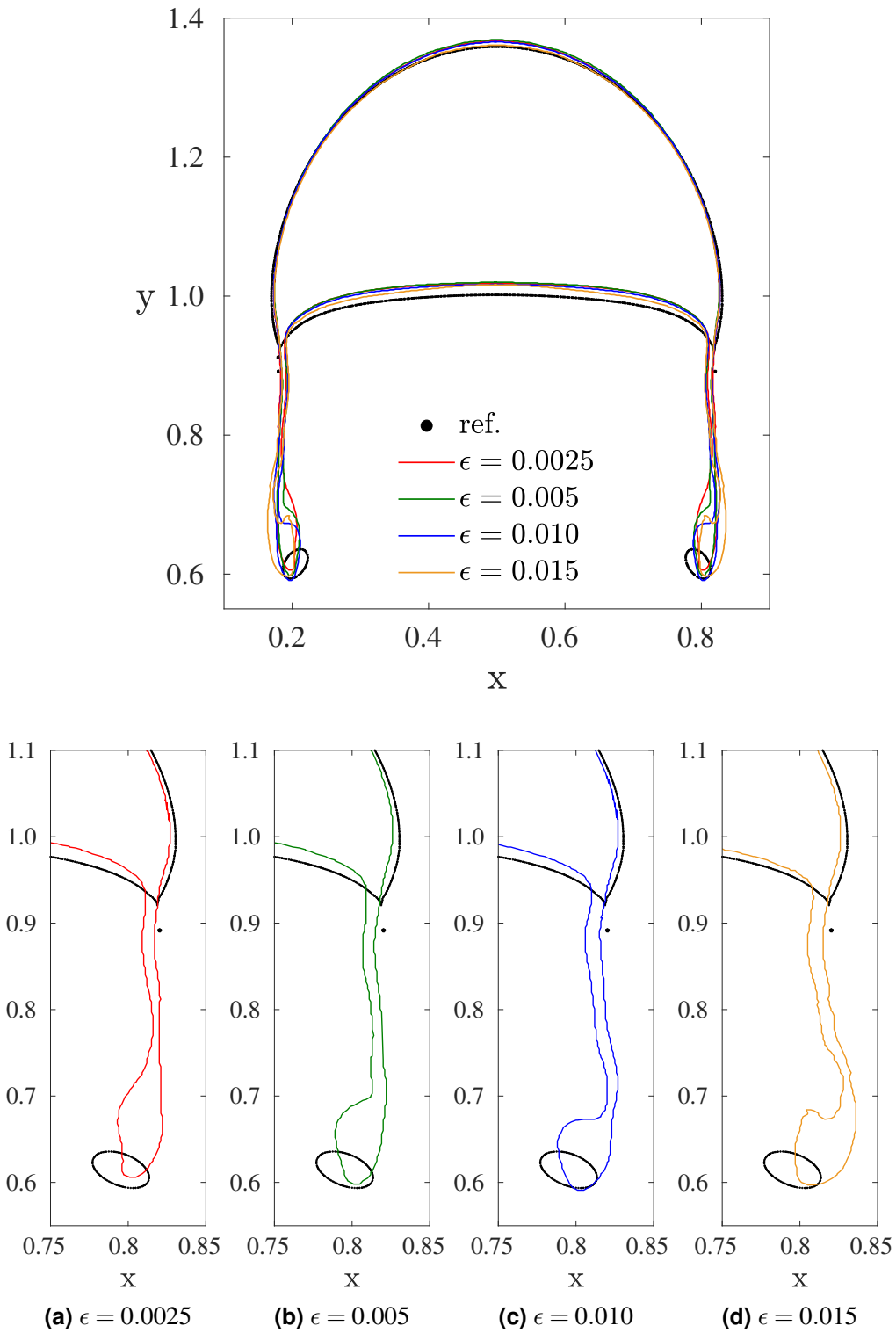

(a) $\epsilon = 0.0025$ **(b)** $\epsilon = 0.005$ **(c)** $\epsilon = 0.010$ **(d)** $\epsilon = 0.015$

Figure 6.20: The bubble shape for different interface thickness values, at mesh refinement $h = 1/128$, superimposed on the reference (TP2D [28]) at final time $t = 3.0$.

6.6.2 Time Step Size Study

In this section, the influence of the temporal discretization parameter, namely the time step size Δt, on the accuracy and stability of the numerical solver is investigated.

The investigation is carried out using three distinct time step sizes: $\Delta t = 5e-2$, $5e-3$, and $5e-4$, respectively, shown in Table 6.9. All tests are performed at a mesh resolution of $h = 1/64$, with interface thickness $\epsilon = 0.010$ $(0.6h)$, and reinitialization parameters are fixed at $\gamma_1 = 1e-4$ and $\gamma_2 = 1e-5$. The corresponding results for the rise velocity, center of mass, and circularity are presented in Fig. 6.21.

h	Δt	$\phi_{\min}$	$t\|_{\phi=\phi_{\min}}$	$\mathbf{u}_{\max,1}$	$t\|_{\mathbf{u}=\mathbf{u}_{\max,1}}$	$\mathbf{u}_{\max,2}$	$t\|_{\mathbf{u}=\mathbf{u}_{\max,2}}$	$X(t=3)$
1/64	$5e-2$	0.5143	3.000	0.2469	0.80	0.2346	2.00	0.8524
	$5e-3$	0.5191	3.000	0.2500	0.720	0.2392	1.955	1.1206
	$5e-4$	0.5201	3.000	0.2504	0.7150	0.2393	1.9650	1.1267
ref.		0.5869	2.4004	0.2524	0.7332	0.2434	2.0705	1.1380

Table 6.9: The quantitative results for three time steps, mesh refinement $h = 1/64$, interface thickness $\epsilon = 0.010$ $(0.6h)$, along with the reference results (TP2D [28]).

The results reveal that for the largest time step, $\Delta t = 5e-2$, the overall trends of the physical observables qualitatively follow the benchmark reference. However, noticeable deviations are observed: the bubble ascends more slowly, as reflected in the reduced value of center of mass, and circularity exhibits discrepancies indicative of temporal discretization errors. These deviations highlight the insufficiency of a coarse temporal resolution in accurately capturing the bubble dynamics.

In contrast, the results with $\Delta t = 5e-3$ and $\Delta t = 5e-4$ demonstrate excellent agreement with the reference quantities. The differences between these two smaller time steps are negligible, confirming that the solutions have reached a state of time step independence. For circularity, slight deviations are observed in the interval $2.0 \leq t \leq 3.0$, which can be attributed not to the numerical method itself but to differences in tail detachment behavior between TP2D [28] and other benchmark groups. Specifically, while TP2D predicts tail separation, other solvers produce attached tails, leading to a linear decrease in circularity more consistent with our results.

The bubble morphologies corresponding to each Δt are illustrated in Fig. 6.22. The case with $\Delta t = 5e-2$ clearly exhibits artificial tail separation, a manifestation of temporal discretization error. On the other hand, the bubble shapes for $\Delta t = 5e-3$ and $5e-4$ are identical at the final simulation time, reinforcing the conclusion that time step convergence has been achieved.

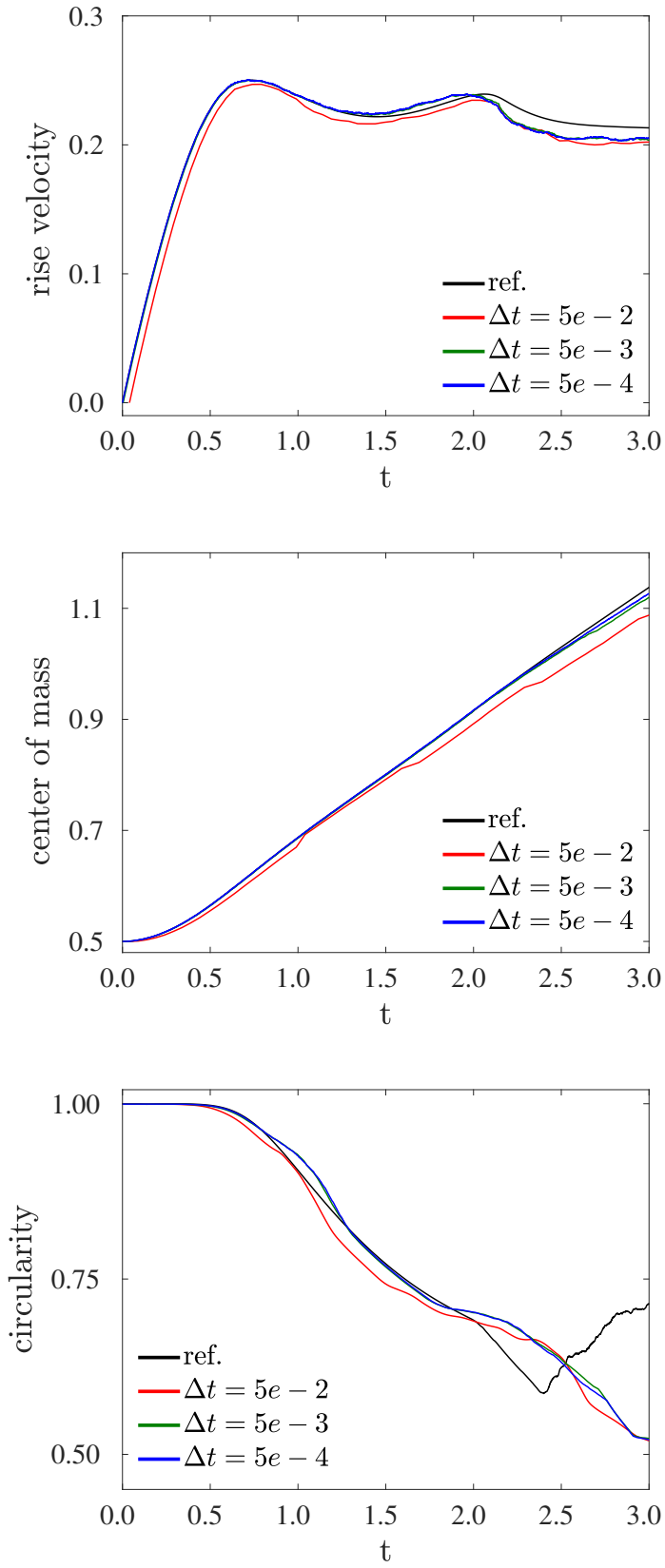

Figure 6.21: The bubble rise velocity, center of mass, and circularity for three time steps, mesh refinement $h = 1/64$, interface thickness $\epsilon = 0.010$ $(0.6h)$.

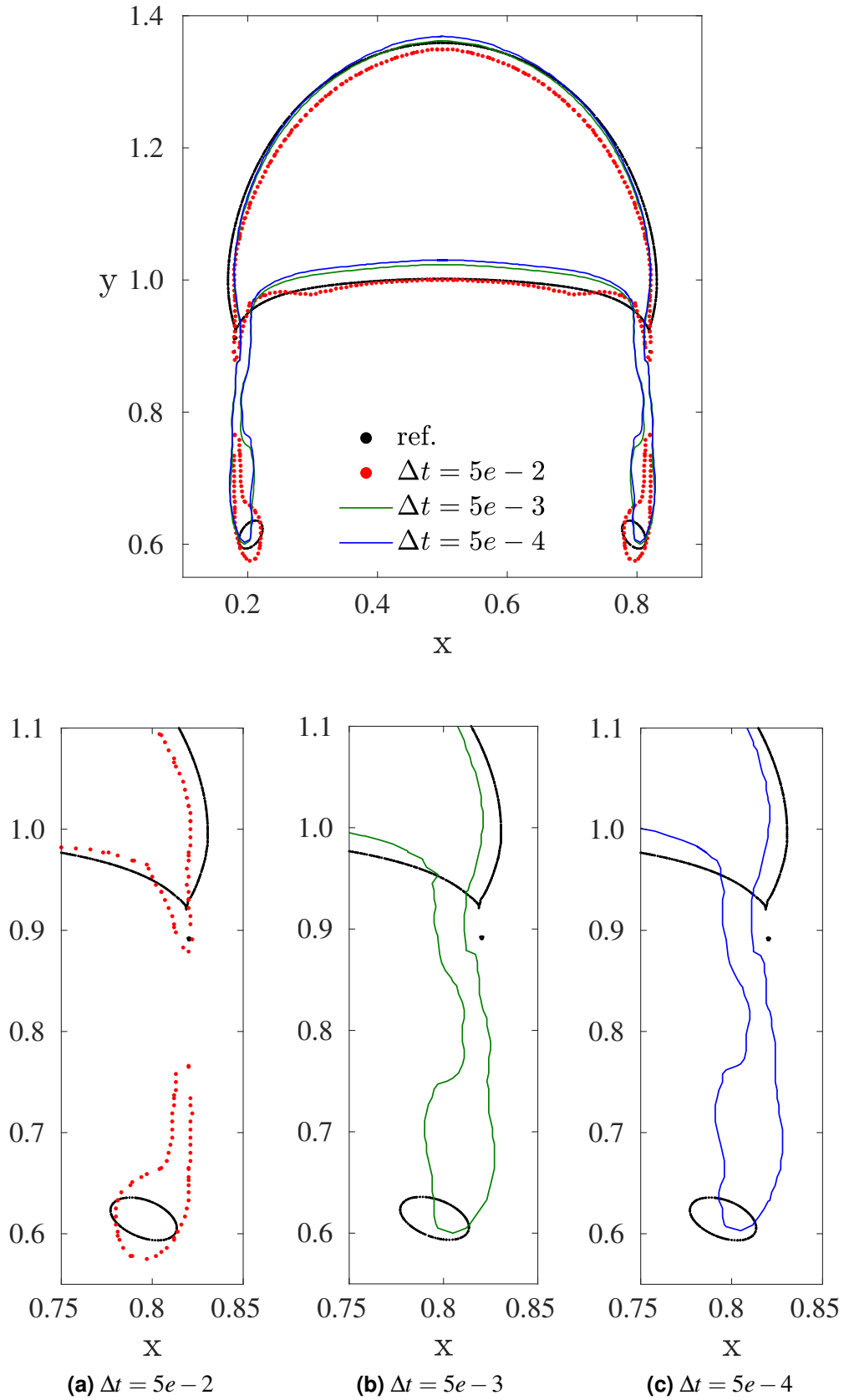

(a) $\Delta t = 5e-2$ **(b)** $\Delta t = 5e-3$ **(c)** $\Delta t = 5e-4$

Figure 6.22: The bubble shape for $\Delta t = 5e-2$, $5e-3$, and $5e-4$, at mesh refinement $h = 1/64$, superimposed on the reference (TP2D [28]) at final time $t = 3.0$.

Based on this analysis, $\Delta t = 5e-3$ is selected as the optimal choice for subsequent studies. It achieves numerical accuracy comparable to the finer time step ($\Delta t = 5e-4$) while offering a substantial reduction in computational cost, thus ensuring both efficiency and reliability of the simulations.

6.6.3 Effect of mesh refinement

In this section, we analyze the effect of the spatial discretization parameter, namely the mesh resolution h, on the accuracy, robustness, and convergence behavior of the solver.

The numerical study is conducted on three discretization levels: $h = 1/32$, $1/64$, and $1/128$. The time step is fixed as $\Delta t = 5e-3$, while the ϵ is chosen according to the optimal value (identified in the subsection "choice of interface thickness"). The reinitialization parameters are fixed at $\gamma_1 = 1e-4$ and $\gamma_2 = 1e-5$. The corresponding evolution of the rise velocity, center of mass, and circularity is summarized in Fig. 6.23 and Table 6.10.

As the mesh is refined ($h = 1/64$ and $1/128$), the discrepancies diminish substantially, showing excellent quantitative agreement with the reference values.

The bubble morphologies associated with each mesh level are presented in Fig. 6.24. With mesh refinements, the bubble profile progressively aligns with the reference solution, particularly in the upper part and lateral regions. Notably, the bubble tails become progressively thinner and more sharply resolved, reflecting improved spatial accuracy. However, further refinement could not be attempted due to solver (UMFPACK) limitations. The monolithic three-field formulation employed here, with velocity and material cut-off functions discretized using high order Q_2 elements, leads to a rapid growth in the number of unknowns, rendering finer meshes computationally prohibitive at the current stage.

h	ϵ	$\phi_{\min}$	$t\|_{\phi=\phi_{\min}}$	$\mathbf{u}_{\max,1}$	$t\|_{\mathbf{u}=\mathbf{u}_{\max,1}}$	$\mathbf{u}_{\max,2}$	$t\|_{\mathbf{u}=\mathbf{u}_{\max,2}}$	$X(t=3)$
1/32	0.020	0.5059	3.000	0.2514	0.725	0.2405	1.905	1.1094
1/64	0.010	0.5191	3.000	0.2500	0.720	0.2392	1.955	1.1206
1/128	0.0025	0.5194	3.000	0.2503	0.755	0.2401	1.980	1.1354
ref.		0.5869	2.4004	0.2524	0.7332	0.2434	2.0705	1.1380

Table 6.10: The quantitative results for mesh refinements $h = 1/32$, $1/64$, and $1/128$ along with the reference results (TP2D [28]).

The relative error norms of the principal physical quantities are summarized in Table 6.11. The finest numerical solution of the current study is employed as the reference against which all errors and convergence rates are evaluated.

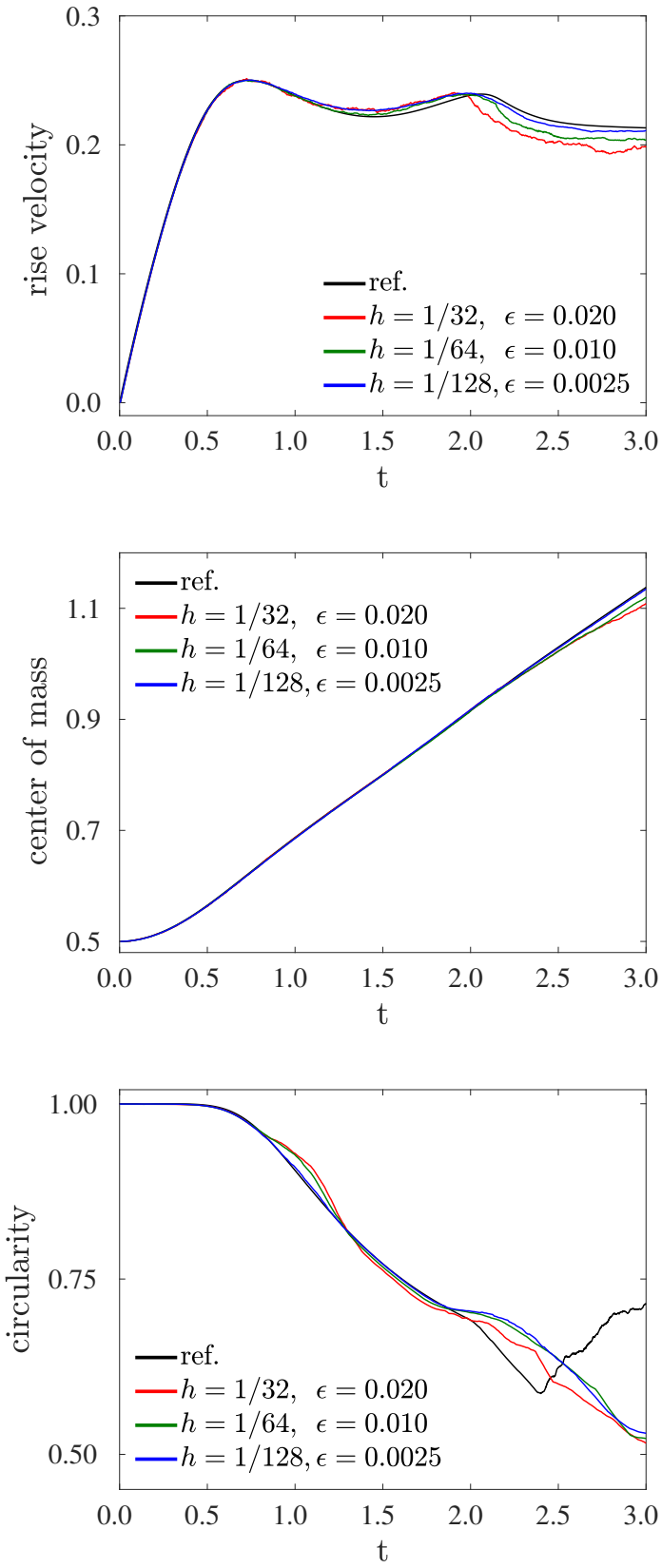

Figure 6.23: The bubble rise velocity, center of mass, and circularity for mesh refinements $h = 1/32$, $1/64$, and $1/128$.

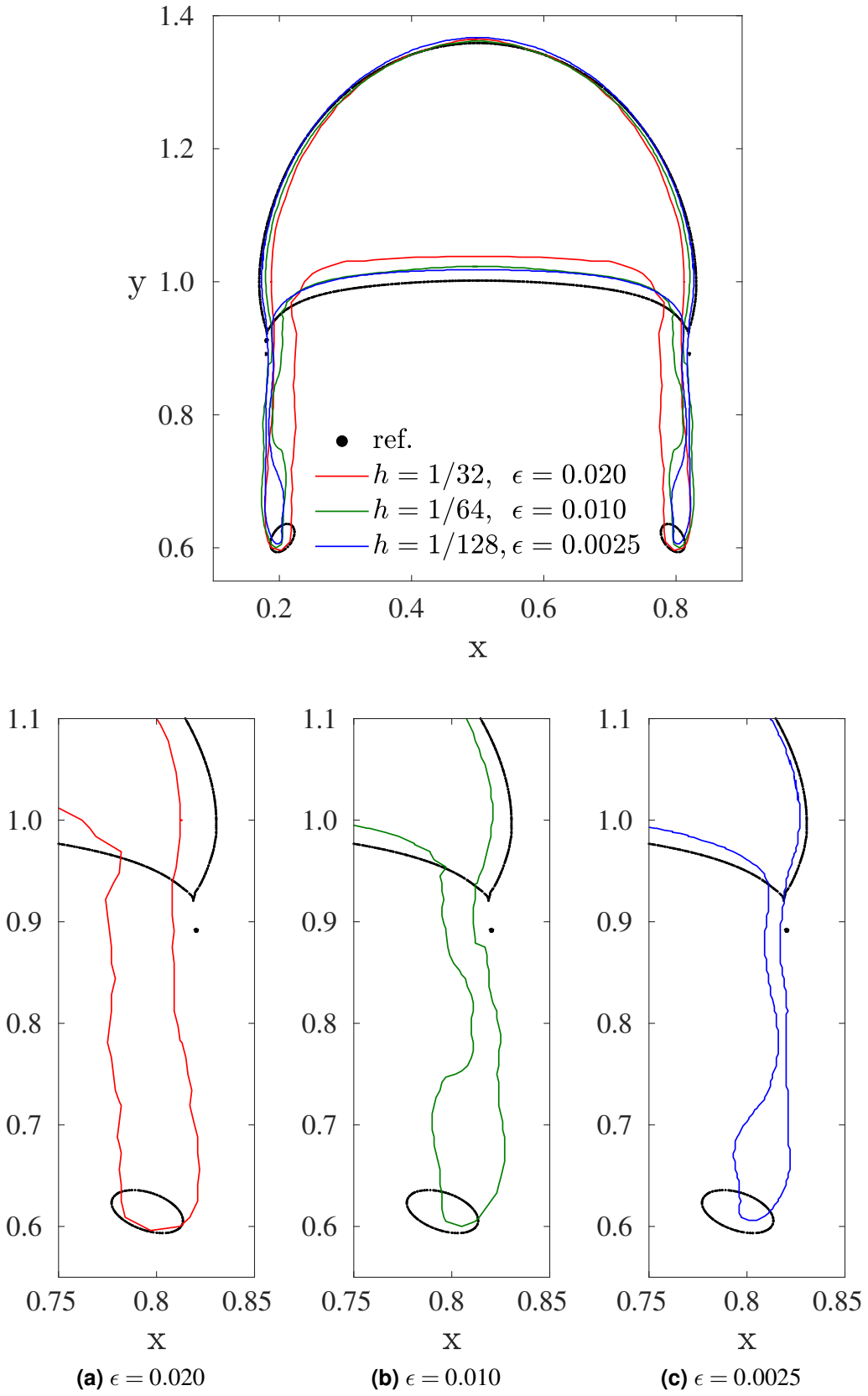

(a) $\epsilon = 0.020$ **(b)** $\epsilon = 0.010$ **(c)** $\epsilon = 0.0025$

Figure 6.24: The bubble shape at mesh refinements $h = 1/32$, $1/64$, and $1/128$, superimposed on the reference (TP2D [28]) at final time $t = 3.0$.

The results demonstrate that the estimated order of convergence (EOC) for all investigated quantities consistently falls between unity and approximately two across all considered norms.

This behavior indicates that the proposed monolithic multiphase flow solver exhibits a numerically robust and physically accurate convergence trend. The observed convergence rates confirm that the solver is capable of capturing interfacial dynamics with high fidelity, thereby reinforcing its suitability for simulating complex multiphase flow problems.

q	h	ϵ	$\|e\|_1$	EOC_1	$\|e\|_2$	EOC_2	$\|e\|_\infty$	EOC_∞
X	1/32	0.020	0.0059		0.0093		0.0216	
	1/64	0.010	0.0029	1.0247	0.0045	1.0473	0.0102	1.0825
u	1/32	0.020	0.0268		0.0381		0.0719	
	1/64	0.010	0.0134	1.0000	0.0172	1.1474	0.0336	1.0975
ϕ	1/32	0.020	0.0071		0.0095		0.0193	
	1/64	0.010	0.0030	1.2429	0.0040	1.2479	0.0086	1.1662

Table 6.11: The relative error norms and the estimated order of convergence for the benchmark quantities.

7

Indicator Function

Earlier chapters addressed interfacial flow modeling using CSF and CSS formulations, where the level set function ϕ requires costly reinitialization to preserve its distance property, often affecting mass conservation [109]. To avoid this, a material cut-off function ψ is introduced, eliminating redistancing and curvature evaluation but still depending on the interface thickness parameter ϵ. To further enhance robustness and mass conservation, this chapter introduces the color function (or indicator function) denoted as $\psi_I(x,t)$ [110], as an alternative interface representation.

This scalar function is bounded between $-\frac{1}{2}$ and $\frac{1}{2}$, with $\psi_I(x,t) = \frac{1}{2}$ corresponding to fluid A and $\psi_I(x,t) = -\frac{1}{2}$ to fluid B. The use of such color functions in interface capturing was first proposed by Nichols and Hirt [7, 8] in the volume of fluid (VOF) method. Notably, the advection of the color function is strictly mass conservative and does not require any redistancing [28].

Although the color function is less smooth than the level set function, which can hinder curvature evaluation, this drawback is naturally resolved in the CSS formulation, where curvature and interface normals are not computed explicitly. Thus, incorporating the color/indicator function into the curvature free material cut-off function (CSS) framework provides a mass conservative and computationally robust alternative for modeling interfacial flows.

7.1 Rising Bubble Benchmark

To test the accuracy and efficiency of the above idea for the system of equations (2.6.3), the numerical study for the rising bubble benchmark (test case 1 and 2) is carried out. The color function for this geometrical configuration is defined as follows

$$\psi_I(x,t) = \begin{cases} \frac{1}{2} & \text{if} \quad x \in \Omega_1(t), \\ -\frac{1}{2} & \text{if} \quad x \in \Omega_2(t). \end{cases} \tag{7.1.1}$$

7.1.1 Test Case 1

To assess the performance of the proposed solver, the validation is carried out on three successive mesh refinement levels, while the time step size is fixed at $\Delta t = 5e-3$, with $\gamma_1 = 1e-4$ and $\gamma_2 = 1e-5$.

The numerical results obtained with the present approach, presented in Fig. 7.1 are consistent with those generated using the previously established approach. Consequently, exhibiting a clear convergence trend toward the reference results with mesh refinement.

The temporal evolution of the bubble shape is further examined at seven distinct time instances to capture its development. The final bubble contour is superimposed with the reference solution of Hysing et al. [28], as depicted in Fig. 7.2. At the initial time ($t = 0$), the bubble deviates slightly from a perfect circular shape, with small oscillations visible at the interface. As the bubble rises, surface tension forces gradually stabilize the interface, restoring its circularity, as corroborated by the circularity measure shown in Fig. 7.1. Importantly, Fig. 7.2 also confirms that mesh refinement enhances accuracy.

This qualitative behavior is supported by quantitative comparisons presented in Table 7.1, exhibiting excellent agreement with reference values. Furthermore, the relative error norms of the principal physical quantities are reported in Table 7.2. The results demonstrate that the errors consistently decrease with mesh refinement, and the observed estimated order of convergence (EOC) lie between unity and approximately two for all quantities and norms.

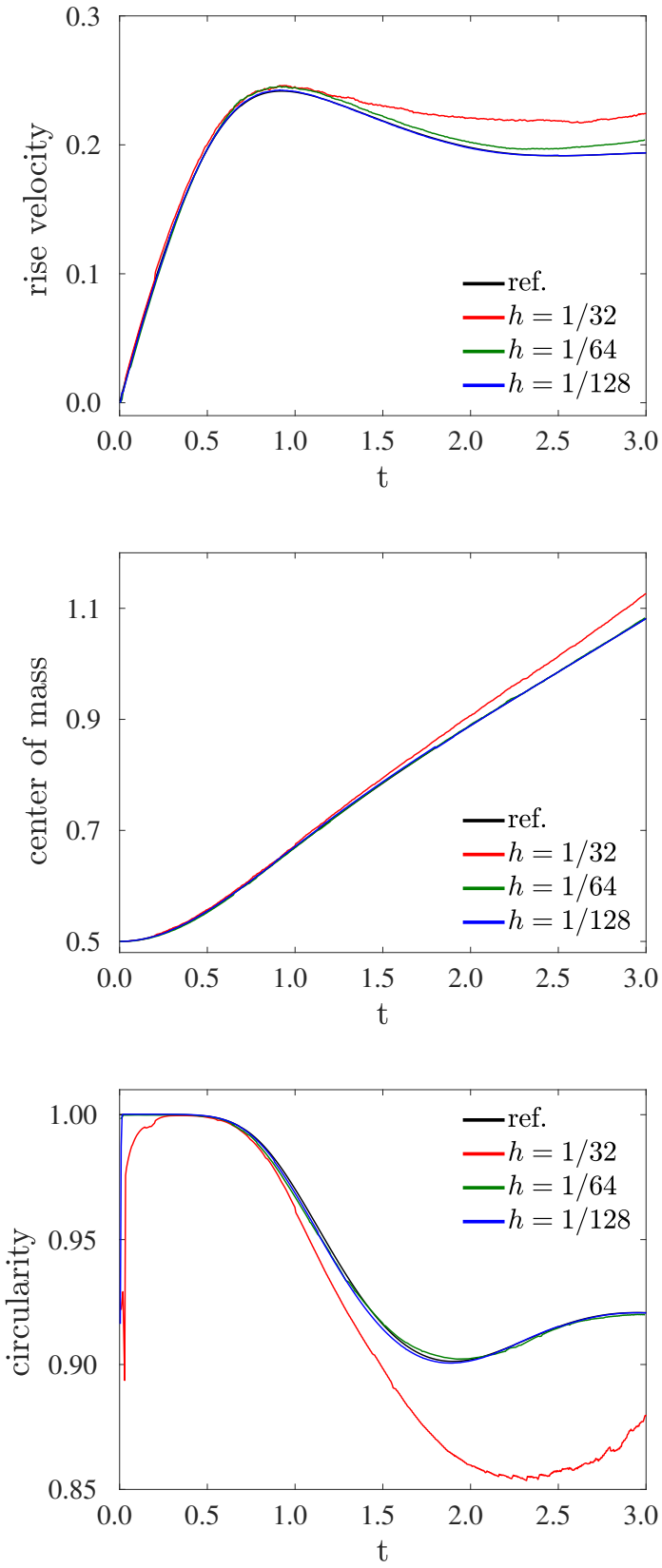

Figure 7.1: The bubble rise velocity, center of mass, and circularity for mesh refinements $h = 1/32$, $1/64$, and $1/128$.

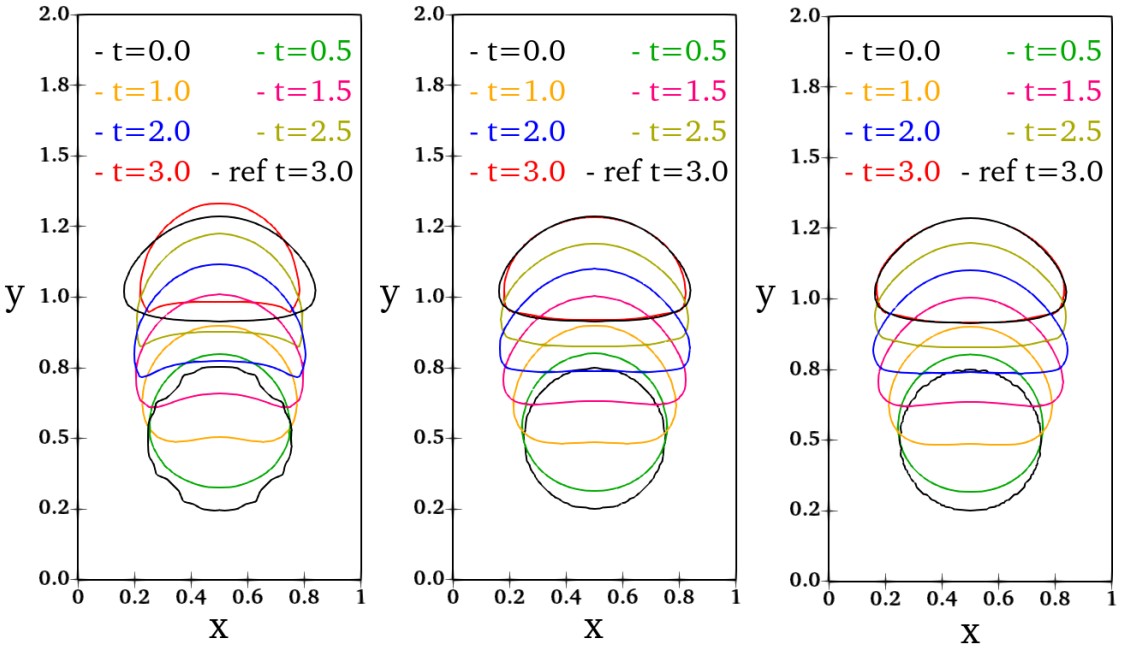

(a) $h = 1/32$ **(b)** $h = 1/64$ **(c)** $h = 1/128$

Figure 7.2: Bubble evolution at mesh refinements $h = 1/32$, $1/64$, and $1/128$, superimposed on the reference (TP2D [28]) at final time $t = 3.0$.

h	$\phi_{\min}$	$t\|_{\phi=\phi_{\min}}$	$\mathbf{u}_{\max}$	$t\|_{\mathbf{u}=\mathbf{u}_{\max}}$	$X(t=3)$
1/32	0.8536	2.320	0.2461	0.915	1.1262
1/64	0.9022	1.930	0.2453	0.920	1.0827
1/128	0.9006	1.890	0.2426	0.915	1.0813
ref.	0.9013	1.9041	0.2417	0.9213	1.0813

Table 7.1: The quantitative results for three mesh refinements $h = 1/32$, $1/64$, and $1/128$ along with the reference results (TP2D [28]).

q	h	$\|e\|_1$	EOC_1	$\|e\|_2$	EOC_2	$\|e\|_\infty$	EOC_∞
X	1/32	0.0239		0.0309		0.0518	
	1/64	0.0021	3.4414	0.0026	3.5710	0.0035	3.8875
	1/128	0.0011	0.9328	0.0013	1.0000	0.0015	1.2630
u	1/32	0.0739		0.0877		0.1281	
	1/64	0.0151	2.2910	0.0195	2.1691	0.0374	1.7762
	1/128	0.0027	2.4835	0.0038	2.3594	0.0096	1.9619
ϕ	1/32	0.0219		0.0301		0.0712	
	1/64	0.0012	4.1898	0.0013	4.5332	0.0039	4.1903
	1/128	0.0008	0.5850	0.0009	0.5305	0.0028	0.4780

Table 7.2: The relative error norms and the estimated order of convergence for the benchmark quantities.

7.1.2 Test Case 2

The rising bubble benchmark (test case 2) is simulated using the same optimal parameters as aforementioned, with validation performed over three mesh refinement levels, presented in Fig. 7.3. The results exhibit consistent convergence toward the reference solution of Hysing et al. [28]. Moreover, the method accurately reproduces bubble dynamics, including elongated tail formation without breakup, demonstrating numerical stability and physical fidelity, shown in Fig. 7.4. Quantitative measures (Table 7.3) and the computed error norms (Table 7.4) confirm first- to second-order convergence across all cases.

h	$\phi_{\min}$	$t\|_{\phi=\phi_{\min}}$	$\mathbf{u}_{\max,1}$	$t\|_{\mathbf{u}=\mathbf{u}_{\max,1}}$	$\mathbf{u}_{\max,2}$	$t\|_{\mathbf{u}=\mathbf{u}_{\max,2}}$	$X(t=3)$
1/32	0.5133	3.0	0.2528	0.880	0.2439	1.925	1.1207
1/64	0.5241	3.0	0.2504	0.725	0.2422	1.890	1.1291
1/128	0.5409	3.0	0.2485	0.715	0.2411	1.945	1.1396
ref.	0.5869	2.4004	0.2524	0.7332	0.2434	2.0705	1.1380

Table 7.3: The quantitative results for three mesh refinements $h = 1/32$, $1/64$, and $1/128$ along with the reference results (TP2D [28]).

Overall, the present monolithic, distancing-free, and interface-thickness-independent formulation proves to be a robust and accurate approach for simulating interfacial flow problems.

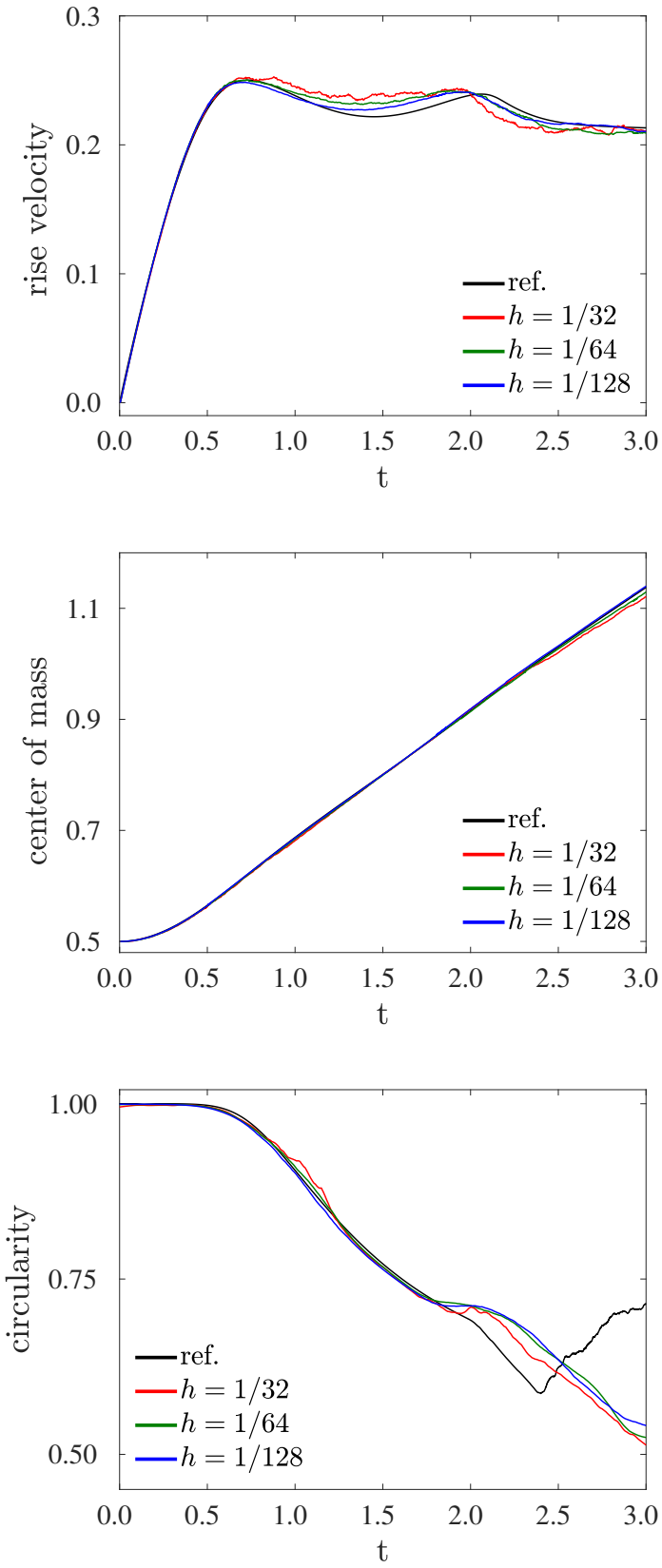

Figure 7.3: The bubble rise velocity, center of mass, and circularity for mesh refinements $h = 1/32$, $1/64$, and $1/128$.

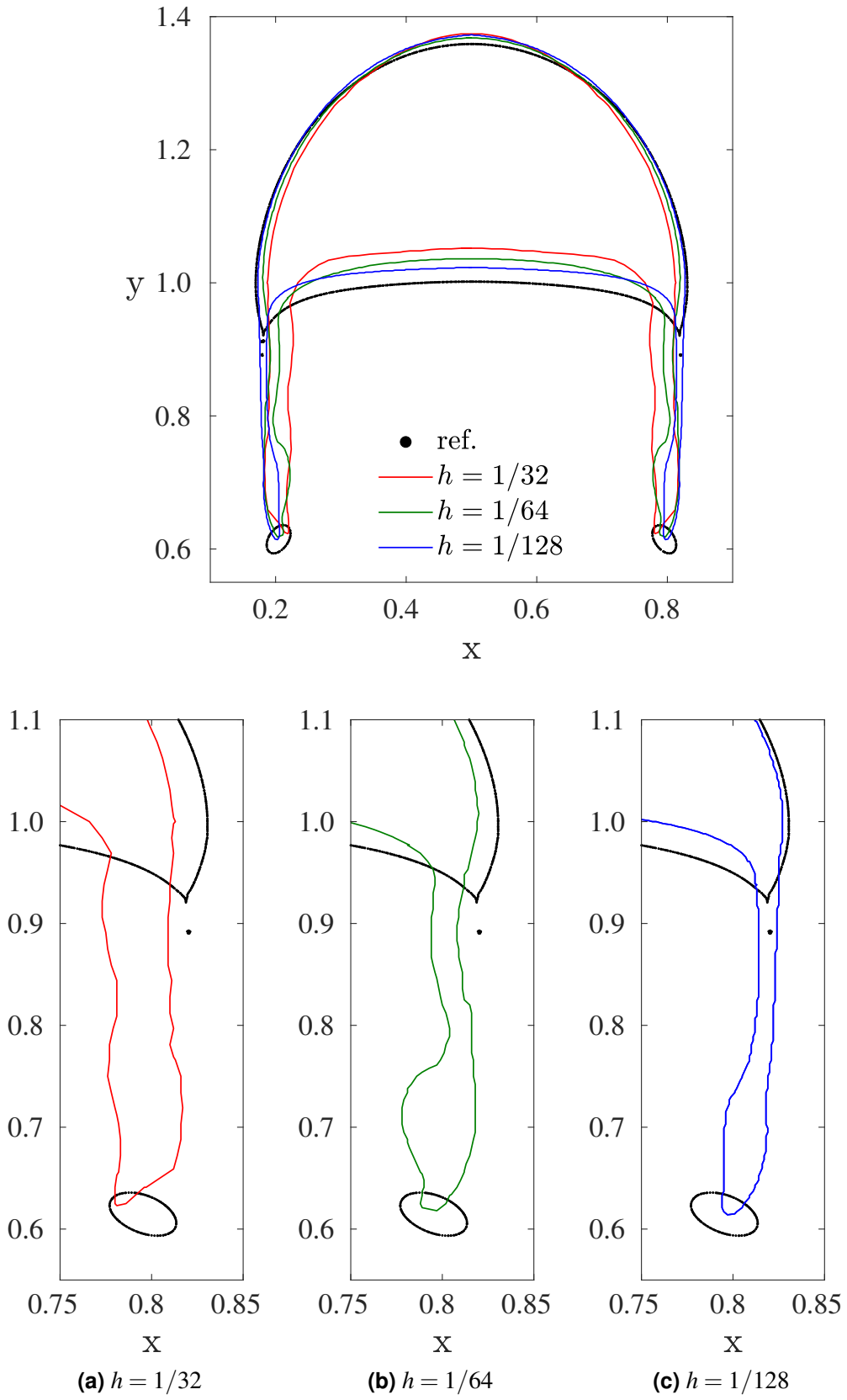

(a) $h = 1/32$ **(b)** $h = 1/64$ **(c)** $h = 1/128$

Figure 7.4: Bubble evolution at mesh refinements $h = 1/32$, $1/64$, and $1/128$, superimposed on the reference (TP2D [28]) at final time $t = 3.0$.

q	h	$\|e\|_1$	EOC_1	$\|e\|_2$	EOC_2	$\|e\|_\infty$	EOC_∞
X	1/32	0.0041		0.0052		0.0078	
	1/64	0.0014	1.5502	0.0016	1.7004	0.0026	1.5849
u	1/32	0.0237		0.0283		0.0491	
	1/64	0.0125	0.9270	0.0151	0.9067	0.0291	0.7561
ϕ	1/32	0.0159		0.0213		0.0415	
	1/64	0.0086	0.8895	0.0122	0.8014	0.0252	0.7197

Table 7.4: The relative error norms and the estimated order of convergence for the benchmark quantities.

8

Summary and Outlook

The work presented in this thesis has been devoted to the development, implementation, and detailed parametric study of a distancing-free monolithic multiphase flow solver designed to capture complex interfacial dynamics with high accuracy. The central motivation was to address some of the long-standing challenges in multiphase flow simulations: the accurate and stable treatment of surface tension forces, the capillary time step restriction associated with classical CSF approaches, and the mass conservation issues arising from redistancing or reinitialization procedures commonly required in level set frameworks.

The progression of this work begins with a discussion of classical multiphase models and their limitations, and contrasts them with the tensor-based CSS approach. This formulation not only provides computational advantages by avoiding curvature evaluation but also enforces a more consistent representation of interfacial stresses. The mathematical model that results from this formulation is shown to satisfy fundamental conservation laws, providing a solid theoretical foundation for the solver.

Building on this, the discretization of the governing equations is analyzed in detail. The focus is placed on the finite element approximation of the Stokes subsystem within the full three-field monolithic formulation. Particular attention is given to the saddle-point structure of the Stokes problem and the choice of compatible finite element spaces to ensure stable and accurate discretization. The numerical framework is then extended by discussing the spatial and temporal discretization strategies, the treatment of discontinuous material properties such as density and viscosity, the Newton-based linearization of

the non-linear system, and the selection of suitable linear solver. Together, these steps provide a comprehensive account of how the final computational scheme is constructed.

The robustness and accuracy of the solver have been assessed through a wide range of numerical experiments. Test cases involving surface tension effects, capillary time step restrictions, and multiphase flow benchmark confirm that the solver is both efficient and reliable in capturing interfacial dynamics. In particular, the well-known rising bubble benchmark (test case 1 and 2) were used as stringent validation tests, since they involve significant interfacial deformation and topological change. The successful reproduction of these benchmark results provides strong evidence of the solver's predictive capabilities.

A further contribution of this work is the introduction of an indicator (color) function to describe the fluid interface, thereby eliminating the need for redistancing, which is both computationally demanding and prone to introducing mass loss. While the indicator function is less smooth than a level set function, its potential drawbacks are naturally mitigated by the CSS formulation, which avoids explicit curvature evaluation. This innovation therefore leads to a curvature free, mass conservative, and computationally efficient framework for modeling multiphase flows.

The resulting solver is demonstrated to be robust, efficient, and accurate, and thus constitutes a significant advancement in the numerical simulation of multiphase flows.

While the present study has made substantial progress in advancing the numerical modeling of multiphase flows, several directions remain open for future research. A natural extension is the application of the solver to three-dimensional problems involving more complex interfacial dynamics and topological transitions. Further improvements could be achieved by incorporating adaptive mesh refinement strategies to better capture fine-scale interface structures while maintaining computational efficiency. Additionally, exploring parallel implementations and high-performance computing techniques would significantly enhance the scalability of the solver, making it suitable for large-scale industrial and scientific applications. These future developments would further strengthen the solver's applicability as a general-purpose tool for interfacial flow problems.

Bibliography

[1] G. F. Hewitt and G. Yadigaroglu. *Introduction to Multiphase Flow: Basic Concepts, Applications and Modelling*. Springer, 2018. ISBN 978-3-319-58718-9.

[2] S. Popinet. Numerical models of surface tension. *Annual Review of Fluid Mechanics*, 50:49–75, 2018. ISSN 1545-4479. doi: https://doi.org/10.1146/annurev-fluid-122316-045034. URL https://www.annualreviews.org/content/journals/10.1146/annurev-fluid-122316-045034.

[3] C. S. Peskin. Flow patterns around heart valves: A numerical method. *Journal of Computational Physics*, 10(2):252–271, 1972. ISSN 0021-9991. doi: https://doi.org/10.1016/0021-9991(72)90065-4. URL https://www.sciencedirect.com/science/article/pii/0021999172900654.

[4] C. S. Peskin. Numerical analysis of blood flow in the heart. *Journal of Computational Physics*, 25(3):220–252, 1977. ISSN 0021-9991. doi: https://doi.org/10.1016/0021-9991(77)90100-0. URL https://www.sciencedirect.com/science/article/pii/0021999177901000.

[5] S. O. Unverdi and G. Tryggvason. A front-tracking method for viscous, incompressible, multi-fluid flows. *Journal of Computational Physics*, 100(1):25–37, 1992. ISSN 0021-9991. doi: https://doi.org/10.1016/0021-9991(92)90307-K. URL https://www.sciencedirect.com/science/article/pii/002199919290307K.

[6] G. Tryggvason, B. Bunner, A. Esmaeeli, D. Juric, N. Al-Rawahi, W. Tauber, J. Han, S. Nas, and Y. J. Jan. A front-tracking method for the computations of multiphase flow. *Journal of Computational Physics*, 169(2):708–759, 2001. ISSN 0021-9991. doi: https://doi.org/10.1006/jcph.2001.6726. URL https://www.sciencedirect.com/science/article/pii/S0021999101967269.

[7] B. D. Nichols and C. W. Hirt. Methods for calculating multi-dimensional, transient free surface flows past bodies. Los Alamos Scientific Lab., N. Mex. (USA), 01 1975. URL https://www.osti.gov/biblio/5044626.

[8] C. W. Hirt and B. D. Nichols. Volume of fluid (VOF) method for the dynamics of free boundaries. *Journal of Computational Physics*, 39(1):201–225, 1981. ISSN 0021-9991. doi: https://doi.org/10.1016/0021-9991(81)90145-5. URL https://www.sciencedirect.com/science/article/pii/0021999181901455.

[9] R. Scardovelli and S. Zaleski. Direct numerical simulation of free-surface and interfacial flow. *Annual Review of Fluid Mechanics*, 31, 01 1999. doi: 10.1146/annurev.fluid.31.1.567.

[10] X. Feng, Y. He, and C. Liu. Analysis of finite element approximations of a phase field model for two-phase fluids. *Mathematics of Computations*, 76:539–571, 04 2007. doi: 10.1090/S0025-5718-06-01915-6.

[11] P. Yue, J. Feng, C. Liu, and J. Shen. A diffuse-interface method of simulating two-phase flows of complex fluids. *Journal of Fluid Mechanics*, 515:293 – 317, 09 2004. doi: 10.1017/S0022112004000370.

[12] D. M. Anderson, G. B. McFadden, and A. A. Wheeler. Diffuse-interface methods in fluid mechanics. *Annual Review of Fluid Mechanics*, 30(1):139–165, 1998. doi: 10.1146/annurev.fluid.30.1.139. URL https://doi.org/10.1146/annurev.fluid.30.1.139.

[13] V. E. Badalassi, H. D. Ceniceros, and S. Banerjee. Computation of multiphase systems with phase field models. *Journal of Computational Physics*, 190(2):371–397, 2003. ISSN 0021-9991. doi: https://doi.org/10.1016/S0021-9991(03)00280-8. URL https://www.sciencedirect.com/science/article/pii/S0021999103002808.

[14] S. Osher and J. A. Sethian. Fronts propagating with curvature-dependent speed: Algorithms based on Hamilton-Jacobi formulations. *Journal of Computational Physics*, 79(1):12–49, 1988. ISSN 0021-9991. doi: https://doi.org/10.1016/0021-9991(88)90002-2. URL https://www.sciencedirect.com/science/article/pii/0021999188900022.

[15] M. Sussman, P. Smereka, and S. Osher. A level set approach for computing solutions to incompressible two-phase flow. *Journal of Computational Physics*, 114:146–159, 1994. doi: 10.1006/jcph.1994.1155.

[16] M. Sussman, E. Fatemi, P. Smereka, and S. Osher. An improved level set method for incompressible two-phase flows. *Computers & Fluids*, 27(5-6):663–680, 1998.

[17] S. Osher and R. Fedkiw. *Level Set Methods and Dynamic Implicit Surfaces*, volume 153. Springer New York, NY, 2003. ISBN 978-1-4684-9251-4. doi: 10.1007/b98879. URL http://dx.doi.org/10.1007/b98879.

[18] J. A. Sethian. *Level Set Methods and Fast Marching Methods: Evolving Interfaces in Computational Geometry, Fluid Mechanics, Computer Vision, and Materials Science.* Cambridge monographs on applied and computational mathematics. Cambridge University Press, 1999.

[19] B. Lafaurie, C. Nardone, R. Scardovelli, S. Zaleski, and G. Zanetti. Modelling merging and fragmentation in multiphase flows with SURFER. *Journal of Computational Physics*, 133(1):134–147, 1994. ISSN 0021-9991. doi: https://doi.org/10.1006/jcph.1994.1123. URL https://www.sciencedirect.com/science/article/pii/S0021999184711235.

[20] M. Boger. *Numerical Modeling of Compressible Two-Phase Flows with a Pressure-Based Method.* PhD thesis, University of Stuttgart, Institute of Aerodynamics and Gas Dynamics, December 2013.

[21] J. U. Brackbill, D. B. Kothe, and C. Zemach. A continuum method for modeling surface tension. *Journal of Computational Physics*, 100(2):335–354, 1992. ISSN 0021-9991. doi: https://doi.org/10.1016/0021-9991(92)90240-Y. URL https://www.sciencedirect.com/science/article/pii/002199919290240Y.

[22] A. Ouazzi, S. Turek, and H. Damanik. A curvature-free multiphase flow solver via surface stress-based formulation. *International Journal for Numerical Methods in Fluids*, 88(1):18–31, 2018. doi: https://doi.org/10.1002/fld.4509.

[23] M. A. Afaq, S. Turek, A. Ouazzi, and A. Fatima. Monolithic Newton-multigrid solver for multiphase flow problems with surface tension. Technical report, Fakultät für Mathematik, TU Dortmund, January 2021. Ergebnisberichte des Instituts für Angewandte Mathematik, Nummer 636.

[24] A. Fatima, S. Turek, A. Ouazzi, and M. A. Afaq. An adaptive discrete Newton method for regularization-free bingham model. In *Book of Extended Abstracts of the 6th ECCOMAS Young Investigators Conference 7th-9th July 2021, Valencia, Spain*, pages 180–189, Valencia, Spain, 2021. Editorial Universitat Politècnica de València.

[25] M. A. Afaq, A. Fatima, S. Turek, and A. Ouazzi. Robust monolithic multigrid FEM solver for three field formulation of incompressible flow problems. Technical report, Fakultät für Mathematik, TU Dortmund, January 2023. Ergebnisberichte des Instituts für Angewandte Mathematik, Nummer 659.

[26] S. Osher and R. Fedkiw. *Level Set Methods and Dynamic Implicit Surfaces*. Springer New York, NY, 2003. ISBN 978-1-4684-9251-4. doi: 10.1007/b98879.

[27] F. Gibou, R. Fedkiw, and S. Osher. A review of level-set methods and some recent applications. *Journal of Computational Physics*, 353:82–109, 2018. ISSN 0021-9991. doi: https://doi.org/10.1016/j.jcp.2017.10.006. URL https://www.sciencedirect.com/science/article/pii/S0021999117307441.

[28] S. Hysing, S. Turek, D. Kuzmin, N. Parolini, E. Burman, S. Ganesan, and L. Tobiska. Quantitative benchmark computations of two-dimensional bubble dynamics. *International Journal for Numerical Methods in Fluids*, 60(11):1259–1288, 2009. doi: https://doi.org/10.1002/fld.1934. URL https://onlinelibrary.wiley.com/doi/abs/10.1002/fld.1934.

[29] C. Basting. *Optimization-Based Finite Element Methods for Evolving Interfaces*. PhD thesis, TU Dortmund, 2017.

[30] A. K. Tornberg and B. Engquist. A finite element based level-set method for multiphase flow applications. *Computing and Visualization in Science*, 3:93–101, 2000. doi: 10.1007/s007910050056.

[31] S. Zahedi, M. Kronbichler, and G. Kreiss. Spurious currents in finite element based level set methods for two-phase flow. *International Journal for Numerical Methods in Fluids*, 69(9):1433–1456, 2012. doi: https://doi.org/10.1002/fld.2643. URL https://onlinelibrary.wiley.com/doi/abs/10.1002/fld.2643. DOI: 10.1002/fld.2643.

[32] E. Olsson and G. Kreiss. A conservative level set method for two phase flow. *Journal of Computational Physics*, 210(1):225–246, 2005.

[33] A. Harten. The artificial compression method for computation of shocks and contact discontinuities. I. single conservation laws. *Communications on Pure and Applied Mathematics*, 30(5):611–638, 1977. doi: https://doi.org/10.1002/cpa.3160300506. URL https://onlinelibrary.wiley.com/doi/abs/10.1002/cpa.3160300506.

[34] T. Coupez. Convection of local level set function for moving surfaces and interfaces in forming fow. In *NUMIFORM '07: 9th International Conference on Numerical Methods in Industrial Forming Processes, June 2007, Porto, Portugal. 908*, pages 61–66. Springer, 2007.

[35] V. Boniou, F. Schmitt, and A. Vie. Comparison of interface capturing methods for the simulation of two-phase flow in a unified low-mach framework. *arXiv preprint arXiv:2106.01864*, 2021. URL `https://arxiv.org/abs/2106.01864`.

[36] A. Mitchell and D. Griffiths. *The Finite Difference Method in Partial Differential Equations*. 01 1980.

[37] K. W. Morton and D. F. Mayers. *Numerical Solution of Partial Differential Equations: An Introduction*. Cambridge University Press, 2005. ISBN 9781139443203. URL `https://books.google.de/books?id=0uf_iQIBFKgC`.

[38] F. Stummel. Difference methods for linear initial value problems. In *Numerische Behandlung nichtlinearer Integrodifferential und Differentialgleichungen*, pages 123–135, Berlin, Heidelberg, 1974. Springer Berlin Heidelberg. ISBN 978-3-540-37771-9.

[39] R. Herbin and O. Labergerie. Finite volume schemes for elliptic and elliptic-hyperbolic problems on triangular meshes. *Computer Methods in Applied Mechanics and Engineering*, 147(1):85–103, 1997. ISSN 0045-7825. doi: https://doi.org/10.1016/S0045-7825(97)00010-8. URL `https://www.sciencedirect.com/science/article/pii/S0045782597000108`.

[40] R. J. LeVeque. *Finite Volume Methods for Hyperbolic Problems*. Cambridge Texts in Applied Mathematics. Cambridge University Press, 2002. doi: 10.1017/CBO9780511791253.

[41] C. Cuvelier, A. Segal, and A. A. S. Van. *Finite element methods and Navier-Stokes equations*. Mathematics and its applications. Reidel, 1986. ISBN 90-277-2148-3.

[42] S. R. Singiresu. *The Finite Element Method in Engineering*. Fourth Edition. Butterworth-Heinemann, 2005. ISBN 978-0-7506-7828-5.

[43] G. Strang and G. J. Fix. *An analysis of the Finite Element Method*. Prentice Hall, 1973.

[44] S. C. Brenner and L. R. Scott. *The Mathematical Theory of Finite Element Methods*. Springer, New York, third edition, 2008. ISBN 978-0-387-75933-3.

[45] D. Braess. *Numerical Solution of Partial Differential Equations by the Finite Element Method.* Dover Publications, Dover, 2009.

[46] D. Kuzmin and J. Hämäläinen. *Finite Element Methods for Computational Fluid Dynamics: A Practical Guide.* 01 2015. ISBN 978-1-611973-60-0. doi: 10.1137/1.9781611973617.

[47] H. Elman, D. Silvester, and A. Wathen. *Finite Elements and Fast Iterative Solvers: with Applications in Incompressible Fluid Dynamics.* Oxford University Press, 06 2014. ISBN 9780199678792. doi: 10.1093/acprof:oso/9780199678792.001.0001. URL https://doi.org/10.1093/acprof:oso/9780199678792.001.0001.

[48] V. John. *Finite Element Methods for Incompressible Flow Problems.* Springer series in computational mathematics. Springer International Publishing, [Cham]; Berlin; Heidelberg, 2016. ISBN 9783319457505. doi: 10.1007/978-3-319-45750-5. URL https://archive.wias-berlin.de/receive/wias_mods_00008325.

[49] D. Boffi and L. Gastaldi. On the quadrilateral Q2–P1 element for the Stokes problem. *International Journal for Numerical Methods in Fluids*, 39:1001–1011, 08 2002. doi: 10.1002/fld.358.

[50] D. Boffi, F. Brezzi, and M. Fortin. *Mixed Finite Element Methods and Applications.* Springer Series in Computational Mathematics. Springer Berlin Heidelberg, 2013. ISBN 9783642365195. URL https://books.google.de/books?id=mRhAAAAAQBAJ.

[51] M. Fortin and F. Brezzi. *Mixed and hybrid finite element methods*, volume 3. New York: Springer-Verlag, 1991.

[52] V. Girault and P. A. Raviart. *Finite Element Methods for Navier-Stokes equations.* Springer, Berlin-Heidelberg, 1986.

[53] D. Boffi, F. Brezzi, and M. Fortin. *Finite Elements for the Stokes Problem*, pages 45–100. Springer, Berlin, Heidelberg, 2008. ISBN 978-3-540-78319-0. doi: 10.1007/978-3-540-78319-0_2. URL https://doi.org/10.1007/978-3-540-78319-0_2.

[54] D. N. Arnold, D. Boffi, and R. S. Falk. Approximation by quadrilateral finite elements. *Mathematics of Computation*, 71(239):909–922, 2002. ISSN 0025-5718. doi: 10.1090/S0025-5718-02-01439-4.

[55] J. Hron and S. Turek. *Fluid-Structure Interaction - Modelling, Simulation, Optimization*. Lecture Notes in Computational Science and Engineering. Springer, 2006. ISBN 3-540-34595-7.

[56] M. Fortin. Old and new finite elements for incompressible flows. *International Journal for Numerical Methods in Fluids*, 1:347–364, December 1981. doi: 10.1002/fld.1650010406.

[57] P. Hood and C. Taylor. Navier-Stokes equations using mixed interpolation. *Finite element methods in flow problems*, pages 157–165, 1974.

[58] R. Stenberg. Analysis of mixed finite element methods for the Stokes problem: a unified approach. *Mathematics of Computations*, 42(165):9–23, 1984.

[59] D. N. Arnold, F. Brezzi, and M. Fortin. A stable finite element for the Stokes equations. *Calcolo*, 21(4):337–344, 1984. doi: 10.1007/BF02576171.

[60] M. Benzi, G. Golub, and J. Liesen. Numerical solution of saddle point problems. *Acta Numerica*, 14:1–137, 05 2005. doi: 10.1017/S0962492904000212.

[61] W. C. George. *Fundamental Numerical Methods and Data Analysis*. 1990.

[62] M. Lukacova-Medvid'ova B. J. P. Kaus, R. S. Lehmann and A. A. Popov. Comparison of continuous and discountinous galerkin approaches for variable-viscosity Stokes flow. *Zeitschrift für Angewandte Mathematik und Mechanik*, 08 2015.

[63] S. Brenner and L. R. Scott. *The Mathematical Theory of Finite Element Methods*. Texts in Applied Mathematics. Springer New York, 2002. ISBN 9780387954516. URL `https://books.google.de/books?id=YhPJf_4pu8kC`.

[64] M. Müller. *Lecture Notes: Mathematical and practical aspects of finite elements*. 2010.

[65] R. L. Burden and J. D. Faires. *Numerical Analysis*. Cengage Learning, 2010. ISBN 9780538733519. URL `https://books.google.de/books?id=zXnSxY9G2JgC`.

[66] R. Courant, K. Friedrichs, and H. Lewy. 'Über die partiellen differenzengleichungen der mathematischen physik'. *Mathematische Annalen*, 100(1):32–77, 1928. doi: 10.1007/BF01448839.

[67] J. Crank and P. Nicolson. Practical methods for numerical integration of solutions of partial differential equations of the heat-conduction type.

[68] E. Olsson, G. Kreiss, and S. Zahedi. A conservative level set method for two phase flow II. *Journal of Computational Physics*, 225(1):785–807, 2007. ISSN 0021-9991. doi: https://doi.org/10.1016/j.jcp.2006.12.027. URL https://www.sciencedirect.com/science/article/pii/S0021999107000046.

[69] D. Boffi and L. Gastaldi. On the quadrilateral Q2-P1 element for the Stokes problem. *International Journal for Numerical Methods in Fluids*, 39(11):1001–1011, 2002.

[70] J. Baranger and D. Sandri. A formulation of Stokes's problem and the linear elasticity equations suggested by the Oldroyd model for viscoelastic flow. *M2AN. Mathematical modelling and numerical analysis*, 26(2):331–345, 1992. URL http://www.numdam.org/item/M2AN_1992__26_2_331_0/.

[71] T. Frachon and S. Zahedi. A cut finite element method for two-phase flows with insoluble surfactants. *Journal of Computational Physics*, 473:111734, 2023. ISSN 0021-9991. doi: https://doi.org/10.1016/j.jcp.2022.111734. URL https://www.sciencedirect.com/science/article/pii/S0021999122007975.

[72] S. Hysing. *Numerical Simulation of Immiscible Fluids with FEM Level Set Techniques*. PhD thesis, TU Dortmund, 2007.

[73] C. T. Kelley. *Iterative methods for linear and nonlinear equations*. SIAM, Philadelphia, 1995.

[74] J. E. Dennis and R. B. Schnabel. *Numerical Methods for Unconstrained Optimization and Nonlinear Equations*. Society for Industrial and Applied Mathematics, 1996. doi: 10.1137/1.9781611971200.

[75] W. H. Press, S. A. Teukolsky, W. T. Vetterling, and B. P. Flannery. *Numerical Recipes in C++: The Art of Scientific Computing*. Cambridge University Press, 2002. ISBN 9780521750332.

[76] M. Razzaq. *Numerical techniques for solving fluid-structure interaction problems with applications to bio-engineering*. PhD thesis, TU Dortmund University, Germany, 2011.

[77] H. Damanik. *FEM Simulation of Non-isothermal Viscoelastic Fluids*. TU Dortmund University, Germany, 2011. PhD Thesis.

[78] H. Damanik, J. Hron, A. Ouazzi, and S. Turek. Monolithic Newton-multigrid solution techniques for incompressible nonlinear flow models. *International Journal for Numerical Methods in Fluids*, 71:208–222, 2012.

[79] A. Fatima, S. Turek, A. Ouazzi, and M. A. Afaq. An adaptive discrete Newton method for regularization-free Bingham model. Technical report, Fakultät für Mathematik, TU Dortmund, January 2021. Ergebnisberichte des Instituts für Angewandte Mathematik, Nummer 635.

[80] H. Damanik, J. Hron, A. Ouazzi, and S. Turek. Monolithic Newton-multigrid solution techniques for incompressible nonlinear flow models. *International Journal for Numerical Methods in Fluids*, 71:208–222, 01 2013. doi: 10.1002/fld.3656.

[81] L. N. Trefethen and D. Bau. *Numerical Linear Algebra*. SIAM, 1997. ISBN 0898713617.

[82] G. Strang. *Linear Algebra and Its Applications*. Brooks/Cole, third edition, 1988.

[83] T. A. Davis. Algorithm 832: UMFPACK V4.3-an unsymmetric-pattern multifrontal method. *ACM Transactions on Mathematical Software*, 30(2):196–199, June 2004. ISSN 0098-3500. doi: 10.1145/992200.992206. URL `https://doi.org/10.1145/992200.992206`.

[84] N. Schönknecht. On solvers for saddle point problems arising in finite element discretizations of incompressible flow problems. Master's thesis, Freie Universität zu Berlin, Fachbereich Mathematik und Informatik, Institut für Mathematik, Oct 2015. URL `https://www.wias-berlin.de/people/john/BETREUUNG/master_schoenknecht.pdf`.

[85] P. Wesseling. *An Introduction to Multigrid Methods*. R.T. Edwards, 2004. ISBN 9781930217089. URL `https://books.google.de/books?id=RoRGAAAAYAAJ`.

[86] W. Hackbusch. *Multi-grid methods and applications*, volume 4. Springer Science & Business Media, 2013.

[87] C. W. Oosterlee and P. Wesseling. A multigrid method for an invariant formulation of the incompressible Navier-Stokes equations in general coordinates. *Communications in applied numerical methods*, 8(10):721–734, 1992.

[88] S. P. Vanka. Block-implicit multigrid solution of Navier-Stokes equations in primitive variables. *Journal of Computational Physics*, 65(1):138–158, 1986. ISSN 0021-9991. doi: https://doi.org/10.1016/0021-9991(86)90008-2. URL `https://www.sciencedirect.com/science/article/pii/0021999186900082`.

[89] S. Turek, M. Griebel, D. Keyes, and R. Nieminen. *Efficient Solvers for Incompressible Flow Problems: An Algorithmic and Computational Approache*. Lecture notes in computational science and engineering. Springer-Verlag, 1999. ISBN 9783540654339. URL https://books.google.de/books?id=bHninqVxO_AC.

[90] DFG benchmark 2D-1 (RE20, laminar), . URL http://www.mathematik.tu-dortmund.de/~featflow/en/benchmarks/cfdbenchmarking/flow/dfg_benchmark1_re20.html.

[91] V. John. Higher order finite element methods and multigrid solvers in a benchmark problem for the 3D Navier-Stokes equations. *International Journal for Numerical Methods in Fluids*, 40(6-7):775–798, 2002. doi: 10.1002/fld.377.

[92] S. Turek, A. Ouazzi, and J. Hron. On pressure separation algorithms (PSEPA) for improving the accuracy of incompressible flow simulations. *International Journal for Numerical Methods in Fluids*, 59(4):387–403, 2008.

[93] S. Ganesan, G. Matthies, and L. Tobiska. On spurious velocities in incompressible flow problems with interfaces. *Computer Methods in Applied Mechanics and Engineering*, 196(7):1193–1202, 2007. ISSN 0045-7825. doi: https://doi.org/10.1016/j.cma.2006.08.018. URL https://www.sciencedirect.com/science/article/pii/S004578250600291X.

[94] E. Shirani, N. Ashgriz, and J. Mostaghimi. Interface pressure calculation based on conservation of momentum for front capturing methods. *Journal of Computational Physics*, 203(1):154–175, 2005. ISSN 0021-9991. doi: https://doi.org/10.1016/j.jcp.2004.08.017. URL https://www.sciencedirect.com/science/article/pii/S0021999104003225.

[95] B. S. Hosseini, S. Turek, M. Möller, and C. Palmes. Isogeometric analysis of the Navier-Stokes-Cahn-Hilliard equations with application to incompressible two-phase flows. *Journal of Computational Physics*, 348:171–194, 2017. ISSN 0021-9991. doi: https://doi.org/10.1016/j.jcp.2017.07.029. URL https://www.sciencedirect.com/science/article/pii/S0021999117305375.

[96] F. Denner, F. Evrard, and B. van Wachem. Breaching the capillary time-step constraint using a coupled VOF method with implicit surface tension. *Journal of Computational Physics*, 459:111128, 2022. ISSN 0021-9991. doi: https://doi.org/10.1016/j.jcp.2022.111128. URL https://www.sciencedirect.com/science/article/pii/S0021999122001905.

[97] R. Clift, J. R. Grace, and M. E. Weber. Bubbles, drops, and particles. *Academic Press*, 1978.

[98] M. A. Afaq, S. Turek, A. Ouazzi, and A. Fatima. Monolithic Newton-multigrid solver for multiphase flow problems with surface tension. In *Book of Extended Abstracts of the 6th ECCOMAS Young Investigators Conference 7th-9th July 2021, Valencia, Spain*, pages 190–199, Valencia, Spain, 2021. Editorial Universitat Politècnica de València.

[99] CFD Benchmarking-Rising Bubble, . URL `https://wwwold.mathematik.tu-dortmund.de/~featflow/en/benchmarks/cfdbenchmarking/bubble.html`.

[100] M. Sussman and E. Fatemi. An efficient, interface-preserving level set redistancing algorithm and its application to interfacial incompressible fluid flow. *SIAM Journal on Scientific Computing*, 20:1165–1191, 07 2006. doi: 10.1137/S1064827596298245.

[101] L. Chen, S. V. Garimella, J. A. Reizes, and E. Leonardi. The development of a bubble rising in a viscous fluid. *Journal of Fluid Mechanics*, 387:61–96, 1999.

[102] T. Chen, P. D. Minev, and K. Nandakumar. A projection scheme for incompressible multiphase flow using adaptive Eulerian grid. *International Journal for Numerical Methods in Fluids*, 45:1–19, 05 2004. doi: 10.1002/fld.591.

[103] C. E. Norman and M. J. Miksis. Dynamics of a gas bubble rising in an inclined channel at finite Reynolds number. *Physics of Fluids*, 17(2):022102, 01 2005. ISSN 1070-6631. doi: 10.1063/1.1842220. URL `https://doi.org/10.1063/1.1842220`.

[104] M. Sussman and E. Puckett. A coupled level set and volume-of-fluid method for computing 3D and axisymmetric incompressible two-phase flows. *Journal of Computational Physics*, 162:301–337, 08 2000. doi: 10.1006/jcph.2000.6537.

[105] W. Hakon. Sphericity and roundness of rock particles. *The Journal of Geology*, 41:310–331, 05 1993.

[106] S. Aland and A. Voigt. Benchmark computations of diffuse interface models for two-dimensional bubble dynamics. *International Journal for Numerical Methods in Fluids*, 69:747–761, 05 2012. doi: 10.1002/fld.2611.

[107] W. Liu, W. Hu, S. Chen, J. Wu, and Y. Chen. Deep learning of interfacial curvature: a symmetry-preserving approach for the volume of fluid method. *Journal of Computational Physics*, 485:112110, 2023.

[108] L. Gamet, M. Scala, J. Roenby, H. Scheufler, and J. Pierson. Validation of volume-of-fluid OpenFOAM® isoadvector solvers using single bubble benchmarks. *Computers and Fluids*, 213:104722, 2020. ISSN 0045-7930. doi: https://doi.org/10.1016/j.compfluid.2020.104722. URL https://www.sciencedirect.com/science/article/pii/S0045793020302929.

[109] M. Sussman, P. Smereka, and S. Osher. A level set approach for computing solutions to incompressible two-phase flow. *Journal of Computational Physics*, 114(1):146–159, 1994. ISSN 0021-9991. doi: https://doi.org/10.1006/jcph.1994.1155. URL https://www.sciencedirect.com/science/article/pii/S0021999184711557.

[110] J. E. Welch, F. H. Harlow, J. P. Shannon, and B. J. Daly. The MAC method-a computing technique for solving viscous, incompressible, transient fluid-flow problems involving free surfaces. Technical report, Los Alamos National Lab., Los Alamos, N. Mex. (United States), 11 1965. URL https://www.osti.gov/biblio/4563173.